UNIVERSITÀ DEGLI STUDI DI MILANO

Scuola di Dottorato in Fisica, Astrofisica e Fisica Applicata

Dipartimento di Fisica

Corso di Dottorato in Fisica, Astrofisica e Fisica Applicata

Ciclo XXVIII

Development and Characterization of an Innovative Low-Noise High-Dynamic-Range VLSI Charge-Sensitive Preamplifier for Solid-State Detectors Employed in Nuclear Physics Experiments with Radioactive Ion Beams

Settore Scientifico Disciplinare FIS/01

Supervisore: Professor Alberto PULLIA

Coordinatore: Dottor Daniele MENGONI

Tesi di Dottorato di:

Stefano CAPRA

Anno Accademico 2014-2015

Commission of the final examination:

External Referee:

Professor Bertuccio Giuseppe

Politecnico di Milano - giuseppe.bertuccio@polimi.it

Other Members:

Professor Mikolajick Thomas

Technische Universität Dresden (DEU) - thomas.mikolajick@namlab.com

Professor Pullia Alberto

Università degli Studi di Milano and INFN, Milano - alberto.pullia@unimi.it

Professor Spiga Sabina

Istituto per la Microelettronica e Microsistemi, CNR - sabina.spiga@mdm.imm.cnr.it

Final examination:

Date 25-01-2016

Università degli Studi di Milano, Dipartimento di Fisica, Milano, Italy

Cover illustration:

Stefano Capra

Internal illustrations:

Stefano Capra

Design:

Stefano Capra and Annalisa Varri

MIUR subjects:

FIS/01 - Fisica Sperimentale

PACS:

85.40.-e

Contents

Introduction

TRACE is an array of Silicon pad detectors in a telescopic configuration for nuclear physics experiments with radioactive ion beams. Any single detector prototype consists of 60 square pads, arranged in 5 rows and 12 columns. The size of the pad is 4x4 mm^2. The telescopic configuration allows to discriminate the impinging particles using an E/ΔE method. However this method is not suitable for low-energy particles because they are stopped by the first thin layer of the telescope. In order to extend the discrimination capabilities of TRACE in the low energy range down to the limit of few MeV, pulse-shape analysis is performed. This technique is based on the analysis of the current profile of the detector pulses. Different particles yield slower or faster signals. The typical width of the current pulses is in the order of 10 ns for the thin ΔE layer. The Charge-Sensitive Preamplifier (CSP) must provide signals fast enough to preserve that information. In the foreseen experimental setup a large count of electronic readout channels is to be packed inside the relatively small volume of the scattering chamber and the front-end electronics must work in vacuum. Both the form-factor and the power dissipation constraints force the designer to opt for integrated solutions. We designed and realized an integrated multichannel charge-sensitive preamplifier suited for this application. Its main features are low power consumption, low noise, fast rise time and programmability. A few critical circuit parameters are adjusted through an I^2C bus, choosing from a set of preset values. In particular the preamplifier can be optimized to work properly with different detector capacitances, ensuring best rise time with little or no ringing in a wide range of different experimental conditions. A compact 5 mm^2 CSP ASIC has been designed and realized, which comprises four channels for the front pads and one channel for the back connection of the detector.

Chapter 1

Brief introduction to nuclear physics experimental set-ups

In this chapter we present briefly the methods for the study of nuclear properties with heavy-ion beams at energies up to 10 MeV ·A together with associated detection systems. Starting from recent results in the study of nuclear structure we will describe motivations and methods for the future research. This will be made possible thanks to the new accelerating facilities implementing Radioactive Ion Beams (RIBs) together with new instrumentation including large gamma-ray spectrometers, recoil mass spectrometers and other ancillary detectors.

1.1 Studies and considerations on the nuclear landscape

Theoretical calculations state that there are more than three thousands of nuclei in the nuclear landscape that are bounded by the strong force, but only 300 of them are stable (see figure 1.1). The others are bound against the emission of protons and neutrons but not against β-decay. In this case there is a transformation of a proton in a neutron or vice versa with the emission of an electron or a positron. The characteristic decay time of some unstable nuclear species can be so long that we can find naturally them on Earth. Many others can be produced and analysed in laboratory but a great part of all the possibly bound nuclear systems is still undocumented. In the last years the study of the nuclide chart far from the valley of stability is a topic of great interest. The final goal is the comprehension of the nuclear force that bonds not only the naturally abundant stable nuclei but also the multitude of weakly bound systems that can be produced by stellar explosions and may exist in the universe. The study of the nuclei in critical configurations is a great challenge both from a scientific and a technological point of view

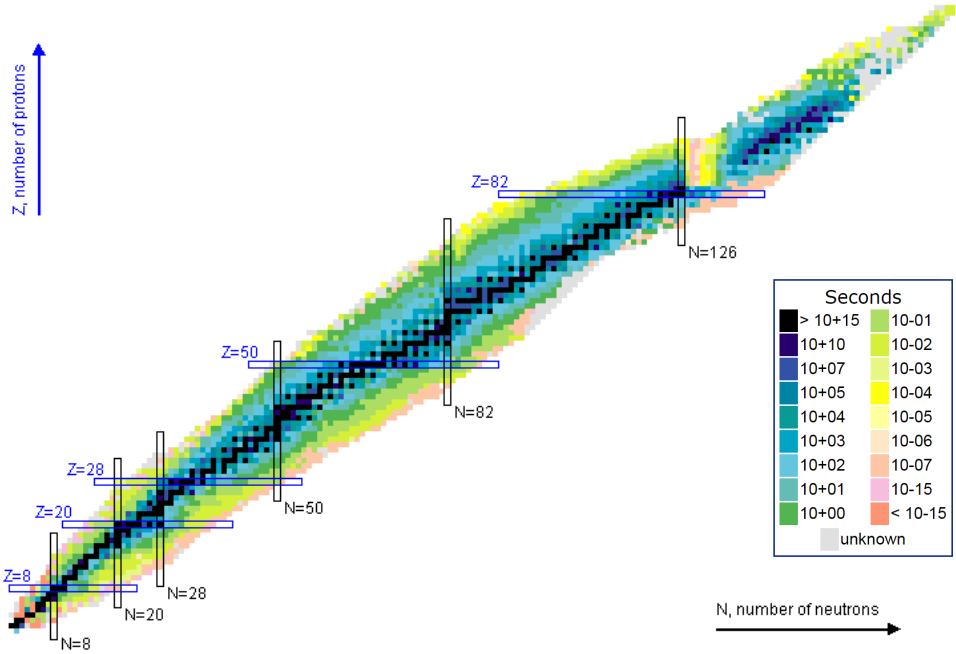

Figure 1.1: Table of nuclides. The color scale refers to the half-life as described in legend. The nuclides pictured in black are considered stable. The neutron-rich part of the diagram is in the lower-right corner while the proton-rich, much more investigated, is in the upper-left one. The magic numbers for proton and neutron are highlighted in the chart [1].

but the knowledge that derives from it will help us to understand properly the structure of the nucleus intended as a many-body system bonded by the nuclear interaction.

It is generally easier to produce proton-rich nuclei than neutron-rich ones. In fact you can obtain nuclei near the proton drip-line with fusion-evaporation reactions, where several neutrons are emitted. If the proton-rich side of the nuclear chart was deeply investigated, big areas in the neutron-rich side are still to be explored. In fact the neutron drip-line was reached only for light nuclei up to Fluorine. The great questions about the nuclear structure are essentially the following. The first one is how many neutrons and protons can be bonded by the strong interaction. This question refers mainly to the neutron-rich side of the table because of the large number of nuclides in the area between the theoretic neutron drip-line and the limit of experimentally observed configurations. Another great question is about the boundary in the heaviest existing nuclei. These ones can exist only if the attracting strong force overtakes the repulsive Coulomb force. Theoretical predictions about the physical limit in weight are uncertain and must be

experimentally validated. Among the others, short-lived neutron-rich nuclear systems are particularly interesting. Only a small part of nuclei far from stability have been produced and studied in laboratory, giving us important information and opening the door to new perspectives.

Our knowledge about nuclear structure is based on some long-standing ideas that may be valid only near the valley of stability. For example, we know that nuclei with some particular number of protons and neutrons (called "Magic Numbers") show a high degree of stability. These rules, although valid within the known region may not be accurate or valid at all near the drip-lines. Magic numbers were historically used as key landmarks in the table of nuclei but we don't know if these rules are valid all across the nuclear landscape. Those numbers may change or even not be valid at all for some extreme nuclear systems. The actual knowledge about nuclei farthest from stability is circumscribed to a little number of cases. In the next years the study of exotic radioactive nuclei will give an answer to both physics and astrophysics open questions. Stable beams are limited to $\approx$100 species. RIB facilities will provide more than 1000 exotic beams with very different intensities. It will be possible to choose the desired exotic nucleus in order to exalt a specific effect.

RIBs can provide new nuclear configurations with unusual orbits and quantum numbers, opening endless possibilities to the discovery of new nuclear structure phenomena. In a stable nucleus the nucleons are bound with a typical energy of 5-8 MeV. For nuclei near the drip-line, the external nucleons, whose binding energy is about hundreds of keV, are described by wave functions that decay exponentially with $[2m(E-V)]^{\frac{1}{2}}$ within the potential barrier. That functions extends to large radii because $(E-V)$ is small. The consequence is that the shell model potential, the spin-orbit force and the residual interaction among nucleons can be altered, leading to new structures and evolutions. The physics of common stars can be described with the fusion of hydrogen into helium, of helium into carbon, with the sequences (p,γ), (p,α) and with the β-decay. These reactions constitute the CNO cycle (Carbon, Nitrogen, Oxygen) pictured in figure 1.2. A critical parameter in the understanding of such phenomena is the reaction rate of each step. This involves unstable nuclei which are still poorly understood. The CNO cycle still requires an adequate quantitative description and there are still open questions about the generation of heavier nuclei with rapid-neutron-capture (r-process) and rapid-proton-capture (rp-process) processes.

Simulations of extreme stellar processes such as supernovae explosions or X-ray

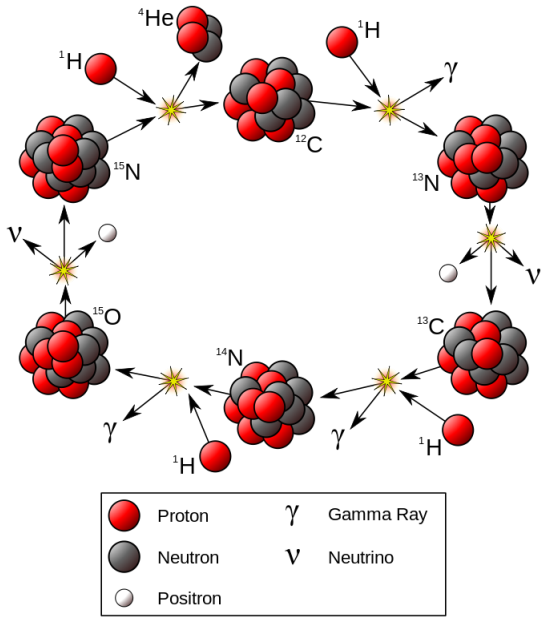

Figure 1.2: Pictorial view of the Carbon-Nitrogen-Oxygen cycle, the main reaction involved in the heat production in stars.

bursts require accurate models of unstable nuclei because their role in such reactions is fundamental. Depending on the abundance of protons or neutrons inside the stellar environments, r-process or rp-process can occur. The firsts are thought to produce heavier elements by means of sequential neutron captures and β-decays. In order to have accurate prevision models of such phenomena we need to know the exact mass of nuclei far from the valley of stability, together with their β-decay half-lives and their neutron or proton capture cross-section. Reliable simulations of physical events in the primordial era of the universe require thus experimental measurements of the properties of exotic nuclei, especially in the neutron-rich side of the table, where the information is fewer.

1.2 The forthcoming Radioactive facilities

The great interest in the perspectives opened by the implementation of radioactive ion beams in nuclear research led to the design and construction of new acceleration facilities all over the world. Some of them are already working, some are under construction and new ones are planned for the future. There are two main methods to produce RIBs: the

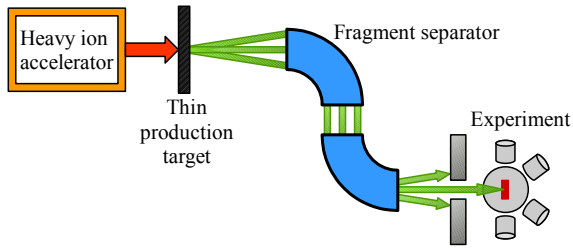

Figure 1.3: Pictorial view of a projectile-fragmentation (PF) facility for the production of radioactive ion beams. The first accelerator produces a beam of heavy ions that collides against a thin target generating a beam of radioactive ions with different mass charge and momentum. From this heterogeneous beam the desired ions are isolated by means of a separator and then sent to the reaction chamber.

Projectile Fragmentation (PF) method and the Isotope separation on-line method (ISOL). The PF method, schematically represented in figure 1.3 provides that a first heavy ion beam is made to collide with a thin production target. The nuclear reaction produces a variety of reaction fragments different in mass, charge and momentum. In-flight fission of very heavy beams, exchange and transfer reaction are alternatives to the projectile fragmentation method. The desired ion beam is extracted from the reaction products by means of a fragment separator. The energy of the final beam is provided by the accelerator of the first heavy-ion one. The radioactive ions are produced in-flight and thus require no post-acceleration. This technique was implemented for the first time in the Lawrence Berkeley National Laboratory at the beginning of the eighties. The fragment separator introduces a delay time between the production of radioactive nuclei and the reaction against the final target of some hundreds of ns. In this way also very unstable nuclei with short half-lives can be analysed.

The ISOL technique, schematically represented in figure 1.4, is based on a quite different concept. A primary beam of particles (thermal neutrons, GeV protons, deuterons with medium energy and even heavy ions) are made impinge against a thick hot target. The reaction products, almost at rest, diffuse through a transfer tube and reach the ion source. Here they are ionized and loosely accelerated. The heterogeneous low-energy beam is then differentiated in charge and mass by means of electro-magnetic selectors. The desired species extracted are accelerated again in a secondary accelerator called "postaccelerator" until they reach the energy needed by the experiment. Because of this

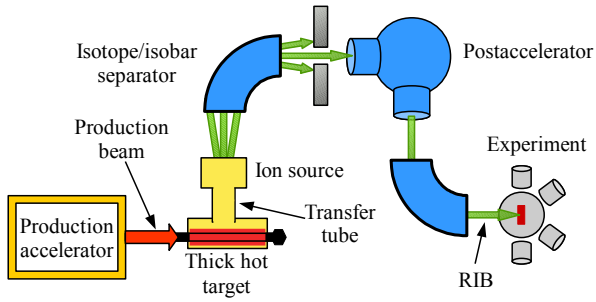

Figure 1.4: Pictorial view of a Isotope-separation on-line (ISOL) facility for the production of radioactive ion beams. The first accelerator produces a beam of protons, neutrons, deuterons or heavy ions that collides against a hot, thick target. Radioactive species are generated almost at rest, collected in the transfer tube and ionized. The beam produced is then separated and accelerated by the postaccelerator and sent to the reaction chamber.

two-step procedure, ISOL method is often called also "two-accelerator method". The post-accelerators can be of very different kinds: linacs, cyclotrons or tandem. ISOL and PF are somehow complementary. In fact RIBs from PF facilities are directly produced at high energies (50-100 MeV·A) while beams obtained with the ISOL method are accelerated from zero energy up to 10-20 MeV·A (energy range from below to above the Coulomb barrier). ISOL facilities have a minor drawback. The delay time needed to collect the first reaction products, ionize, separate and post-accelerate them is higher that the delay times of the PF method. This problem is however a minor clue because the main decay channel on many radioactive nuclei of interest is the β-decay and their half-lives are longer than milliseconds.

Above all, the simple existence of the radioactive beam is not sufficient at all to obtain good experimental results. Other parameters are of paramount importance in that sense. The collimation of the beam on the target, together with proper channel selection have a great impact on efficiency and both angular and energy resolution. The reduction of the background is mandatory, especially if very sensitive apparati are used. Below a short list of new RIB facilities is reported. Some of them are already operative and others are under construction. Those of the ISOL type are: SPIRAL and SPIRAL2 at GANIL (Caen, France), REX ISOLDE at CERN (Genève, Switzerland), SPES at LNL (Legnaro, Italy), HRIBF (OakRidge, USA), ISAC-I and II at TRIUMF (Vancouver, Canada), etc. The PF facilities are: GANIL(Caen, France), GSI (Darmstadt, Germany), NSCL at MSU (Michigan, USA), Flerov Laboratory (Dubna, Russia), RIKEN (Saitama, Japan), IMP

Characteristics	STABLE	ISOL	PF
Energy available(MeV·A)	10÷100	10÷20	50÷100
Intensity (p/s)	1010÷13	104÷8	<105
Energy dispersion		small	big
Contaminant	monoisotopic	monoisotopic	isobaric
Beam spot (mm)	~1	>1	>10
Timing	~100 ns	>1 ms	~100 ns

Table 1.1: This table shows some key parameters of the beams produced with different methods. The results obtained with the ISOL technique depend heavily on the element chosen due to the complexity of the extraction process preceding the second acceleration.

(Lanzhou, China), etc. The development of more ambitious and challenging projects such as EURISOL [2] may be possible only thanks to the knowledge and expertise gained in the realization of large facilities such as SPES ans SPIRAL. In table 1.1 some characteristics of different beam types are reported.

1.3 Reactions, cross-sections and beam requirements

In nuclear research with radioactive ion beams some well-understood reactions are used. For our purposes the most common ones are:

- **Elastic and inelastic scattering.** These reactions are used to evaluate form factors, transition amplitudes and shape parameters of exotic nuclei.

- **Coulomb excitation.** This is used to study vibrational and rotational modes and the coupling of single-particle and collective degrees of freedom, especially for nuclei near the drip lines.

- **Radiative capture and Coulomb dissociation.** These reactions enable to determine cross sections, resonance energies and strengths for astrophysical reactions.

- **Transfer reactions.** These can involve a single nucleons or few nucleons. These can be used to determine single particle energies, effective nucleon-nucleon interactions, strengths distributions, and particle correlations in doubly magic closed shell nuclei far from stability and in weakly bound nuclei close to the drip lines.

- **Fusion-evaporation reactions.** The analysis of the gamma spectra coming from these reactions enable the study of the band structure of the nucleus.

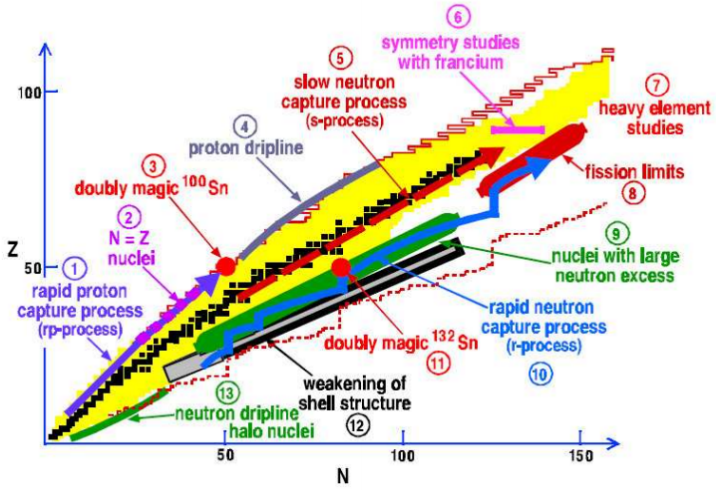

Figure 1.5: Research opportunities with beams of short-lived nuclei. Regions of interest that can be explored with a second-generation ISOL facility are shown. This is a schematic representation, characterising the areas of research and exemplifying types of studies. The desired beam intensities, where not available from present first-generation ISOL facilities, can be achievable with new technological developments as expected at an advanced ISOL facility.

- **Fusion-fission reactions.** Common reactions of great interest since the beginning of the nuclear research.
- **Strongly damped collisions.** These are used to extend the range of neutron-rich nuclei. These studies will also encompass the broad range of tools and methods developed for nuclear decay studies including the most modern methods to prepare nuclei for specific studies - ion and atom traps.

In figure 1.5 different areas of interest on the table of nuclei are shown. If these cannot be reached with present ISOL facilities, they will be available with the ones under development. Some case-studies are used to represent a whole class of possible investigations, suggesting both beam requirements and experimental approaches. Each type of science area, with its own cross-section, requires a specific beam intensity. The upper part of figure 1.6 shows the beam intensities required by different research areas due to the corresponding cross-section. The bottom graph shows the methods usually adopted for the nuclear research with stable beams. Thanks to the know-how gained in past studies these techniques can be now used in the research with radioactive ion beams. In the last decades a continuous development of large gamma-ray spectrometers took place. These

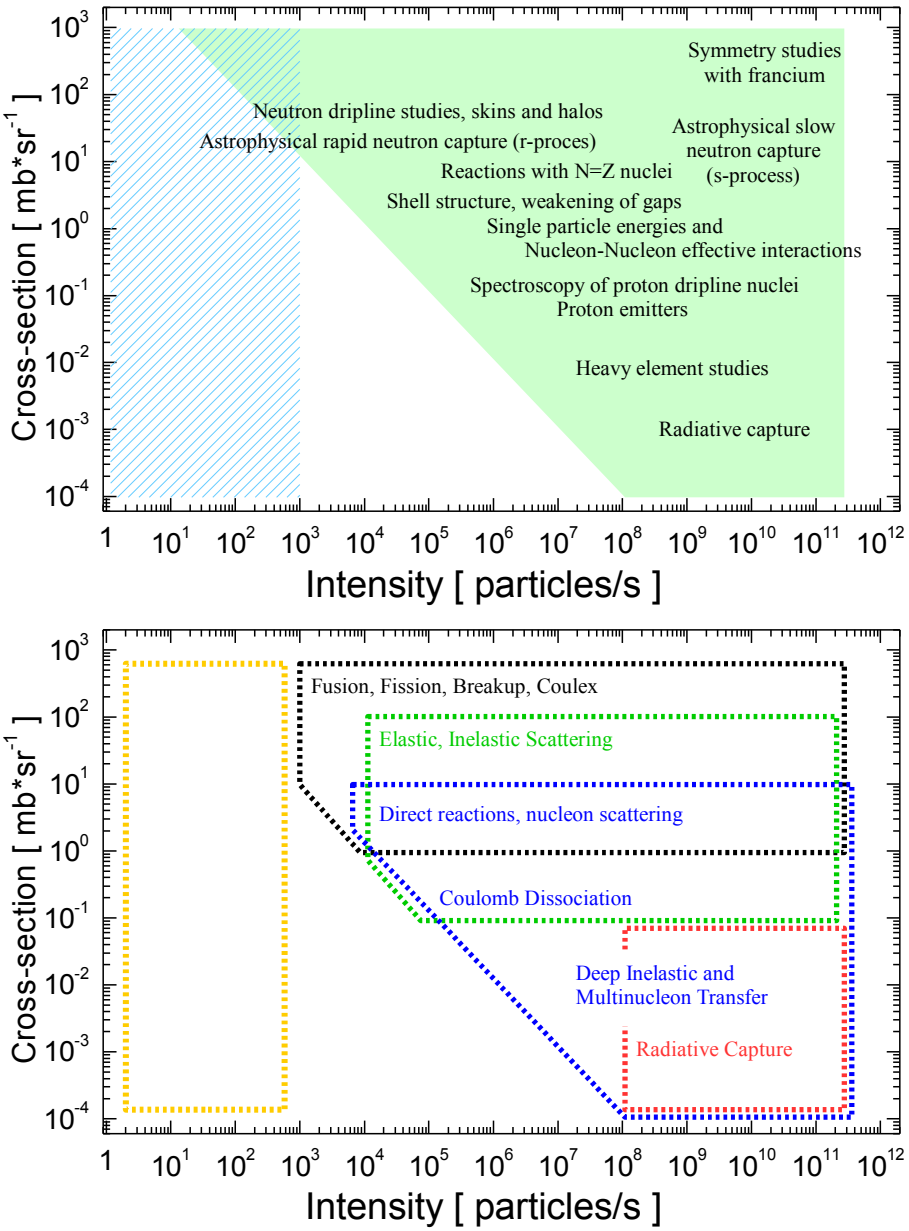

Figure 1.6: Cross section $[\text{mb} \cdot \text{sr}^{-1}]$ versus required beam intensity for the areas of research illustrated in figure 1.5. The top panel shows the relation of these areas with typical cross sections and needed beam intensities. The bottom panel indicates the cross section and the beam intensity, which are necessary to use the well-established reaction processes and methods that have been developed to a high level of sophistication in the past decades with stable beams. Now they can be effectively applied to the new physics opportunities with unstable beams [3].

devices have been improved both in energy resolution, efficiency and angular coverage. These can be coupled to complementary equipment capable of mass and atomic number selection and light- and heavy-ion identification. The sensitivity enhancement resulting from these technological improvements will open new possibilities in the study of weakly-populated nuclear configurations.

There are some reactions of paramount importance in the study of nuclei far from the stability valley. Direct reactions with RIBs are performed in inverse kinematics and require the detection of light charged particles and neutrons in a wide dynamic range, together with a spectroscopic analysis of the scattered projectiles. Transfer, knock-out and break-up reactions give information about the microscopic shell structure of the nuclei. Information about nuclear densities and transition intensities are provided by elastic and inelastic scattering. If heavy ions have enough energy to break through the Coulomb barrier they melt with the nucleus forming a compound nuclear structure, which de-excites with the emission of gamma rays and evaporating particles. These reactions are thus called fusion-evaporation and are used to populate high-spin nuclear states in proton-rich nuclei. The TRACE detector array is mainly focused on transfer and fusion-evaporations ones. Both the silicon detectors and the front-end electronics have to be conceived to maximize the performance in these experimental contexts.

1.4 Details on different nuclear reactions

In this section we will provide some detailed information on different kind of reactions with focus on the information they can provide and citing some case-studies as examples.

Transfer reactions

Transfer reaction are divided into three groups, depending on the number of nucleons involved: there are single-nucleon reactions, two-nucleon reaction or multi-nucleon reactions. In single-nucleon transfer reaction the product is a structure that is given by the original nucleus as a core, with the transferred nucleon in an orbit around it. This is an excellent way to probe the energies of the shell model orbitals and the corresponding changes in energy moving away from the valley of stability. These reactions, despite a lot of details and non-idealities, tend to populate mainly single-particle states in the final nucleus which, in turn, are really interesting from a theoretical point of view. For this reason, single-particle transfer reactions are among the most important sources of information about the nuclear structure, thanks to the new upcoming RIB facilities. Quantum

single-particle levels away from the line of stability will be mapped for exotic nuclei using heavy ion beams and hydrogen isotopes as target, as in early transfer experiments with stable beams. The reactions will thus be realized in inverse kinematics. The reactions that use a proton or deuteron as projectiles and that produce respectively a deuteron or a tritium, namely (p, d) or (d, t) are called pick-up reactions. The products of these reactions (deuteron or tritium) are focused in the forward hemisphere of the reaction chamber. In stripping reactions such as (d, p) the light ejectiles are emitted mainly in the backward hemisphere of the reaction chamber. Elastic scattering is concentrated at 90 degrees angle. This means that we can identify light ejectiles just analysing their energy and their angle respect to the center of mass. The Z-identification can be useful in some particular conditions. Thanks to the greatly improved sensitive of large gamma spectrometers, the measurement of coincident gamma rays can enhance the resolution of individual quantum states by means of ejectile identification.

Some physics-cases are the study of the $N = 20$ closed shell with beams of neutron-rich fluorine producing neutron-rich oxygen nuclides via the stripping of a proton. Other possible solutions are given by $^{24}O(d, p)^{25}O$ and $^{24}O(\alpha,^3 He)^{25}O$. For these reactions beam intensities of at least 10^4 pps are required with energies in the order of 5-20 MeV·A. Also the study of neutron-rich Ni isotopes are of great interest, together with the analysis of the single-particle orbits near the Fermi surface for $N = Z = 40$.

In stable nuclei a lot of physical parameters are influenced by the presence of pairing between identical nucleons. Some of these parameters include rotational moments of inertia, collective vibrational modes, gamma-transition probabilities and low-lying level structures. For nuclei far from the valley of stability the particle separation energy becomes smaller approaching to the drip-line. In these conditions the pairing energy covers a fundamental role because is responsible for the existence of a bound state. Beside pairing between identical nucleons, also proton-neutron pairing is an interesting phenomenon. It should be relevant mostly in those nuclear configurations where the $N = Z$ line departs from the stability valley. In fact only in $N = Z$ nuclei both protons and neutrons share the same orbitals and thus p-n pairs with spatial correlation is possible. An interesting method to study the pairing between identical nucleons is the evaluation of the probability of (t, p) or (p, t) reactions. In these reactions, generally performed in inverse kinematics, a pair of neutrons are transferred from the projectile to the target or vice versa.

In multi-nucleon transfer reactions a series of single-nucleon and two-nucleon trans-

fers take place, together with the transfer of whole clusters. Even if there is still a lot of aspects that require a deeper comprehension, the study of multi-nucleon transfers will give important information about the dependence of the pairing correlation as a function of neutron number. It is supposed that the two-neutron separation energy is dropping in case of neutron excess. This fact should enhance the pair-transfer mode and consequently the multi-pair transfer mode. The study of multi-nucleon transfer reaction will help to give answer to such theoretical questions. Moreover these reactions are a valuable tool to produce neutron-rich nuclei in those specific mass regions, like actinides and transactinides, where other methods are not effective. Experiments with radioactive ion beams involving the transfer of more than two nucleons have not been performed yet. Neutron-rich RIBs may be used to populate nuclei near the drip-lines even if the cross-section of transfer reactions drops by a factor of 3 to 4 for each transferred neutron.

Break-up reactions

Break-up reactions take place at higher energies respect to transfer reactions (tens of MeV vs units of MeV) but represent a valid alternative to the second ones. There is no exchange of light particles or single nucleons. The reaction lead to the fragmentation of the original nucleus. This technique was used to study halo nuclei. These ones are constituted by a group of core nucleons surrounded by a halo of orbiting protons and neutrons at relatively large radii. In these cases, when break-up reactions take place the core nucleons are separated from the halo ones which collapse in a separated nucleus. The idea is to exploit these reactions to analyze nuclear structures less dependent on the asymptotic part of the wave function. In the beginning break-up reactions were used to measure just the nuclear radii looking at the overall cross-section, but can be used to study excited states in exotic nuclei looking for core-gamma coincidences. Neutron-core coincidence measurements can provide additional information, together with correlation between emitted particles which may disentangle Coulomb excitation from nuclear break-up.

Coulomb excitation

Coulomb excitations are reactions mediated by the electromagnetic field. Two nuclei are made to collide inelastically, enabling the study of collective excitations, which are often connected by electric quadrupole transitions. Together with (p, p') inelastic scattering these reactions are complementary to transfer ones and can probe changes in proton and neutron densities. There reactions can be used in the study of the Calcium and Nickel

isotopic chains, in the search for new doubly-magic nuclei and for the investigation of the shell structure of heavier nuclides and the evolution of magic numbers far from the valley of stability.

Fusion-evaporation reactions

In fusion-evaporation reactions the beam is accelerated at energies above the Coulomb barrier. The collision with the target induces the fusion of the two nuclei. The compound nucleus thus obtained evaporates nucleons and finally decays by means of gamma emission. With this technique is easy to produce proton-rich nuclei. In fact lighter nuclei have a lower N/Z ratio respect to heavier stable nuclei. For this reason, after the fusion the compound nuclei are naturally neutron-deficient. Moreover compound nuclei tend spontaneously to emit neutrons, populating nuclear structures near the proton drip-line. With this technique also neutron-rich nuclei can be produced, but radioactive beams (or targets) are required. The acceleration of proton-rich radioactive ions to Coulomb-barrier energies to induce fusion-evaporation reactions shows to be an excellent method to explore the proton drip-line in the heavier mass region (above Z = 50). Another open question is the maximum angular momentum sustainable by a nucleus. It is well known that neutron abundance can enhance stability against fission due to high-spin states. For this reason the research is focused both in the study of high-spin states near the stability region and maximum-spin states in the neutron-rich area. In the former case fusion-evaporation reaction induced by neutron-rich beams can be used, while in the latter relatively high-spin states can be produced in fragmentation reactions.

1.5 Techniques and equipments for experiments with radioactive ion beams

Experiments with radioactive ion beams imply the study of a lot of different physical observables and each one requires a dedicated set-up. The exploration of the ground-state properties of exotic nuclei include the measurement of masses, electromagnetic moments, radii of matter and charge and, moreover, a series of phenomenological quantities related to fundamental symmetries and interactions. Nuclear structure studies require β-delayed neutron spectroscopy, decay spectroscopy and in-beam gamma-ray and conversion electron spectroscopy. Delayed neutrons are those emitted by the nuclei produced by nuclear reactions. Decay spectroscopy is a term which refers to a series of

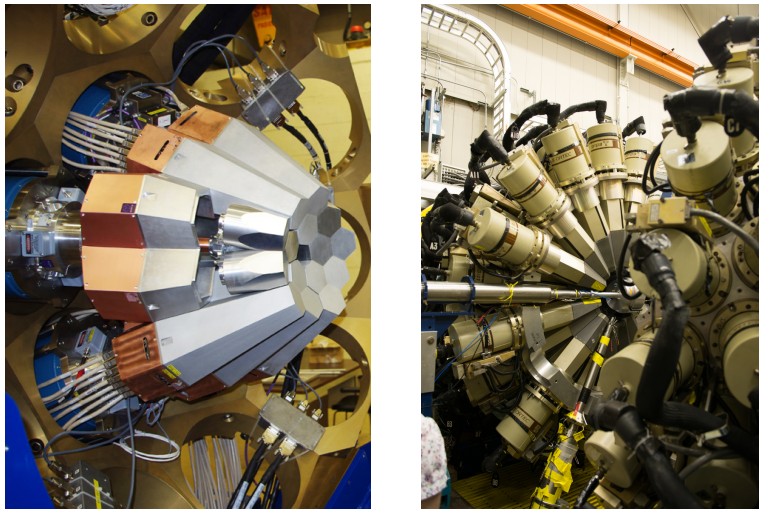

Figure 1.7: On the left a photo of the AGATA array, the most advanced gamma-ray tracking array, still under development. On the right the GAMMASPHERE array, which consists of 108 Compton-suppressed large volume, high-purity germanium detectors in a spherical configuration.

techniques and methods aimed at determining the decay properties of radioactive nuclei from the analysis of the particles emitted. Decay experiments are at the forefront of exploration at the limits of nuclear stability. In fact, once the existence of an isotope has been verified, the next critical piece of information required is its decay mechanism.

Modern gamma spectrometers have ray tracking capabilities. These require efficient and high-fold segmented germanium detectors together with dedicated digital signal processing, Pulse-Shape Analysis (PSA) and tracking algorithms. It is thus possible to reconstruct the multiple interactions of a single gamma photon inside the spectrometer. This requires a precision in the order of 1 mm in the measurement of the interaction position. It would be impossible to reduce the detector segmentation down to similar pitches, because of physical production limits and costs. Also the number of acquisition channels would increase exponentially. On the other hand, the current profile produced by the detectors contain information about the position of interaction of the gamma ray inside the crystal. PSA thus enables the experimenter to achieve a very good spatial resolution even using a wider pitch detector segmentation.

Experiments with radioactive ion beams require different information to be collected simultaneously. For this reason arrays of multidetectors are mandatory which can detect gamma rays, light particles ejectiles, heavy fragment, neutrons and other fission

fragments. Not only the beams but also the targets must comply with stringent requirements. Ion and charged particle spectroscopy is performed with gas-filled separators, recoil mass spectrometers, ray-tracking spectrometers and fragment recoil separators. The techniques listed above make possible the measurement of a lot of interesting observables in the research with radioactive nuclear beams: atomic masses and radii, shapes and moments. They enable the study of decay properties of exotic nuclei, drip-line phenomena, nuclear structure and excitation modes, reaction processes involving radioactive projectiles and heavy and super-heavy nuclei.

1.6 Large gamma-ray spectrometers

EUROBALL [4] and GAMMASPHERE [5] are among the state-of-the-art gamma-ray spectrometers available. They are made of hundreds of hyper-pure germanium detectors with BGO Compton suppression. They have a 4π geometry, with an inner diameter of 30 cm. Their photo-peak efficiency is around 10% with a peak-to-total ratio of $\approx$ 60%. The readout system is based on standard analogue electronics. Since the intrinsic energy resolution is smaller than 2.3 keV, the energy resolution is dominated by Doppler broadening for reactions with recoil velocity higher than the 3% of the speed of light.

Gamma spectrometers that will be used in radioactive ion beam experiments will have more stringent requirements regarding both photo-peak efficiency, peak-to-total ratio and angular resolution. The ideal 4π set-up would be made of detectors with large sensitive volumes and high segmentation. Using an array of single-crystal detectors, the photo-peak efficiency is limited by their physical volume which, in turn, is practically limited by cost. In Compton-suppressed detectors with 80% of relative efficiency the maximum photo-peak efficiency obtained is $\approx$ 10%. The only way to increase photo-peak efficiency at constant volume is to move the detectors closer to the target, but this would deteriorate the energy resolution due to the Doppler effect. A smart solution is the packing of more than one detector inside the same cryostat. Compton scattering events that involve more than one detector in the cryostat are added together, leading to a better photo-peak efficiency. This technical solution shows also some benefits regarding resolving power. In fact a better definition of the incoming photon direction enables a better correction of Doppler effects. A 4π array can have a photo-peak efficiency higher than 20%. In the EUROBALL array a photo-peak efficiency of 3.8% could be obtained thanks to the adoption of clover detectors, which are groups of four germanium crystals inside a single cryostat. The overall active volume in this configuration is cubic-like. In

		Ge-shell	AGATA
Efficiency	E_γ=0.1 MeV, M_γ=1, 0<β<0.5	100%	>70%
	E_γ=1 MeV, M_γ=1, 0<β<0.5	72%	≃50%
	E_γ=10 MeV, M_γ=1, 0<β<0.5	15%	≃10%
	E_γ=1 MeV, M_γ=30, 0<β<0.5	36%	≃25%
Peak-to-total ratio	E_γ=1 MeV, M_γ=1	85%	60÷70%
	E_γ=1 MeV, M_γ=30	60%	40÷50%
Angular resolution	ΔE/E <1%	-	better than 1
Maximum rates	M_γ=1	-	3 MHz
	M_γ=30	-	0.3 MHz
Inner free space		150 mm	170 mm

Table 1.2: Comparison of AGATA parameters with the ones of an ideal germanium shell with 150mm inner radius and 90mm thickness.

the backware hemisphere of same experiment also cluster detectors were used. They are made of seven hexagonal close-packed germanium crystals. 15 of them produced an overall photo-peak efficiency of $\approx 4.4\%$.

Traditionally the Compton suppression is made with BGO or NaI scintillators, which are wide and cheap. They surround the germanium crystals and work in anti-coincidence mode, in order to reject events in which the gamma ray is scattered out of the detector before depositing all its energy. Compton shields have a bigger stopping power respect to germanium detectors and it is very unlikely that the gamma ray escapes from both. This improves the quality of the spectra, especially in the low energy range. Innovative gamma spectrometers like AGATA (figure 1.7) and GRETA remove the Compton shields and pack all the Germanium detectors one close to the other. The tracking of the gamma rays inside the spectrometer allows an excellent reconstruction both of the original energy and direction. Pulse shape analysis on the output signals enable the 3D reconstruction of the interaction points inside the detectors with $\approx$ 11mm resolution. AGATA is an Advanced GAmma-ray Tracking Array [10]. Proposed in 2001 and subscribed by twelve European countries in 2002, it is expected to be complete within 2018. It is made of HPGe detectors without Compton suppression and was designed to manage high counting rates while providing high energy and angular resolution and high Peak/Total (P/T) ratio. AGATA detectors are 36-fold segment with six-fold azimuthal and six-fold longitudinal segmentation. The performance comparison with other gamma spectrometers is reported in figure 1.8.

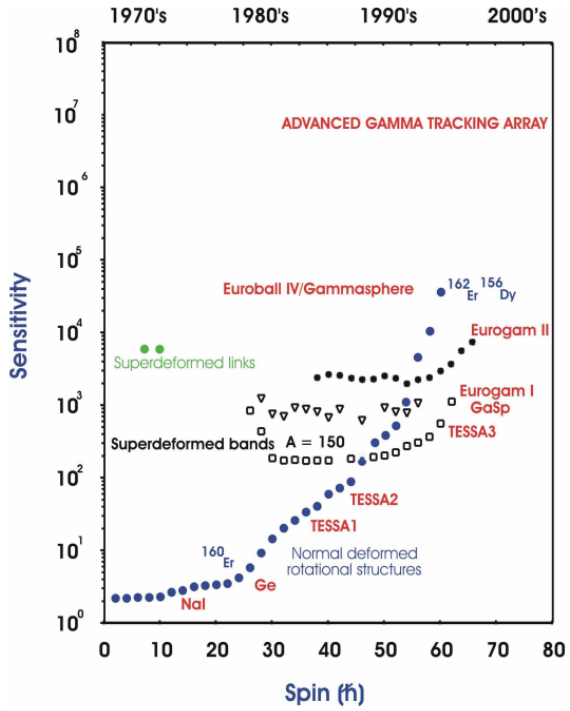

Figure 1.8: This table makes a comparison between different gamma spectrometers and AGATA. On the y axis the sensitivity is plotted as the inverse of the minimum observable intensity against the spin for selected phenomena [6, 7, 8, 9].

1.7 Light charged particle detectors

In fusion-evaporation reactions, particle detectors constitute a useful auxiliary tool for gamma spectrometers. Thanks to the ability to discriminate impinging particles, they can provide a selective trigger signal deducing the charge and mass of the residual nuclei from particle-gamma coincidences. A good efficiency limits the number of high-multiplicity events misinterpreted as low-multiplicity ones and high granularity reduces the probability of multiple-hits. Particle spectrometers can provide Doppler correction to gamma spectrometers. In fact the direction and the energy of the emitting nuclei can be calculated from the angle and the energy of the emitted particles. Particle discrimination generally relies on the consolidated ΔE and E-ΔE techniques implemented respectively in single silicon detectors and in multi-layer telescopes (see figure 1.9). EUCLIDES is an example of silicon telescopic detector. The working principle relies on the Bethe-Bloch

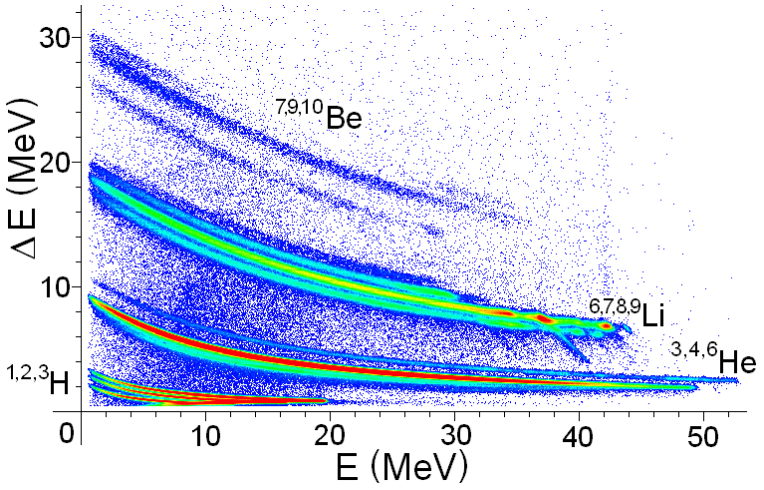

Figure 1.9: Example of $E - \Delta E$ correlation matrix obtained with Micron Semiconductors DSSSDs. Different impinging elements/isotopes are clearly recognisable because they produce separated traces[11].

formula that, for impinging particles considerably heavier than electrons, can be written as follows:

$$-\frac{dE}{dx} = \frac{4\pi}{m_e c^2} \cdot \frac{nz^2}{\beta^2} \cdot \left(\frac{e^2}{4\pi\epsilon_0}\right)^2 \cdot \left[\log\left(\frac{2m_e c^2\beta^2}{I \cdot (1-\beta^2)}\right) - \beta^2\right] \tag{1.1}$$

where v is the speed of the particle, E its energy, x the travelling distance, n is the electron number density of the medium and I the mean excitation potential. As usual c is the speed of light, m_e the rest mass of the electron, e the charge of the electron, ϵ_0 is the vacuum permittivity and $\beta = \frac{v}{c}$. The telescope is made of a first thin silicon layer and a second, thick one. The particles pass through the first and are stopped by the second. Different particles have different mass and charge, leading to a different energy deposition in the two detectors. If we put in a correlation matrix the energy deposited into the two layers respectively on x and y axes, we can reconstruct charge and mass of the impinging particles. In fact each type of impinging particle produce a different pattern in the correlation matrix depending on its charge and mass. With increasing energy of the particle, the amount of energy deposited in the first layer decreases in favour of the one deposited in the second, leading to the characteristic hyperbolic behaviour. This is due to the $1/\beta$ fall of the stopping power in Bethe-Bloch formula. Single ΔE silicon crystals can be used as particle spectrometers, but to work as discriminators they require Pulse-Shape analysis to be performed on the output waveforms. Particles with different

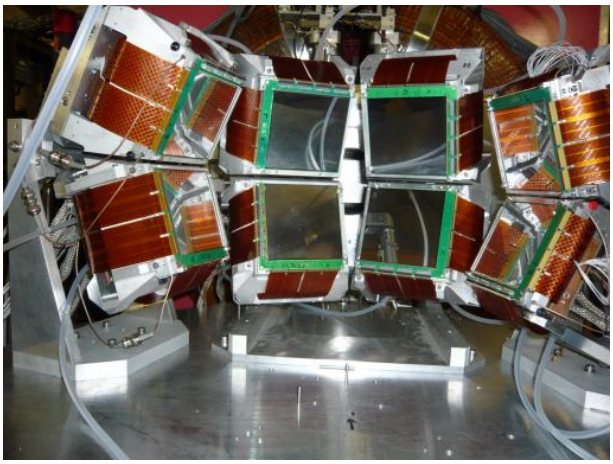

Figure 1.10: Photograph of the MUST2, a telescope array for the detection of the light ions emitted in direct reactions using exotic ion beams. It was built by a collaboration including GANIL, IPN Orsay and IRFU/SPhN.

mass and charge produce their own characteristic interaction inside the detector. The event charge production is thus influenced by the parameters of the impinging particles. These can be thus discriminated looking at the current profiles at the detector electrodes, provided that the preamplifier are fast enough to resolve them. A typical approach in PSA [12] is to correlate either the maximum current or the risetime with the total charge (see figure 1.11).

Particle spectrometers based on silicon detectors are mostly transparent to gamma radiation and thus are very indicated to be used as ancillary for 4π gamma spectrometers, but are not the only solution possible. Also cesium-iodide (CsI) scintillators were employed with good results in 4π arrays such as MICROBALL, GAMMASPHERE, DIAMANT inside EUROBALL. Their energy measurement and particle discrimination is good, but these scintillators are not very transparent to gamma radiation and can produce a higher gamma background due to absorption and scattering phenomena which is almost absent in silicon. For these reasons, future 4π particle spectrometers will conveniently be constituted by silicon crystals. The 4π configuration is envisaged because in direct reactions the products of pickup, stripping and elastic scattering cover the whole angular range. In the study of fusion-evaporation reactions a 4π coverage ensures that most of the reaction products are within the angular acceptance. Beside that also position and angular resolution must comply with stringent requirements, provided that they are limited by the size and angular divergence of the beam spot on the target. A beam angu-

lar uncertainty less than 1 degree, for 1 mm spot, is required. Energy resolution of 50 keV 5 MeV and timing resolution of 500 ps FWHM are required together with a wide dynamic range (from 0.2 to 300 MeV). Present silicon spectrometers are based on strip detectors. The MUST array is made of 8 square silicon strip-Si(Li) telescopes. It is used in GANIL laboratory and has the possibility to be expanded with an additional CsI layer to extend the dynamic range. TIARA is another silicon array which is complementary to MUST. The latter is in fact quite bulky and not very transparent to gamma rays. TIARA, on the other hand, is more compact and can provide a complementary angular coverage. It is made of 8 silicon, 300 μm thick detectors arranged in a barrel-like configuration which ensures a solid angle coverage of 85% of the whole 4π solid angle. It is very transparent to gamma rays and suited to be put in the center of gamma-ray spectrometers but has a naturally limited dynamic range. The evolution of MUST (MUST2, pictured in figure 1.10) is the first silicon array that is based on an ASIC front-end electronics [13].

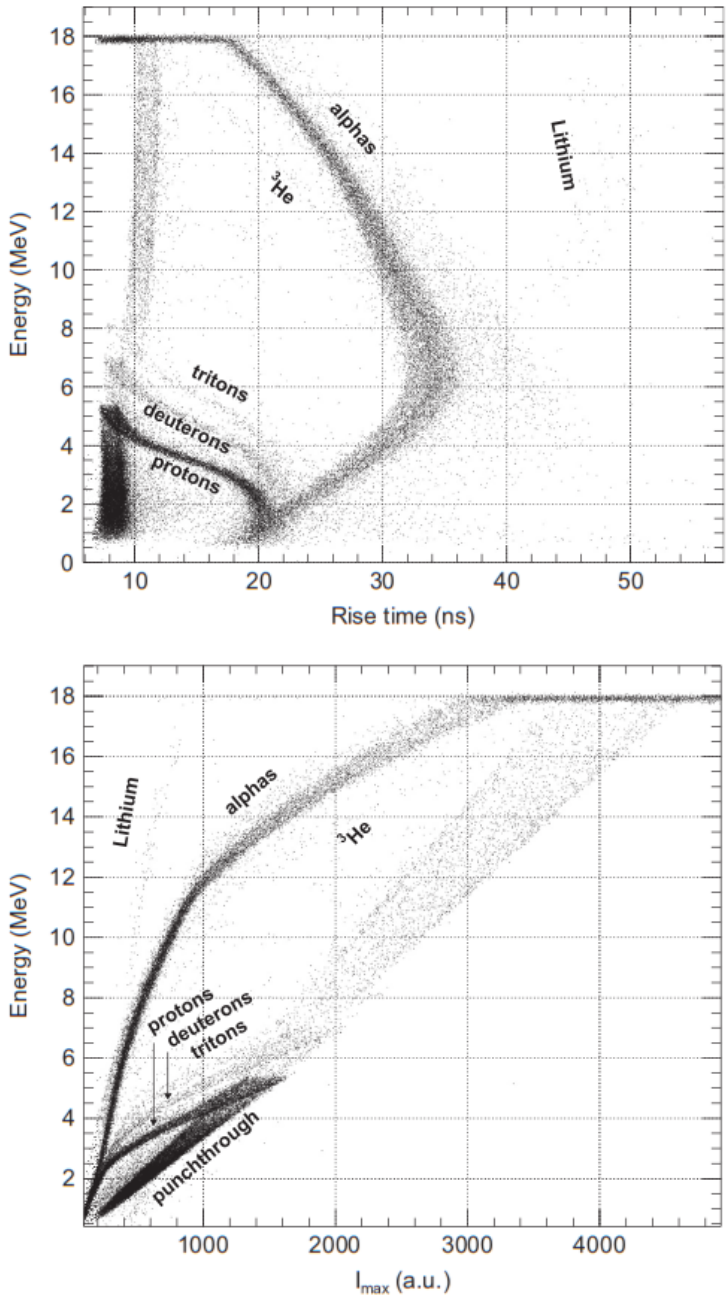

Figure 1.11: Example of correlation matrices obtained with the Pulse-Shape analysis of the signals from the silicon pad detectors of TRACE. The maximum current I_{MAX} and the risetime are plotted against the event energy.

Chapter 2

Front-end electronics for solid-state detectors

The first circuit block of a typical acquisition chain for radiation detectors is the charge preamplifier. Its purpose is to integrate the current coming from the detector producing an analog voltage signal which retains all the necessary information like the amount of charge produced in an event and the current time profile. That information is then used to estimate the energy released by the impinging photon or particle, the position of the interaction and other experimentally relevant quantities. These analog signals can be treated in different ways depending on the purpose of the acquisition and the technology adopted. Energy information can be obtained both with classical all-analogue procedure or with a modern digital one. In the first case the signals are filtered with a spectroscopy shaping amplifier. These filters are designed to receive exponential-decay signals and produce Gaussian-like ones. They are generally insensitive to the baseline level because they implement a baseline restorer. The main purpose of such devices is to maximize the Signal-to-Noise Ratio (SNR). The time constant of these filters can be adjusted in a typical range from 0.1 μs to 10 μs. The optimization of the SNR requires a proper shaping time depending on the spectral composition of the noise coming from the detectors and preamplifiers. Modern techniques require digital sampling of the preamplifier output waveforms. The decay time constant of the preamplifier is typically cancelled out with moving-window deconvolution algorithms and the signals are finally shaped with trapezoidal filters to obtain the energy information. If the experimenter wants to perform particle discrimination or gamma-ray tracking with HPGe detectors, direct analog-to-digital conversion of the preamplifier output waveform is typically adopted, together with the adoption of proper off-line digital algorithms. In some experiments the preamplifier output signals are processed with on-line analog or digital algorithms and only parameters such as energy and risetime are recorded. The possibility to acquire

and save the waveform of an event requires more complex front-end and back-end architecture, but it's a very flexible solution. The experimenter can in fact apply the desired algorithms off-line without getting stuck with the analysis chosen during the acquisition.

2.1 Solid state Detectors

Radiation detectors are liquid, gaseous or solid-state devices [14]. When hit by photons or ionizing particles they produce electronic signals that are processed by the so-called Front-End Electronics (FEE). Although there are many different types of radiation detectors, we will focus only on solid-state ones. A solid detection medium has some great advantages respect to gas-filled detectors. For example, the volume required for the detection of high-energy electrons or gamma-rays can be considerably smaller respect to that of gaseous detectors, due to the higher density. Even if, technically speaking, crystal scintillation counters can be thought of as solid-state detectors, with this term in general we refer only to semiconductor detectors. One of the main drawbacks of crystal scintillation counters is the relatively poor energy resolution. The minimum energy needed to produce a photon is in the order of 0.1 keV. Typical events thus produce some thousands of photons and the statistic fluctuations on such a small number define the limit of the spectroscopic performance. Moreover the process of conversion of the photo-electrons involves a lot of inefficient steps. In the end a typical energy resolution achievable is in the order of 6% for 0.662 MeV gamma-rays. These detectors however have a very good timing resolution.

Semiconductor detectors became available in the early 1960s. In these detectors the radiation-matter or the particle-matter interaction generates electron-hole pairs that are free to move respectively in the conduction and the valence band. These act like electrons-ions couples in gas-filled detectors. The electric field inside the detector separates electrons from holes. The first ones are collected by the anode while the others by the cathode. This process converts all the energy (or only part of it) of the incoming radiation in a current signal. The physical process of interaction lasts some picoseconds and is generally faster than the collection time of the charge carriers, that can be measured in nanoseconds, typically. The signal produced at the terminals of the detector by an event is a delta-like current pulse with area equal to the total amount of charge released in the crystal during the interaction. This charge is generally collected with a Charge-Sensitive Preamplifier (CSP) and converted to an analogue signal. The CSP is an imperfect active

current integrator.

2.1.1 Basic physical considerations on semiconductor detectors

Due to the periodicity of the potential inside crystals, the possible energies of the electrons are confined inside bands [15]. These bands are separated by a range of non-acceptable energies called band-gap. Both for insulators and semiconductors the Fermi energy lies in the middle of the band-gap, thus at T=0 the lower energy band, called "valence band" is full while the upper band, called "conduction band" is empty. The valence band corresponds to those electrons that are bound to specific sites in the crystal while the conduction band describes electrons that can move freely. The energy difference between the two borders of valence and conduction bands determines if the crystal is a semiconductor or an insulator. In case of lower band-gap values ($\approx$1 eV) the thermal excitations can promote electrons from the valence band to the conduction band generating charge carriers that contribute to conduction together with the resulting hole in the valence band: this is the case for semiconductors. If the band-gap is too high (>5 eV) thermal excitations are not able to promote electrons in the conduction band and the crystal behaves as an insulator. In fact the probability of generation of an electron-hole pair per unit time is:

$$p(T) = CT^{3/2} \exp\left(-\frac{E_g}{2kT}\right) \tag{2.1}$$

where T is the absolute temperature, E_g is the band-gap energy, k is the Boltzmann constant and C is a proportionality constant that depends on the material. The exponential term is the cause of the great dependency of such probability from the ratio between the band-gap energy and the absolute temperature. The equilibrium concentration of charge carriers depends also on the recombination probability, dominated by Shockley-Read-Hall, radiative and Auger processes. The free electron concentration n obeys to the Fermi-Dirac distribution, which can be simplified with the Boltzmann equation:

$$n = N_c \exp\left[-\frac{E_c - E_F}{kT}\right] \tag{2.2}$$

where E_c is the energy of the conduction band, E_F is the Fermi energy of the system, T is the temperature of the system and k is the Boltzmann constant. N_c is the effective density of states at the conduction band edge and is equal to:

$$N_c = 2\left(\frac{2\pi m_e^* kT}{h^2}\right)^{3/2} \tag{2.3}$$

where m_e^* is the effective mass of the electron and h is the Planck's constant. Similarly the hole concentration p is equal to:

$$p = N_v \exp\left[-\frac{E_F - E_v}{kT}\right] \tag{2.4}$$

where E_v is the energy of the limit of the valence band and N_v is the effective density of states at the valence band edge and m_h^* is the effective mass of the holes in the valence band.

$$N_v = 2\left(\frac{2\pi m_h^* kT}{h^2}\right)^{3/2} \tag{2.5}$$

Starting from equations 2.2 and 2.4 we can derive the mass action law for the charge carrier densities in an ideal, intrinsic (i.e. non doped) semiconductor crystal, according to which the product of the electron and hole densities depends on the structure of the crystal (N_c and N_v and the band-gap energy E_g) and the temperature:

$$np = n_i^2 = N_c N_v \exp\left(-\frac{E_g}{kT}\right) \tag{2.6}$$

Doping the semiconductor crystal with impurities introduces additional energy levels inside the otherwise prohibited band-gap. For example, if we introduce pentavalent impurities in silicon or germanium, which are tetravalent, the fifth external electron occupies a state which is very close to the conduction band. In fact it doesn't participate in crystal covalent bondings but starts to orbit around the nucleus of the contaminant. The energy required to dislodge it is very low compared to the one required to promote an electron from the valence band to the conduction one. Moreover when the last electron of the contaminant becomes a free-moving electron no hole in the valence band is generated. This kind of impurity is called donor.

Similarly trivalent impurities, known as acceptors, tend to capture in space-localized traps the crystal free-moving electrons, releasing a hole. The energy of the localized electron state introduced by the trivalent impurity is only slightly higher than the one of the valence band edge. Due to their favourable energy level, at room temperature donors and acceptors are completely ionized. If the doping concentration is sensibly higher than the intrinsic charge carrier density of a semiconductor at room temperature, the charge carrier density is almost completely determined by the concentration of the dopant. Moreover, due to the mass action law the number of charge carriers of opposite sign respect to the ones produced by the dopant is almost negligible. With proper doping we can thus control both the conductivity of a semiconductor crystal and the

type of charge carriers. Just to give an example, in intrinsic silicon at room temperature the electron/hole concentration is equal to 10^{10} cm^{-3}. If we dope the silicon with a donor concentration of 10^{17} atoms cm^{-3} the overall electron density will be almost equal to 10^{17} cm^{-3} while the hole concentration will be just in the order of 10^{3} cm^{-3}.

Crystal defects can trap free electrons and behave much like acceptor impurities. Some contaminants like gold, zinc and cadmium, occupying substitutional positions, generate states with energy close to the center of the band-gap. These levels can trap charge carriers for a relatively long period of time. Other impurities can act as recombination centers: they can trap both electrons and holes. All these contaminants are called "Deep impurities", while n and p-type dopants that introduce energy levels near the limits of the band-gap are called "shallow impurities". Recombinations through deep levels is much more probable in crystals than normal recombination between free-running electrons and holes. A good detector crystal should present the lowest possible density of trapping and recombination centers. When an event inside a detector produces a certain number of charge carriers we would like to collect 100% of these at the electrodes, without losing them during their trip across the crystal. A non-optimal detector production process can thus limit greatly the charge collection efficiency, with bad consequences on the spectroscopic properties of the device.

Semiconductor crystals with an equal number of n and p-type dopants behave just like intrinsic semiconductors. They are called "compensated crystals". It is almost impossible to achieve the perfect compensation during the production process, because even minimal local fluctuations in the doping density can lead to n or p-type electrical behaviour. The only practical method to compensate large volumes of silicon or germanium is through lithium ion drifting after the production process [14]. Both in silicon and germanium the purest available crystals behave as p-type semiconductors due to the imperfections in the lattice structure. Thus donor impurities must be added to accomplish the desired compensation. The alkali metals (lithium, sodium, potassium) tend to form interstitial donors. Once ionized, these impurities have good mobility and can travel across the crystal if subject to an electric field. The process begins with the diffusion of a lithium excess on one surface of the detector, forming a n-type region. The Crystal is then reverse biased and heated at $\approx 40^{\circ}$ C to enhance the lithium ion mobility. After several days or weeks part of the lithium has diffused all across the crystal. Almost perfect compensation can be achieved because the lithium distribution spontaneously reaches the configuration where the total space charge is zero at every point. Any departure

from exact compensation has been demonstrated to be an unstable configuration and any imbalance is quickly corrected until uniform concentration is reached. With this method compensation depths of 5-10 mm in silicon and 10-15 mm in germanium were achieved.

N-type doping in semiconductors raise the Fermi energy level above the middle of the band-gap while p-type doping lowers it. This can be easily understood since even in presence of dopants, equations 2.2 and 2.4 are still valid. Two contiguous volumes of semiconductor with different doping type and concentration share the same Fermi energy. This means that the conduction and valence bands must bend in order to match the two Fermi levels. Holes that are majority carriers in the p region diffuse in the n region while electrons from the n-side diffuse in the p-side. This phenomenon is counter-balanced by the electric field generated by the charges themselves. The process reaches the equilibrium state when the diffusion currents are perfectly counterbalanced by the currents induced by the resulting electric field. Such electric field is the cause of the potential which distorts the conduction and valence bands.

For simplicity we perform a 1-dimensional calculus. The first approximation is the following: the motion of charge carriers in the semiconductor is ruled by equations 2.7 and 2.8. The current densities of electrons (J_n) and holes (J_p) are determined by the local electric field E, the mobility factor μ_p and μ_n, the diffusion factors D_p and D_n, the electron and hole density p and n and their respective gradients along the direction of the junction ∇p and ∇n.

$$J_p = -qp\mu_p E - qD_p \nabla p \tag{2.7}$$

$$J_n = -qn\mu_n E + qD_n \nabla n \tag{2.8}$$

Einstein relations state that $D_{p,n} = \frac{kT}{q}\mu_{p,n}$ while the Poisson equation for the electric potential ϕ is:

$$\nabla^2 \phi = -\frac{q}{\epsilon_{Si}} \left(p - n + N_D - N_A\right), \tag{2.9}$$

where N_A and N_D are donor and acceptor densities. The electric potential can also be written as in equation 2.10.

$$\phi(x) = \frac{1}{q}\left(E_F - E_i(x)\right) \tag{2.10}$$

E_F is the Fermi energy, q is the hole charge and $E_i(x)$ the intrinsic Fermi energy. Thanks to equation 2.10 we can thus write the relation between the local electric potential and

the densities of electrons and holes.

$$n = n_i \exp\left(\frac{q\phi(x)}{kT}\right) \tag{2.11}$$

$$p = p_i \exp\left(-\frac{q\phi(x)}{kT}\right), \tag{2.12}$$

where n_i and p_i are the intrinsic concentrations of charge carriers. The principle of detailed balance states that:

$$\frac{n(x)}{n(x')} = \exp\left[\frac{q}{kT}\left(\phi(x) - \phi(x')\right)\right] \tag{2.13}$$

$$\frac{p(x)}{p(x')} = \exp\left[-\frac{q}{kT}\left(\phi(x) - \phi(x')\right)\right] \tag{2.14}$$

Obviously $\nabla\phi = \frac{kT}{q}\frac{1}{n}\nabla n = -E$. For temperatures at which the quasi-neutrality approximation stands we can say that $n \approx N_D$ and $p \approx N_A$. In this case the built-in junction potential ϕ_i (the potential between the p and n-type regions of the junctions due to electric field induced by charge carrier diffusions) is equal to:

$$\phi_i = \frac{kT}{q}\log\frac{N_A N_D}{n_i^2}. \tag{2.15}$$

Due to the high dopant gradient at the interface of the junction, electrons diffuse from the n-zone into the p-zone (and vice versa for holes), leaving ionized impurities non compensated until the Fermi energy becomes equal across the junction. We perform now the electrostatic analysis of the system according to the complete depletion approximation, as indicated in equation 2.16. This approximation implies that when charge carriers diffuse from one side of the junction to the other, they generate two distinct and contiguous areas of the crystal with space-localized charges and no free moving charge carriers. In real semiconductors these zones are not precisely delimited because the charge carrier densities are continuous functions of the space.

$$\begin{cases} p(x) = N_A & \text{for} \quad -L_p < x < -x_p \\ p(x) = 0 & \text{for} \quad -x_p < x < 0 \\ n(x) = 0 & \text{for} \quad 0 < x < x_n \\ n(x) = N_D & \text{for} \quad x_n < x < L_n \end{cases} \tag{2.16}$$

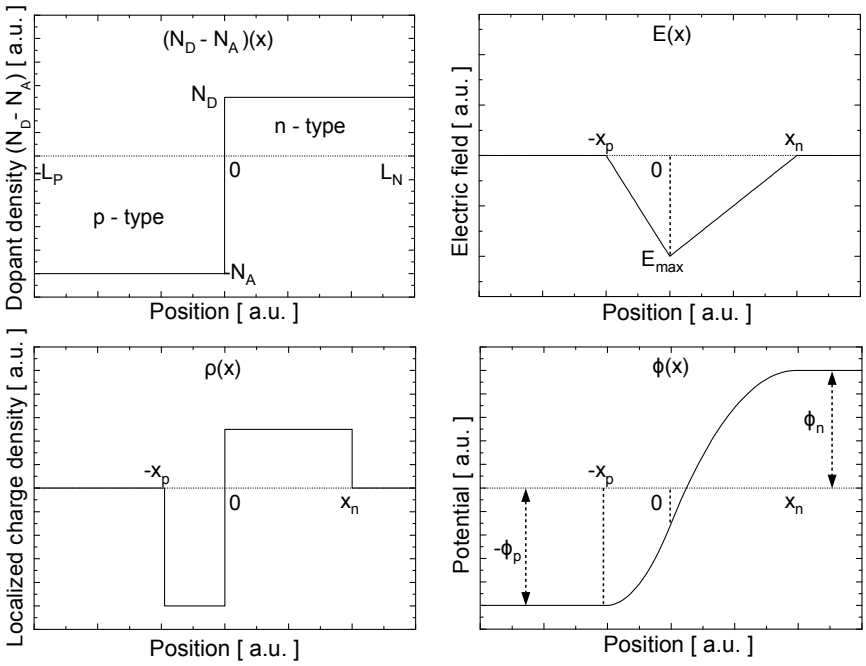

Figure 2.1: Relevant physical quantities of the non biased p-n junction. From upper-left in clockwise order: the dopant density $N_D - N_A$, the electric field E(x), the electric built-in potential $\phi(x)$ and the localized charge density $\rho(x)$. All units are arbitrary. The diode extends from $-L_P$ to L_D. The interface between the p-doped and n-doped zones is placed at $x = 0$. The depletion region starts at $-x_p$ and ends at x_n.

We thus write the Poisson equation considering $\rho(x)$ as follows:

$$\frac{d^2\phi}{dx^2} = -\frac{\rho(x)}{\epsilon_{Si}} \tag{2.17}$$

$$\begin{cases} \rho(x) = 0 & \text{for} \quad -L_p < x < -x_p \\ \rho(x) = -qN_A & \text{for} \quad -x_p < x < 0 \\ \rho(x) = qN_D & \text{for} \quad 0 < x < x_n \\ \rho(x) = 0 & \text{for} \quad x_n < x < L_n \end{cases} \tag{2.18}$$

After straightforward calculations, since:

$$\begin{cases} \frac{d^2\phi}{dx^2} = \frac{qN_A}{\epsilon_{Si}} \\ E(x) = -\frac{qN_A}{\epsilon_{Si}}(x + x_p) \end{cases} \qquad -x_p < x < 0 \tag{2.19}$$

for the p-doped region we obtain that:

$$\phi(x) = \frac{qN_A}{2\epsilon_{Si}}(x + x_p)^2 + \phi_p \qquad -x_p < x < 0. \tag{2.20}$$

In the same way we can calculate both the electric field and potential in the n-doped region ($0 < xL_n$).

$$\begin{cases} \frac{d^2\phi}{dx^2} = -\frac{qN_D}{\epsilon_{Si}} \\ E(x) = -\frac{qN_D}{\epsilon_{Si}}(x_n - x) \end{cases} \qquad -x_p < x < 0 \tag{2.21}$$

$$\phi(x) = -\frac{qN_D}{2\epsilon_{Si}}(x_n - x)^2 + \phi_n \qquad 0 < x < x_n \tag{2.22}$$

The solutions for the p-doped region ($x < 0$) and n-doped region ($x > 0$) must be joined so as to obtain continuous functions in $x = 0$.

$$\begin{cases} E(0^-) = E(0^+) \\ \phi(0^-) = \phi(0^+) \end{cases} \tag{2.23}$$

This condition is used to determine x_p, x_n given the dopant densities.

$$\begin{cases} x_p N_A = x_n N_D \\ \frac{qN_A}{2\epsilon_{Si}}x_p^2 + \phi_p = -\frac{qN_D}{2\epsilon_{Si}}x_n^2 + \phi_n \end{cases} \tag{2.24}$$

The width of the depletion region is thus equal to

$$x_d = x_p + x_n = \sqrt{\frac{2\epsilon_{Si}}{q}\left(\frac{1}{N_A} + \frac{1}{N_D}\right)\phi_i} \tag{2.25}$$

and substituting this value into equation 2.24 we can obtain the maximum electric field $E_{MAX} = \frac{2\phi_i}{x_d}$ (see figure 2.1). If we consider for example a p-n junction in Silicon ($\epsilon_{Si} = 1.04 \cdot 10^{-12}$ Fcm^{-12}) with an acceptor concentration $N_A = 4 \cdot 10^{18}$ cm^{-3} and a donor concentration of $N_D = 4 \cdot 10^{16}$ cm^{-3} the built-in potential is equal to 0.83 V, the maximum electric field is $-5 \cdot 10^4$ Vcm^{-1} and, since $x_n = 400x_p$ we can conclude that $x_d \approx x_n = 328$ nm.

If we apply a voltage difference to the junction we perturb the natural thermodynamic equilibrium and the Fermi energy level loses its meaning. In case of biased junction we must refer to "Quasi-Fermi" or "Imref" levels. These are like the Fermi energy level but

stand separately for electrons and holes. In fact E_{Fn} is the Imref level for electrons while E_{Fp} is the one for the holes. The Maxwell-Boltzmann statistics is still valid, but with the new formulation in equations 2.26 and 2.27.

$$n = n_i \exp\left[\frac{E_{Fn} - E_i}{kT}\right] \tag{2.26}$$

$$p = p_i \exp\left[-\frac{E_{Fp} - E_i}{kT}\right] \tag{2.27}$$

We can thus write the new mass action law for systems in quasi-equilibrium, that can be easily deducted from equations 2.26 and 2.27.

$$np = n_i^2 \exp\left[\frac{E_{Fn} - E_{Fp}}{kT}\right] = n_i^2 \exp\left[-\frac{qV_R}{kT}\right] \tag{2.28}$$

$$E_{Fn} - E_{Fp} = qV_R \tag{2.29}$$

The difference between the Imref levels is a measure of the deviation from the thermal equilibrium. Practically we can say that in these conditions electrons and holes obey to their own Fermi distribution separately. In fact both photo-excitation and electron-hole recombination have a lifetime of $\approx 10^{-9}$ s. The SRH recombination of injected minority carriers have a characteristic lifetime of $\approx 10^{-6}$ s. Electron-electron, hole-hole, electron-phonon and hole-phonon interactions have a characteristic time of $\approx 10^{-13}$ s. This means that charge carriers of the same kind are in thermodynamic equilibrium between them. The thickness of the depleted zone can be easily deducted from 2.25. The localized charge at the junction interface must follow the electrostatic Poisson equation with the proper boundary conditions imposed by the applied voltage.

$$x_d = x_p + x_n = \sqrt{\frac{2\epsilon_{Si}}{q}\left(\frac{1}{N_A} + \frac{1}{N_D}\right)(\phi_i + V_{EXT})} \tag{2.30}$$

Semiconductor detectors work following this simple principle. The interaction with particles or photons promote electrons from the valence band to the conduction band (and the opposite can be said for holes). The number of charge carriers produced is directly proportional to the energy deposited inside the crystal and thus retains the desired information. Bigger the dimensions of the detectors, larger both the probability of interaction and the possibility that all the energy of the incoming radiation is completely deposited inside the crystal. Once the charge carriers are promoted, they must be collected at the electrodes in order to be measured. If accidentally these charge carriers recombine with

other charge carriers naturally present in the semiconductor, the energy information can be deteriorated or completely lost. Since the probability of recombination of interaction-induced charge carriers depends on the number of already present free charge carriers of the semiconductor, we should deplete the crystal from its thermally generated charge carriers in order to maximize the collection efficiency. This is accomplished by means of a reverse-biased junction. Detectors are typically made of a thin highly doped n-contact coupled with an almost intrinsic p-type volume. This one is not intentionally doped but contains impurities and crystallographic defects that act as p-dopants. Pollutants can come for example from the crucible during the ingot melting, while the crystallographic defects are naturally originated during the crystal growth. If $N_D \gg N_A$, equation 2.30 can be simplified.

$$x_d = x_p + x_n = \sqrt{\frac{2\epsilon_{Si}}{q}\left(\frac{1}{N_A}\right)(\phi_i + V_{EXT})} \tag{2.31}$$

The lower the defect and pollutant density in the p region, the larger the width of the depleted zone. Great effort has been spent in recent years to minimize the crystallographic defect and pollutant densities in order to enhance the depletion thickness. One of the most common method is called "zone refining" or "floating zone" process. Induction coils or resistance heaters melt a little portion of the semiconductor ingot. Moving the heaters respect to the ingot changes the position of the molten zone which "travels" across the length of the ingot. Impurities are more likely to diffuse in the molten zone than to be trapped in the solid one. This means that the moving molten zone collects a great part of the impurities, leaving behind a solid ingot purer than before. This process can be repeated several times, leaving the impurities at the end of the semiconductor ingot. In germanium the lowest impurity density achieved is in the order of 10^{10} impurities/cm^2. Detectors with such degree of purity are defined HPGe (High Purity Germanium) and can achieve a depletion thickness of 10 mm with reverse bias voltages of less than 1000 V. Silicon detectors are generally thinner (between some hundreds of microns and 1-1.5 mm) due to the limitation in maximum depletion thickness induced by the higher impurity concentration. A typical value for silicon detectors is 10^{12} impurities/cm^2. Another difference between silicon and germanium is the amount of black current. Silicon has a larger band-gap (1.12 eV) respect to germanium (0.67 eV) and thus has a lower number of free charge carriers produced by thermal excitation as written in equation 2.1. For this reason silicon detectors can be operated at room temperature keeping the leakage

current at acceptable levels. Germanium detectors, on the other hand, must be cooled down to cryogenic temperatures before being biased otherwise the high leakage currents can destroy the crystals. Germanium is favoured in gamma spectroscopy because of its higher cross section. This is due to its higher atomic number (Z = 32) respect to silicon (Z = 14). Silicon is on the other hand favoured in the detection of low-energy gamma rays, X rays and charged particles. Since any variation of the reverse bias voltage leads to a change in the width of the depleted region (and also a change in the amount of localized charge) we can evaluate, for a determined bias condition, the equivalent parasitic capacity of the junction. Starting from equation 2.30 we can calculate the small-signal junction capacitance.

$$C = \frac{dQ}{dV_R} \tag{2.32}$$

In case of unilateral junction (as in equation 2.31)

$$dQ = qN_D dx_n \tag{2.33}$$

and

$$\frac{dQ}{dV_R} = q_N D \frac{dx_n}{dV_R}. \tag{2.34}$$

This leads to a simple expression for the small-signal junction capacitance.

$$C(V_R) = \frac{\epsilon}{x_n(V_R)} \tag{2.35}$$

$$\frac{1}{C^2} = \frac{2}{q\epsilon N_D}(\phi_i + V_R) \tag{2.36}$$

When designing a charge sensitive preamplifier this is an important parameter to be taken into account, since it affects both the speed and the noise performance of the circuit. Photon (X or gamma) interaction is precisely localized in a single point in space and is based on some well-known physical phenomena, such as photoelectric absorption, Compton scattering and pair production. Each of these has its own cross-section which is energy-dependent. Charged particles interact in a different way. They progressively lose energy while they travel into the detector crystal, leaving traces of ionized electron-hole pairs. The length of these traces depends on the energy of the impinging particle (the higher the energy, the longer the trace). Such ionization is produced by the interaction of the particle's electric field with the detector. The differential energy loss for a particle

travelling into a medium is described by the Bethe-Bloch formula.

$$-\frac{dE}{dx} = \frac{4\pi}{m_e c^2} \cdot \frac{nz^2}{\beta^2} \cdot \left(\frac{e^2}{4\pi\varepsilon_0}\right)^2 \cdot \left[\ln\left(\frac{2m_e c^2\beta^2}{I \cdot (1-\beta^2)}\right) - \beta^2\right] \tag{2.37}$$

In equation 2.37 n and I are respectively the detector's electron density and electron mean excitation potential. z is the atomic number of the impinging particle. Integrating this equation we can calculate, for example, that an electron with energy equal to 200 keV can travel across a 300 μm-thick silicon detector, emerging from the opposite side and not being stopped. Since for high values of β the spatial derivative of the energy loss dE/dx tends to become constant, the amount of charge released in a detector by high-energy particles is almost independent from the energy. These particles are called "Minimum Ionizing Particles" or simply "MIP". Both in case of photons or particles, the number of charge carriers released during the interaction is not exact but obeys to a statistical distribution. This aspect is relevant since we measure the energy of the incoming radiation from the total charge released in the detector. If each electron-hole ionization was completely independent from the others the total number of charge carriers released per unit energy would follow the Poisson distribution, but this model is not correct. In fact there is a strong correlation between successive ionizations, leading to a different distribution for the total charge released per unit energy. This effect is called "Fano effect". The practical consequence is that the standard deviation σ of the number of electron released is smaller than the square root of the mean electron number N.

$$\sigma = \sqrt{0.12N} \tag{2.38}$$

The correction factor 0.12 is thus called "Fano factor". When measuring the energy of the incoming radiation the two sources of uncertainty are the intrinsic broadening σ_{FANO} and the electronic noise (ENC). Since these two values are not correlated, they sum up quadratically. The total error of the measure (σ^2_{TOT}) is equal to

$$\sigma^2_{TOT} = \sigma^2_{FANO} + ENC^2. \tag{2.39}$$

If E is the photon energy and χ is the energy required to produce a single electron-hole pair (3.6 eV in silicon), the error in the energy measurement is equal to:

$$\sigma_{TOT} = \sqrt{0.12\frac{E}{\chi} + ENC^2}. \tag{2.40}$$

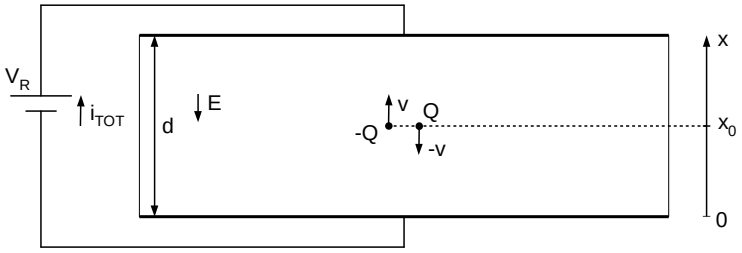

Figure 2.2: Scheme of a fully depleted detector in which a group of electron-hole pairs is generated at distance x_0 from the cathode. V_R is the reverse bias voltage of the fully depleted detector of thickness d. Due to relations 2.41 the charge carriers move along the electric field lines according to their charge sign.

Let's now calculate the shape of the current signals induced by interaction with incoming radiation. At this purpose we make the following assumption. If we apply to the detector a reverse bias higher than the one needed to deplete it completely, we accumulate charge on the surfaces like in a capacitor. The electric field induced by these charges sums up with the one induced by localized charges inside the depleted region. In case of high over-depletion the electric field inside the detector can be approximated to the one of a capacitor (i.e. constant in the volume between the plane, parallel plates). Being this electric field high enough, electrons and holes drift inside the semiconductor at fixed speed, equal to the product of the electric field E and the mobility coefficient μ of the charge carrier (see figure 2.2). Electrons and holes have different mobilities (μ_n and μ_p).

$$\begin{cases} v_p = \mu_p \cdot E \qquad \mu_p \approx 450 \dfrac{cm^2}{V \cdot s} \quad \text{for holes in Si} \\ \\ v_n = -\mu_n \cdot E \qquad \mu_n \approx 1200 \dfrac{cm^2}{V \cdot s} \quad \text{for electrons in Si} \end{cases} \tag{2.41}$$

This approximation holds generally for electric fields lower than 4000 V/cm since over this threshold the speed of the carriers saturates to a limit-value and thus the electric field and the drift velocities of the carriers are no more proportional. In order to deduce the analytical expression of the current produced by a detector let us start with the description of a simple model. We consider a point-like interaction (photon interaction). We describe the detector as a capacitor with parallel and plane plates. Their dimensions are big compared to their reciprocal distance d so that the conditions of complete induction are satisfied. Let us also assume to have complete depletion of the crystal (or better,

over-depletion). The detector is biased with a reverse voltage V_R produced by an ideal generator. The electric field inside the detector is thus constant and equal to $E = \frac{V_R}{d}$. Such electric field is responsible for the drift of free charge carriers inside the depleted region of the detector (that in our model is the dielectric between the plates) according to equation 2.41. Once an electron-hole pair with charge $\pm q$ and mobility factor μ_p and μ_n is generated inside the depleted region at distance x_0 from the cathode, each charge carrier starts travelling along the electric field lines. Such drift is made possible because of the work $\vec{L}$ of the electric field on the charge itself. The instantaneous power P of the Coulomb force ($\vec{F} = \pm q\vec{E}$) on each charge carrier is equal to:

$$P_p = \frac{d\vec{L_p}}{dt} = +q\vec{E}\frac{d\vec{x_p}}{dt} = q\vec{E}\cdot\vec{v} = q\mu_p\frac{V_R}{d} \tag{2.42}$$

$$P_n = \frac{d\vec{L_n}}{dt} = -q\vec{E}\frac{d\vec{x_n}}{dt} = -q\vec{E}\cdot\vec{v} = q\mu_n\frac{V_R}{d}. \tag{2.43}$$

Please notice that, since electrons and holes have opposite charge, they travel in opposite directions inside the detector: electrons towards the anode and holes towards the cathode. However the power delivered from the electric field has the same sign regardless of the carrier's charge sign. If N electron-hole pairs are generated at once in the same position x_0, since we assume that all the electrons are travelling together (and the same happens to holes), equations 2.42 and 2.45 become:

$$P_p = \frac{d\vec{L_p}}{dt} = +qN\vec{E}\frac{d\vec{x_p}}{dt} = qN\vec{E}\cdot\vec{v_p} = qN\mu_p\left(\frac{V_R}{d}\right)^2 \tag{2.44}$$

$$P_n = \frac{d\vec{L_n}}{dt} = -qN\vec{E}\frac{d\vec{x_n}}{dt} = -qN\vec{E}\cdot\vec{v_n} = qN\mu_n\left(\frac{V_R}{d}\right)^2. \tag{2.45}$$

Since this power must be supplied by the voltage generator and knowing that the power is equal to the product of the voltage and the current, we can easily calculate the current induced at the electrodes by the moving electrons and holes.

$$i_p = \frac{qN\mu_p V_R}{d^2} \tag{2.46}$$

$$i_n = \frac{qN\mu_n V_R}{d^2} \tag{2.47}$$

A more accurate demonstration of this phenomenon is the Shottky-Ramo theorem, which analysis is beyond this work's aim. Such currents last until each group of charge carriers has reached the corresponding electrode. Being the distances to be covered equal to x_0 for

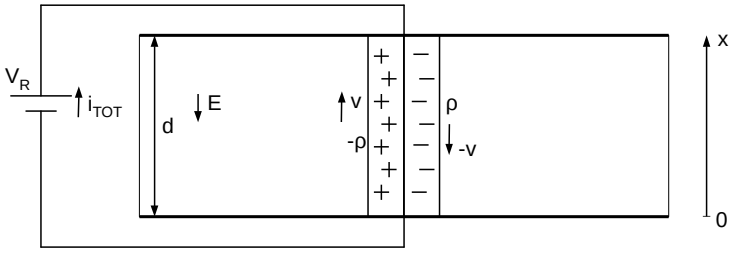

Figure 2.3: Scheme of a fully depleted detector in which a continuous distribution of electron-hole pairs is generated along a line across the whole thickness of the detector. The linear charge densities are $\pm\rho$. V_R is the reverse bias voltage of the fully depleted detector of thickness d. Due to relations 2.41 the charge carriers move along the electric field lines according to their charge sign.

the holes and $d - x_0$ for the electrons, the durations of the hole and electron components of the induced current are:

$$t_p = \frac{x_0}{\mu_p E} \tag{2.48}$$

$$t_n = \frac{d - x_0}{\mu_n E} \tag{2.49}$$

The overall current signal induced by an event occurred at $t = 0$ which produces N electron-hole pairs at distance x_0 from the cathode is:

$$i_{TOT}(t) = i_p(t) + i_n(t) \qquad \text{where} \qquad \begin{cases} i_p = \dfrac{qN\mu_p V_R}{d^2} & \text{for} \quad 0 < t < t_p \\ \\ i_n = \dfrac{qN\mu_n V_R}{d^2} & \text{for} \quad 0 < t < t_n \end{cases} . \tag{2.50}$$

The integral of the current is as expected equal to qN, because at the end of the collection process, the whole generated charge is deposited on the electrodes. Please notice that this current is directed from the anode to the cathode. If the interaction is not point-like as happens for photons but is distributed along the whole thickness of the detector, the current profile will be different. This is the case for minimum ionizing particles (MIP) as in figure 2.3. The total charge produced is Q and the linear charge density along the trace is $\rho = \frac{Q}{d}$. The height $h_{p,n}$ of the charge distributions decreases with time following the equation:

$$h_p(t) = d - q\mu_p \frac{V_R}{d} t \qquad \text{for} \quad 0 < x < \frac{d}{v_p} \tag{2.51}$$

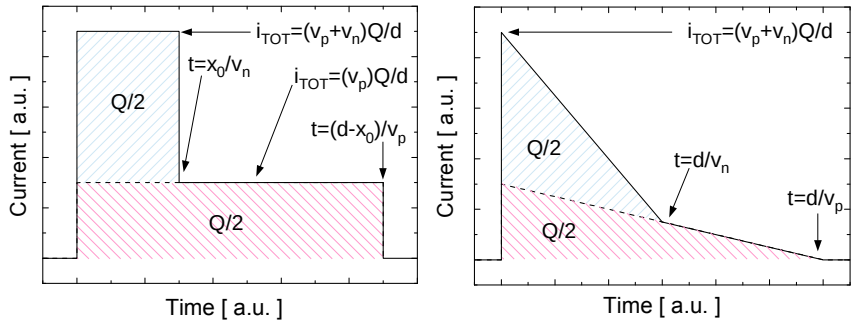

Figure 2.4: Left: time diagram of the current produced in a detector by a point-like interaction that produces a charge equal to Q. Right: time diagram of the current produced in a detector by the interaction of a MIP. Please notice that in both cases the electron and hole current function have area equal to $Q/2$ and that their sum is equal to Q which is the total charge produced in the event.

$$h_n(t) = d - q\mu_n \frac{V_R}{d} t \qquad \text{for} \quad 0 < x < \frac{d}{v_n}. \tag{2.52}$$

The expressions of the current induced at the electrodes by holes and electrons at a given time are:

$$i_p(t) = \int_0^{h_p(t)} \frac{\rho\mu_p V_R}{d^2} dh = \frac{\rho\mu_p V_R}{d^2} \cdot \left(d - q\mu_p \frac{V_R t}{d} \right) = \frac{Q}{d^2} v_p \left(d - v_p t \right) \tag{2.53}$$

$$i_n(t) = \int_0^{h_n(t)} \frac{\rho\mu_n V_R}{d^2} dh = \frac{\rho\mu_n V_R}{d^2} \cdot \left(d - q\mu_n \frac{V_R t}{d} \right) = \frac{Q}{d^2} v_n \left(d - v_n t \right) \tag{2.54}$$

These currents have a maximum in $t = 0$: $i_p(0) = \frac{Q}{d} v_p$ and $i_n(0) = \frac{Q}{d} v_n$. The expression of the total current at the electrodes is:

$$i_{TOT}(t) = i_p(t) + i_n(t) \quad \text{where} \quad \begin{cases} i_p(t) = \dfrac{Q}{d^2} v_p \left(d - v_p t \right) & \text{for} \quad 0 < x < \frac{d}{v_p} \\ \\ i_n(t) = \dfrac{Q}{d^2} v_n \left(d - v_n t \right) & \text{for} \quad 0 < x < \frac{d}{v_n}. \end{cases} \tag{2.55}$$

It is clear that the analysis of the current profiles (figure 2.4) can provide more information than the simple energy released inside the detector. In fact Pulse-Shape Analysis (PSA) is adopted for various tasks. For example in AGATA it is used to reconstruct the position of interaction of gamma rays inside the detector while in particle spectroscopy it is used to discriminate the impinging ions both in atomic number and mass. From now

on we will use a very simple model of solid-state detector, made of a parasitic capacitance C_{DET} and current generator i_{DET} with associated noise source. Both in simulations and in experiments on the test-bench the detector is simulated with a step-like voltage generator connected to the charge-sensitive preamplifiers through a test capacitor C_{DET}. If we want to inject in the CSP a charge equal to Q the voltage step amplitude must be equal to $V_{TEST} = \frac{Q}{C_{TEST}}$. Let's now concentrate on charge-sensitive preamplifiers, analysing their working principles, their noise sources and the techniques to optimize them.

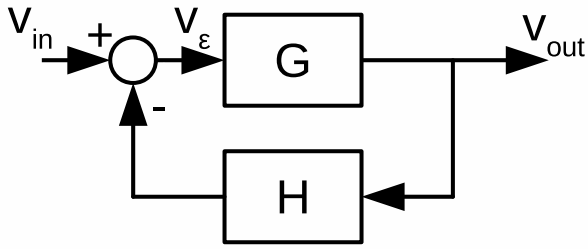

Figure 2.5: Pictorial view of a feedback amplifier

2.2 Charge-Sensitive Preamplifiers

2.2.1 Theory of negative feedback amplifiers

Negative feedback amplifiers are a class of circuits where the output signal $\tilde{v}_{out}(\omega)$ is "feed back" and mixed to the input signal $\tilde{v}_{in}(\omega)$ after being multiplied by a proper transfer function $\tilde{H}(\omega)$. Please notice that throughout this chapter we will refer to signals using the following formalism:

- $v(t)$ is the small signal in the time domain
- $\tilde{v}(\omega)$ is the small signal in the frequency domain
- $H(t)$ is the response function in the time domain of a system that receives a δ-like function at the input
- $\tilde{H}(\omega)$ is the response function in the frequency domain or "transfer function" of a system with time-domain input response function $H(t)$.

A negative feedback amplifier can be described with two blocks, G and H, as pictured in figure 2.5. The system obeys to equation 2.56.

$$\frac{\tilde{v}_{out}(\omega)}{\tilde{v}_{in}(\omega)} = \frac{\tilde{G}(\omega)}{1 + \tilde{G}(\omega)\tilde{H}(\omega)} \tag{2.56}$$

In equation 2.5 $\tilde{G}(\omega)$ and $\tilde{H}(\omega)$ stand for the transfer function in the frequency domain of the G and H blocks. In the limit of $\tilde{G}\tilde{H} \gg 1$ the expression tends to $\frac{\tilde{v}_{out}}{\tilde{v}_{in}} \to \frac{1}{\tilde{H}}$.
In fact, from an historical point of view the idea of a negative feedback amplifier comes from the need to design linear circuits with predictable gain even if the active components at disposal have great non-linearities and unstable or unpredictable gain. With this

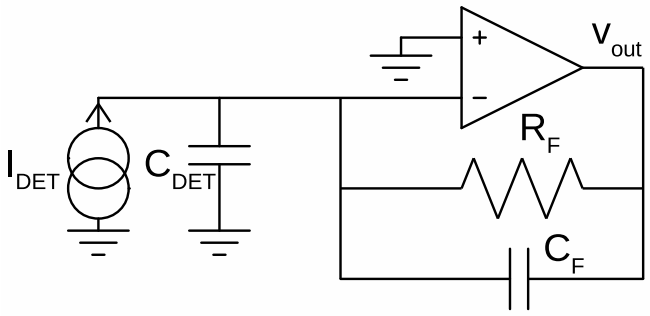

Figure 2.6: Pictorial view of a charge-sensitive preamplifier

technique, for all the frequencies where $\tilde{G}\tilde{H} \gg 1$ the gain of the circuit depends only marginally from the active high-gain block G. The behaviour of the circuit depends more or less only on the feedback block H, which is generally made with passive components and thus is more stable in time and temperature and with a more predictable transfer function. A negative feedback amplifier is stable only if the system respect the Nyquist stability criterion or the simpler but equally effective Bode criterion about phase and gain margins. Thinking at G as a realistic bandwidth-limited system, the Bode criterion says that stability is ensured in closed-loop configuration if the frequency at which the gain becomes unitary (f_0) is lower than the frequency at which the phase shift becomes π (f_π). This rule imposes some restrictions on the positions of the poles and zeroes of the system, but in electronics these requirements are usually met. In fact operational amplifiers are generally compensated with a low-frequency pole. This ensures that all the following parasitic poles are placed at so high frequency that the corresponding gain is well under unity. The distance in dB between the loop gain at f_π and unity is called gain margin. On the other hand the distance between (f_0) and (f_π) is called the phase margin.

2.2.2 From theory to application: circuit structure of a CSP

The simplified schematic of a charge-sensitive preamplifier is represented in figure 2.6. The detector is schematically depicted with a current generator and a capacitor. The first one represents the charge carrier production due to events inside the detector, while the second one is a good model of the parasitic capacitance of the p-n junction of the depleted detector. A charge-sensitive preamplifier is a negative feedback amplifier with capacitive

feedback. The feedback capacitance determines the closed-loop gain of the circuit that is the report between the amplitude of the output waveforms and the amount of charge produced inside the detector. The feedback resistance is used to ensure correct operation of the amplifier settling the DC operating point. It also avoids a constant saturation of the preamplifier providing a continuous discharge of the feedback capacitor. Let's now study the circuit's response function to a delta-like current pulse at the input. At the moment we consider the operational amplifier as an ideal one with infinite gain and no bandwidth limitations.

$$i_{in}(t) = Q\delta(t) \tag{2.57}$$

$$v_{out}(t) = -\theta(t)\frac{Q}{C_F}e^{-\frac{t}{\tau_F}} \tag{2.58}$$

In equation 2.58 $\tau_F = R_F C_F$. The feedback resistance and capacitor determine the time constant of the preamplifier. As we see later in this chapter this parameter must be selected with accuracy since both C_F and R_F are critical components in the circuit, both for the dynamical properties of the preamplifier and for the noise performance. Translating equations 2.57 and 2.58 into the frequency domain we obtain the ideal preamplifier's transfer function.

$$\tilde{v}_{out}(\omega) = -\frac{1}{C_F}\frac{\tau_F}{1+s\tau_F} = -\frac{R_F}{1+s\tau_F} \tag{2.59}$$

From and electronic point of view the detector is a current generator that produces delta-like current pulses. Those pulses have finite area equal to Q, which is the total charge of the carriers promoted to conduction band during an event inside the crystal structure. The time required by these carriers to travel across the detector and reach anode and cathode depends on the detector thickness and bias voltage. However it is in the order of 10-15 ns for thin silicon detectors and 100-150 ns for thick germanium ones. The total charge produced by an event is proportional to the energy released inside the detector while the current profiles gives us different pieces of information, such as position and type of the interaction. The analysis of the current profile, under certain conditions, enables the experimenter to distinguish between different particles impinging on the detector.

2.2.3 Types of noise sources

In this section we will describe all the different noise sources that appear in a circuit. Ideally they are always connected to dissipative devices but never to conservative ones.

For this reason, in first approximation, noise sources are connected to resistors, diodes and transistors but not to condensers. This is a first-order consideration, since in reality things show to be quite different. In fact also condensers can induce noise inside the electronic circuits due to a noise source called dielectric noise. The following list includes the most common kinds of noise.

- "Thermal" or "Johnson" noise. A resistance at a given temperature generates at its poles a noise due to the random thermal movement of the charge carriers inside it. The spectrum is white upon a very wide bandwidth. The spectral noise density is equal to $4KTR$, where K is the Boltzmann constant, R the value of the resistor and T the temperature of operation.

- "Shot noise". This noise source is generated by a current flowing through a potential barrier due to its granularity.

- $1/f$ noise. This noise is present in every physical process. Its demonstration generally takes place from cosmological means. In semiconductors it is generally referred to the composition of several Lorentzian noise sources. The spectral noise density is proportional to $\frac{A}{f}$ where f is the frequency. From a mere mathematical calculation the integral of this spectral density of noise should diverge while f approaches 0. In reality this doesn't happen because of the simple principle that, in the end, every measurement is limited in time.

- "Lorentzian" noise. In semiconductors this noise is generated by trap-detrap phenomena of charge carriers inside the non ideal crystal structure.

- "K-T-C" noise. This kind of noise source is generated by the sampling of a voltage reference on a capacitor through a resistor.

"Thermal" or "Johnson" noise

As stated before, a resistance at a given temperature produces noise at its nodes due to the chaotic movement of the charge carriers inside. The noise spectrum is white within a very wide bandwidth. Thanks to the well known theorems about Thevenin and Norton equivalent circuits, this noise source can be represented both with a current and a voltage noise generator, as can be seen in figure 2.7. The theoretic demonstration of this result is quite straightforward. First of all lets imagine to build an ideal circuit made of a realistic noisy resistance of value R connected to an ideal transmission line

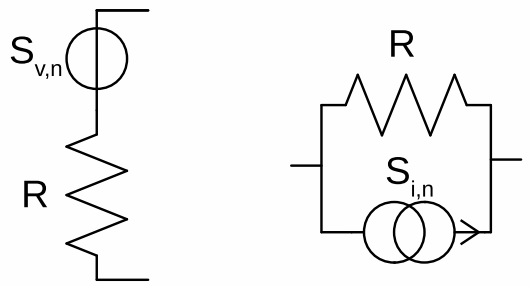

Figure 2.7: Figure on the left: the voltage noise source referred to a resistance R. The physical spectral noise density is equal to $S_{v,n} = 4kTR$. Figure on the right: current noise source associated with a resistance R. The physical spectral noise density is equal to $S_{i,n} = \frac{4kT}{R}$. T is the temperature, R the value of the resistance and k is the Boltzmann constant.

of characteristic impedance R as in figure 2.8. The transmission line is shorted on the other side. There is a switch connected between the two extremes of the resistor. We wait for the system to thermalize leaving the switch open. Then we close the switch. After having closed the switch, the energy stored inside the transmission line generates

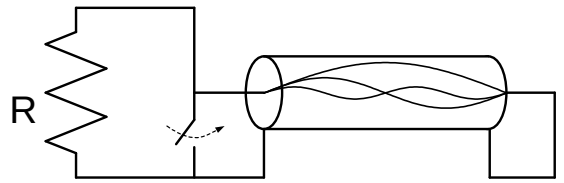

Figure 2.8: Pictorial view of the ideal circuit used to demonstrate the formula of the spectral noise density of the thermal noise. The transmission line has a characteristic impedance equal to R.

a standing electric wave constantly reflected at the two extremes. The transmission line has become an unidimensional resonating cavity of length L. This physical system obeys to the laws of the black body. First of all we notice that the only wavelength λ allowed inside the cavity are the ones that fulfil equation 2.60.

$$\lambda_n = \frac{2L}{n} \qquad \text{with } n = 1, 2, 3... \tag{2.60}$$

The frequency is thus equal to:

$$f_n = \frac{v}{\lambda} = \frac{v}{2L}n \tag{2.61}$$

where v is propagation speed inside the transmission line with length L. The frequency separation between the modes is equal to:

$$df = \frac{v}{2L}. \tag{2.62}$$

The number ρ of modes with frequency comprised between f and Δf is equal to:

$$\rho = \frac{\Delta f}{df} = \Delta f \frac{2L}{v}. \tag{2.63}$$

From the energy equipartition theorem comes that, at thermal equilibrium, the mean energy $E(f)$ stored inside the harmonic oscillator's mode with frequency f is equal to:

$$E(f) = \frac{hf}{e^{\frac{hf}{kT}} - 1} \approx kT \quad \text{for} \quad hf < kT, \tag{2.64}$$

where h is the Planck constant. The constraint $hf < kT$ is valid for all the frequencies of interest for electronic circuits. The energy $E_{\Delta f}$ stored inside all the modes within a certain range of frequencies Δf is equal to:

$$E_{\Delta f} = \Delta f \frac{2L}{v} kT. \tag{2.65}$$

Now let's imagine to open the switch, so that the resistance is again connected to the transmission line. It is straightforward to notice that the system was and is still in thermodynamic equilibrium. Every stationary wave is composed by the sum of two identical waves running in opposite directions. Let's identify with "progressive" the wave moving towards the resistance and "regressive" the one running in the opposite direction. Since the characteristic impedance of the transmission line is equal to the resistance value, the progressive wave is reflected no more and is completely absorbed by the resistance. The thermodynamic equilibrium implies that the resistor gives as much energy to the transmission line as much it receives. This means that the resistance is generating a noise waveform running inside the transmission line equal to the one running from the transmission line into the resistance. Let us consider for a while only a defined set of frequencies inside the range Δf. During the time needed by the wave to run back and forth across the transmission line, the resistor receives from all the waveforms included in the range Δf an amount of energy equal to $E_{\Delta f}$. The standing wave can

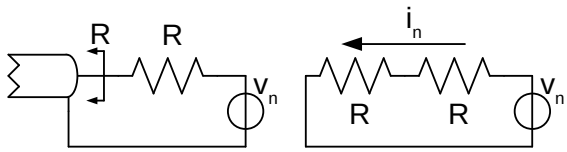

Figure 2.9: Simple schematic view representing the entities of equation 2.67.

be considered completely absorbed inside the resistor when both its progressive and regressive components reach the resistance. The time required by this process is equal to $\frac{2L}{v}$. The power P absorbed during this period is equal to:

$$P = \frac{E_{\Delta f}}{2L/v} = \frac{\Delta f \frac{2L}{v} kT}{\frac{2L}{v}} = \Delta f kT. \tag{2.66}$$

The same power must be released by the resistance to the transmission line. We know that the impedance seen from the resistance looking inside the transmission line is equal to R (figure 2.9). $\overline{v_n^2}$ is the voltage noise generator associated to the resistance R. From simple considerations about the current that flows from the resistor into the transmission line, the power P_r produced by the noise generator is equal to:

$$P_r = \overline{i_n^2} R = \overline{\left(\frac{v_n}{2R}\right)^2} R = \frac{\overline{v_n^2}}{4R}. \tag{2.67}$$

With $\overline{v_n^2}$ we mean the quadratic mean value of the noise voltage fluctuation in the frequency band Δf. If S_n is the spectral power density of the noise generator then $\overline{v_n^2} = S_n \Delta f$. Equating 2.66 and 2.67 we obtain 2.68.

$$\Delta f kT = \frac{S_n \Delta f}{4R} \qquad \text{then} \qquad S_n = 4kTR \tag{2.68}$$

If we don't simplify equation 2.64 the only difference in the final result is that the expression of the spectral power density in 2.68 becomes

$$S_n = \frac{4hf}{e^{\frac{hf}{kT}} - 1} R \tag{2.69}$$

which is almost a white distribution with a cutoff frequency at $\frac{kT}{h}$, that is however a frequency higher than the bandwidth of real electronic circuits.

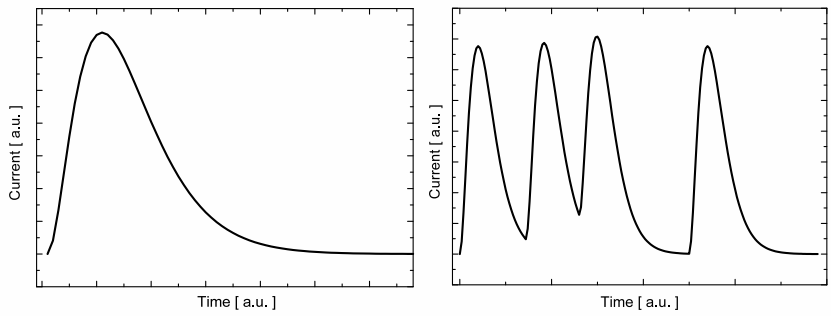

Figure 2.10: On the left, current pulse produced by a single electron passing through the barrier. On the right, the noisy current produced by the sum of several charge carriers passing the barrier at random times. This graphs are just conceptual and do not represent any real mathematical functions or physical measurements.

"Shot" or "Granular" noise

The "shot" or "granular" noise is produced by a current flowing through a potential barrier. This is what happens, for example, in diodes and bipolar transistors. The main cause is that the flux is not a continuum but is produced by the sum of the contributes of each single charge carrier. These pass across the barrier at random times and thus the overall current is not uniform but "noisy", as can be seen in figure 2.10. The statistic distribution that rules such events is the Poissonian one. We define ν as the average rate of emission and νdt the probability of emission within a time interval dt. Each charge carrier produces a current signal with duration equal to the time needed to pass across the barrier. We define $qg(t)$ as the function that describes the current produced by an electron passing through the barrier. It is the product of the electron's charge q and the unitary function $g(t)$. Obviously $\int_0^\infty g(t)\,dt = 1$. If we integrate in time the product of the current expression of a single electron passing through the barrier and the average rate of emission we obtain the total average current $\overline{i(t)}$ flowing through the barrier.

$$\overline{i(t)} = \int_0^\infty qg(\xi)\,\nu d\xi = q\nu \int_0^\infty g(\xi)\,d\xi = q\nu = I \tag{2.70}$$

In order to evaluate the mean square value of the current $\overline{i^2(t)}$ we have to sum two terms. The first one takes into account just the probability of emission of a single electron while the other represents the signal fluctuations due to correlations between signals of

different electrons.

$$\begin{aligned}\overline{i^2(t)} &= q^2\int_0^\infty g^2(\alpha)\nu d\alpha + q^2\int_0^\infty\int_0^\infty g(\alpha)\nu d\alpha\, g(\beta)\nu d\beta \\ &= q^2\nu\int_0^\infty g^2(t)dt + q^2\int_0^\infty g(\alpha)\nu d\alpha\int_0^\infty g(\beta)\nu d\beta \\ &= q^2\nu\int_0^\infty g^2(t)dt + q^2\left[\int_0^\infty g(t)\nu dt\right]^2 \\ &= q^2\nu\int_0^\infty g^2(t)dt + q^2\nu^2 \end{aligned} \tag{2.71}$$

So from equation 2.71 we obtain that

$$\sigma^2 = \overline{i^2\,(t)} - \overline{i\,(t)}^2 = q^2\nu\int_0^\infty g^2\,(t)\,dt + \cancel{q^2\nu^2} - \cancel{(q\nu)^2} \tag{2.72}$$

$$= q^2\nu\int_0^\infty |\tilde{G}\,(\omega)|^2\frac{d\omega}{2\pi} \tag{2.73}$$

The result in equation 2.72 is possible due to the Parseval's theorem. In the end we obtain:

$$S_n\,(\omega) = q^2\nu\cdot|\tilde{G}\,(\omega)|^2 = qI\cdot|\tilde{G}\,(\omega)|^2 \tag{2.74}$$

If the time needed by the electron to pass through the barrier was 0, it would produce a delta-like current signal. This means that the spectral power density S_n would be completely white. In fact if $g(t) \to \delta(t)$ then $\tilde{G}\,(\omega) \to 1$ and $|\tilde{G}\,(\omega)|^2 \to 1$. If we approximate $g(t)$ to a delta-like function, then

$$S_n \approx qI. \tag{2.75}$$

This approximation is valid only for frequencies lower than the inverse of the barrier crossing time. The shot noise is thus bandwidth limited but the cutoff is placed at so high frequencies that is of no interest for bandwidth limited electronic circuits. Generally we prefer to express spectral noise densities with the physical formalism and not with the mathematical one. For this reason we multiply the result of equation 2.75 by a factor 2. In this way we can obtain the noise power just integrating on the positive axis of the frequencies and not in the negative one. So 2.75 becomes:

$$S_n \approx 2qI. \tag{2.76}$$

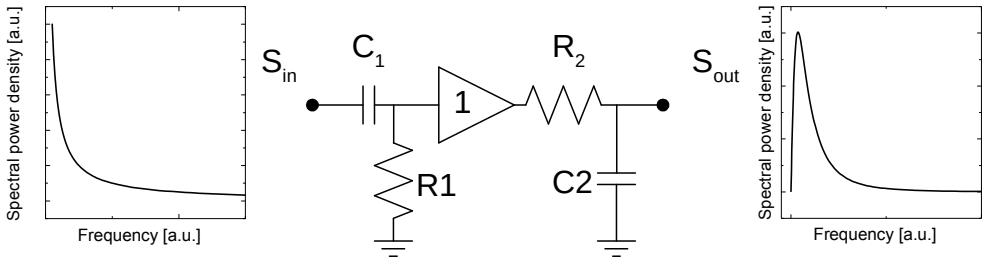

Figure 2.11: Conceptual schematic of a simple circuit bandwidth-limited both at low and high frequencies. The graph on the left shows the non convergent power spectrum of the $1/f$ noise at the input of the circuit. The graph on the right shows an integrable and convergent power spectrum of the noise filtered by the circuit.

"1/f" or "Flicker" noise

This kind of noise has a frequency spectrum such that the power spectral density is inversely proportional to the frequency. Its origin can be traced back to quasi-equilibrium phenomena in condensed matter. The analytical demonstrations generally take as a basis fundamental cosmological principles. It is also connected to trap-detrap phenomena of charge carriers inside semiconductors. Some resistances, such as the carbon ones, show this kind of noise more than others. From a purely mathematical point of view it's impossible to integrate the "$1/f$" noise down to the 0 frequency because it diverges. This doesn't happen in nature because every physical phenomena is limited in time and this determines the lower frequency limit of integration. The physical power spectrum of this kind of noise is:

$$S_{1/f} = \frac{A_f}{f} \tag{2.77}$$

where A_f is simply a coefficient. Strictly speaking $\int_0^\infty S_{1/f}\,df \to \infty$ but it's easy to demonstrate that the $1/f$ noise can converge easily at the output of an electronic circuit. Let's consider the simple circuit in figure 2.11. If the spectral power density of the input signal is $\frac{A_f}{f}$, at the output of the circuit we find that

$$S_{out} = \frac{A_f}{f} \cdot \frac{\omega^2\tau^2}{1+\omega^2\tau^2} \cdot \frac{1}{1+\omega^2\tau^2} = A_f \frac{4\pi^2\tau^2 f}{(1+4\pi^2\tau^2 f^2)^2} \tag{2.78}$$

$$\begin{cases} S_{out} \to 0 \text{ if } f \to 0 \\ S_{out} \propto \dfrac{1}{f^3} \text{ if } f \to \infty \end{cases} \qquad \text{and} \qquad \sigma^2 = \overline{v_{out}^2} = \int_0^\infty S_{out}\, df \text{ converges.} \tag{2.79}$$

The $1/f$ noise is often neglected in a first-approximation analysis. However designing a charge-sensitive preamplifier for nuclear spectroscopy is mandatory to take into account this kind of noise due to its effects on the energy resolution. We will discuss about this topic in the proper section.

Lorentzian noise

In real imperfect semiconductors there are space-localized sites where free-running charge carriers can be momentarily trapped. These sites are energetically placed in the middle of the bang-gap. These sites are generated from the imperfections naturally present in the lattice structure. Let us define τ_T as the average capture time and τ_R the average release time. The spectral power density S_n of the noise generated by a trap depends from a characteristic time τ which is the harmonic average of τ_T and τ_R.

$$S_n = \alpha \frac{1}{1+\omega^2\tau_{eq}^2} \qquad \text{with} \qquad \tau_{eq} = \frac{\tau_T \cdot \tau_R}{\tau_T + \tau_R} \tag{2.80}$$

Let us now demonstrate the analytical expression of the spectral power density formula. If a charge carrier moving around in the conduction band of a semiconductor falls into a localized trap it is no longer available for current transport. The function that represents the number of available charge carriers has the form of a Random Telegraph Signal (RTS, figure 2.12). The probability of observing m telegraphic signals in the time interval T is given by:

$$p(m,T) = \frac{(\nu T)^m}{m!}\, e^{-\nu T} \tag{2.81}$$

where ν is the mean rate of transitions per second. If τ_+ and τ_- are the average durations of the "1" and "0" states, the probability distribution of τ_+ and τ_- is:

$$p(t_\pm) = \tau_\pm^{-1}\, e^{-\frac{t_\pm}{\tau_\pm}} \tag{2.82}$$

Let us call $x(t)$ the function that describes a RTS fluctuating between the values a and $-a$. The product $x(t)x(t+\tau)$ is equal to $+a^2$ if an even of transitions occur in the interval $(t, t+\tau)$. On the other hand it is equal to $-a^2$ if in the same time period an odd number

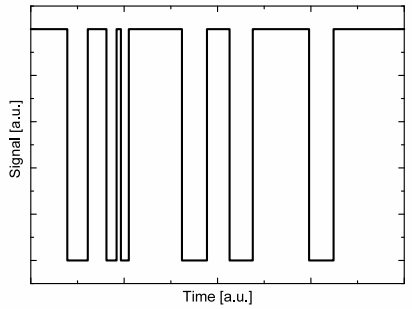

Figure 2.12: Computer simulation of a random telegraph signal produced by a carrier trap.

of transitions occur. We can thus compute the autocorrelation function $\phi_x(\tau)$

$$\begin{aligned}\phi_x(\tau) &= a^2\left[p(0,\tau)+p(2,\tau)+...\right]-a^2\left[p(1,\tau)+p(3,\tau)+...\right]\\ &= a^2e^{-\nu\tau}\left[1-\nu\tau+\frac{(\nu\tau)^2}{2!}-\frac{(\nu\tau)^3}{3!}+...\right]\\ &= a^2e^{-2\nu\tau}\end{aligned} \tag{2.83}$$

where $p(\beta,\tau)$ is the probability of having β transitions in the period τ. We can now calculate the spectral power density of noise thanks to the Wiener-Khintchine theorem.

$$\begin{aligned}S_x(\omega) &= 4\int_0^\infty \phi_x(\tau)\cos(\omega\tau)\,d\tau\\ &= \frac{2a^2/\nu}{(1+\omega^2/4\nu^2)}\\ &= 4a^2\tau_{eq}\cdot\frac{1}{\left(1+\omega^2\tau_{eq}^2\right)}\end{aligned} \tag{2.84}$$

From "Lorentzian" noise to "1/f"

The $1/f$ noise in semiconductors is a topic of great interest. The origin of such noise is related to a number of different physical processes. Here we describe how to connect such kind of noise to the mentioned Lorentzian one [16]. We have calculated in equation 2.84 the spectral power distribution of the signal produced by a single trap. Let's now consider the overall noise produced in a MOS transistor by the trapping of the charge carriers inside the oxide. Let us suppose that the trapping occurs by means of tunnel

effect from the conducting layer towards the insulating one. If the trap is located at depth w inside the oxide, its time constant τ_{eq} is equal to:

$$\tau_{eq} = \tau_0 e^{\gamma w} \tag{2.85}$$

where τ_0 and γ are constants. The traps are distributed uniformly between the depths w_1 and w_2: the corresponding characteristic times are τ_1 and τ_2. If we write the distribution of the traps depending on their corresponding characteristic time we obtain:

$$p(\tau_{eq})\,d\tau_{eq} = \begin{cases} \dfrac{d\tau_{eq}/\tau_{eq}}{\ln(\tau_2/\tau_1)}, & (\tau_1 \leqslant \tau_{eq} \leqslant \tau_2) \\ 0, & \text{Otherwise} \end{cases} . \tag{2.86}$$

From the definition of probability we have that $\int_0^\infty p(\tau)\,d\tau = 1$. Considering equations 2.83 and 2.86 we can write the spectral power density of the total carrier number fluctuation $S_n(\omega)$.

$$\begin{aligned} S_n(\omega) &= 4\phi_x(\tau)\big|_{\tau=0} \int_0^\infty \frac{\tau_{eq} p(\tau_{eq})}{(1+\omega^2\tau_{eq}^2)} d\tau_{eq} \\ &= \frac{4\phi_x(\tau)\big|_{\tau=0}}{\ln(\tau_2/\tau_1)} \int_{\tau_1}^{\tau 2} \frac{1}{(1+\omega^2\tau_{eq}^2)} d\tau_{eq} \\ &= \frac{4\phi_x(\tau)\big|_{\tau=0}}{\ln(\tau_2/\tau_1)} \cdot \frac{\tan^{-1}(\omega\tau_2) - \tan^{-1}(\omega\tau_1)}{\omega} \end{aligned} \tag{2.87}$$

Equation 2.87 shows a $1/f$ power law in the frequency range of $\omega\tau_2 \gg 1$ and $0 \leqslant \omega\tau_1 \ll 1$. This concludes the demonstration.

"K-T-C" noise

This kind of noise is also called "sampling noise" and refers to the randomness of the voltage signal sampled on a capacitor. The physical source of this noise is the "Johnson" noise coming from the series resistance of the switch used to sample. It's interesting to notice that in the final expression of the noise power the value of the resistance is dropped. To understand this phenomenon let us study the simple circuit in figure 2.13. The voltage noise generator at the input has a spectral power density of $4kTR$. The spectral power density at the output of the circuit is:

$$S_{out}(s) = 4kTR \cdot \left| \frac{1}{(1+sRC)} \right|^2 \quad \text{where} \quad s = i\omega. \tag{2.88}$$

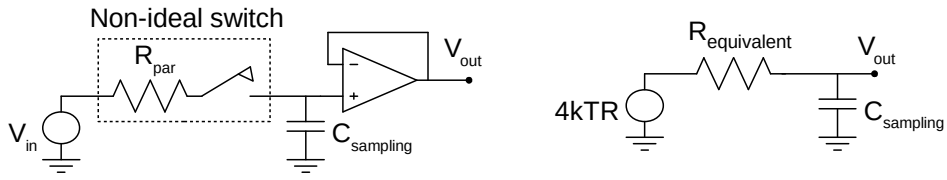

Figure 2.13: On the left: conceptual schematic of a sample-and-hold circuit. On the right: the equivalent RC circuit. The input voltage signal is neglected here. The switch is substituted by a resistance with value variable between $R_{closed} \to 0$ and $R_{open} \to \infty$. The spectral power density of the Johnson noise generator varies according to the value of the equivalent resistor.

If we calculate the variance σ^2_{out} of the output voltage we obtain:

$$\begin{aligned}\sigma^2_{out} &= 4kTR\int_0^\infty \frac{1}{1+4\pi^2f^2R^2C^2}\,df = \frac{4kTR}{2\pi RC}\left[\arctan\left(2\pi fRC\right)\right]_0^\infty \\ &= \frac{4kTR}{2\pi RC}\cdot\frac{\pi}{2} = \frac{kT}{C}.\end{aligned} \tag{2.89}$$

This result means that the variance of the sampled signal does not depend on the resistance value but only on the temperature and the capacitance. As can be seen in figure 2.14 the spectral noise density depends on the value of R: what is constant is just the value of the integral in equation 2.89. If the resistor is small (switch closed) the value $4kTR$ is small but the cutoff frequency $1/2\pi RC$ is high. We can imagine the opening of the switch as a more-or-less continuous variation of R from ≈ 0 to a really high value (almost infinite). In this case the amplitude of the $4kTR$ goes to infinity but the cutoff frequency becomes very small. The spectral power noise distribution on the output progressively reduce its bandwidth and enhances its amplitude. At the limit of $R \to \infty$ the sampling has been performed and the whole spectral power noise is packed inside a Dirac delta placed at 0 frequency. This means that performing a series of sampling processes of the same voltage reference will produce a set of data with a statistical distribution around the mean value with variance equal to σ^2_{out} of equation 2.89.

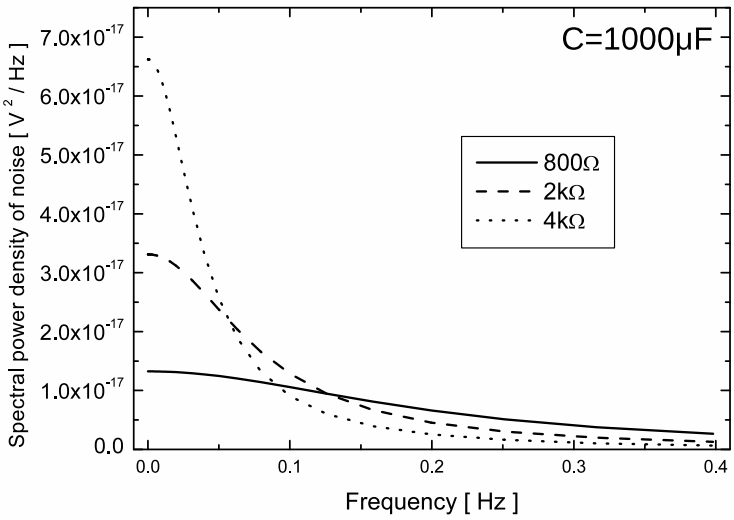

Figure 2.14: Noise spectral density at the output of a R-C circuit for different values of the resistor. As the resistance becomes higher the spectrum becomes concentrated on low frequencies. At the limit of infinite frequency (voltage sampled on a capacitor) the noise power spectral density becomes a Dirac delta centred on 0 frequency. The most important thing to notice is that, given a condenser value, the area of the function (that is the variance of the noise waveform) is constant and does not depend on the resistor value.

2.2.4 Noise sources and propagation in a charge-sensitive preamplifier

Let's now concentrate on the propagation of the noise in the circuit. The most relevant noise sources are the ones depicted in figure 2.15.

- i^2_{shot}, which represents the shot noise generated by the black current of the detector. In fact, being the detector a reverse-biased diode, it's absolutely natural to associate the reverse current to the noise induced by its granularity. Its spectral noise density is equal to 2qI, where q is the charge of the electron and I is the total current flowing through the junction.

- $i^2_{thermal}$, which represents the thermal noise of the feedback resistor. The spectral density of this noise is equal to 4KTR. The bigger the resistance, the lower the noise contribution. For this reason for spectroscopy applications generally a GΩ resistor is chosen.

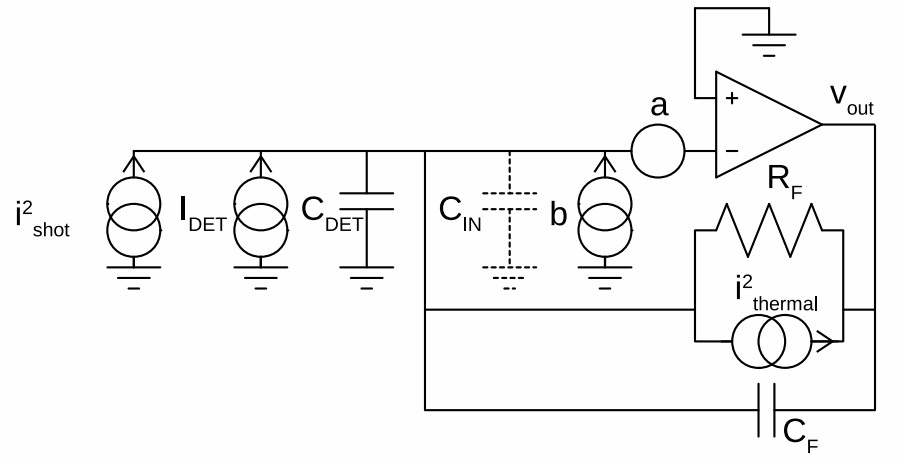

Figure 2.15: Schematic diagram of a charge-sensitive preamplifier. Some non-idealities were added, such as the noise generators and the parasitic input capacitance C_{in}

- a and b, which stand for the overall series and parallel noise generators of the preamplifier. These aren't physical sources but an input-referred model of the noise sources of the operational amplifier.

Now let's calculate the spectral noise densities of a and b. If the operational amplifier is correctly designed, the only relevant noise contribution comes from the input stage, while the ones coming from the following stages can be neglected. The reason for this comes after straightforward calculation. In fact the transfer function that connects the voltage on the gate of the input transistor $\tilde{v}_{in}$ and the one on the drain of the same transistor $\tilde{v}_{drain}$ is equal to:

$$\frac{\tilde{v}_{drain}}{\tilde{v}_{in}} = g_m \left(R_{LOAD} // R_0\right). \tag{2.90}$$

Since the output resistance R_0 of the input transistor is generally appreciably larger than R_{LOAD}, the expression $(R_{LOAD} // R_0)$ is generally omitted in favour of the simpler form R_{LOAD}. If the transconductance g_m of the input transistor is high enough, condition that depends on the physical properties of the device and the chosen bias point, the product $g_m (R_{LOAD} // R_0)$ is larger than 1. In order to refer to the input a voltage noise generator that insists on the drain of the input transistor we just have to invert the expression in equation 2.90. Since we are dealing with spectral noise densities, being these quadratic magnitudes, all the transfer functions must be taken in modulus and elevated to the

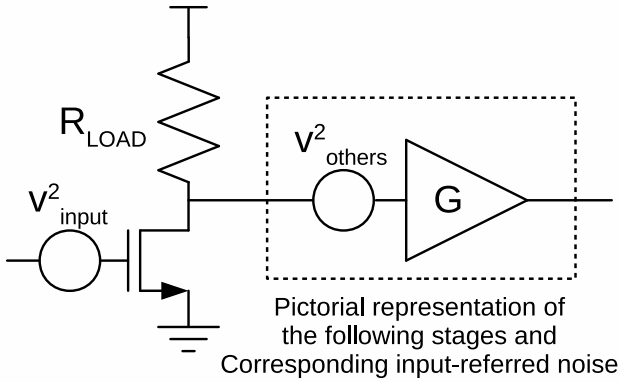

Figure 2.16: Simplified schematics of an operational amplifier. The input stage is represented with a transistor in common-source configuration and a load resistance. All the following stages are represented by a gain block with input-referred noise.

second power. The series input referred noise source corresponding to v^2_{others} of figure 2.16 is equal to:

$$\tilde{v}^2_{in\_eq} = \frac{\tilde{v}^2_{others}}{[g_m\,(R_{LOAD}\,//\,R_0)]^2}. \tag{2.91}$$

This means that if the input stage is designed properly the denominator in equation 2.91 is bigger than 1. For this reason the main contribution in the series input referred noise of a charge-sensitive preamplifier is the one produced by the input transistor. This is equal to a voltage series noise with spectral noise density of $\psi\frac{4KT}{g_m}$ where ψ is a constant usually equal to 0.7. This is the series noise generator "a" depicted in figure 2.15. If the input transistor is realized with CMOS technology then the input leakage current is absolutely negligible. If the input transistor is a JFET one there is a non completely neglegible leakage current I_L flowing from the input node into the gate of the input transistor. A shot noise equal to $2qI_L$ is associated with this current. This noise is parallel and is the b noise source of figure 2.15. This one sums up with the noise source connected to the feedback resistor. There is also another important noise source that must be taken into account during the design of an ASIC preamplifier in CMOS technology and is the $1/f$ noise source. This noise is strictly technology dependent. In a CMOS transistor its power goes as the inverse of the area of the device. It's expression is :

$$v^2_{1/f} \propto \frac{1}{W \cdot L \cdot f} \tag{2.92}$$

Generally this noise source is neglected in first-approximation calculations. We can, for simplicity, consider the feedback resistance's thermal noise source as part of the parrallel noise source of the preamplifier. So the two noise sources of the preamplifier become:

$$\begin{cases} a = \psi \dfrac{4kT}{g_m} \qquad \text{with} \qquad \psi \approx 0.7 \\ \\ b = \dfrac{4kT}{R_F} + 2qI_L. \end{cases} \tag{2.93}$$

Now that we have identified all the main noise sources, we want to compare them with the charge information coming from the detector, in order to quantify the overall equivalent noise charge at the input induced by the electronics and thus the signal to noise ratio. In order to do so we transform the voltage noise generator "a" into a current one so as to compare it directly with the current signal produced by the detector. To do so we propagate the noise to the output of the CSP and then we back-propagate it. For simplicity we define $Z_1 = \frac{1}{s(C_{DET}+C_{IN})}$ and $Z_2 = \frac{R_F}{1+sR_FC_F}$. The expression of the voltage noise at the output of the preamplifier due to the "a" noise source only is:

$$S_{out,a} = a\left|1 + \frac{Z_2}{Z_1}\right|^2 = a\left|1 + \frac{\frac{R_F}{1+sRC}}{\frac{1}{s(C_{DET}+C_{IN})}}\right|^2 \tag{2.94}$$

where, for simplicity, we defined

$$a\frac{1+\omega^2C_T^2R_F^2}{1+\omega^2\tau_F^2}C_T = C_{DET} + C_{IN} + C_F \qquad \text{and} \qquad \tau_F = C_FR_F. \tag{2.95}$$

Now let's calculate the transfer function that is used to propagate a parallel current noise source at the input to the output of the CSP. In the approximation of ideal feedback ($GH \to +\infty$) we have:

$$S_{OUT}^2 = b\left|-\frac{R_F}{1+s\tau_F}\right|^2 = b\frac{R_F^2}{1+\omega^2\tau_F^2}. \tag{2.96}$$

In order to find the expression of the equivalent parallel current noise generator at the input b_{EQ} that produces at the output the same noise of the voltage noise generator "a" we must divide the expression in equation 2.94 by the one in equation 2.96.

$$b_{EQ} = a\frac{1+\omega^2C_T^2R_F^2}{1+\omega^2\tau_F^2}\cdot\frac{1+\omega^2\tau_F^2}{R_F^2} = a\left(\omega^2C_T^2 + \frac{1}{R_F^2}\right) \tag{2.97}$$

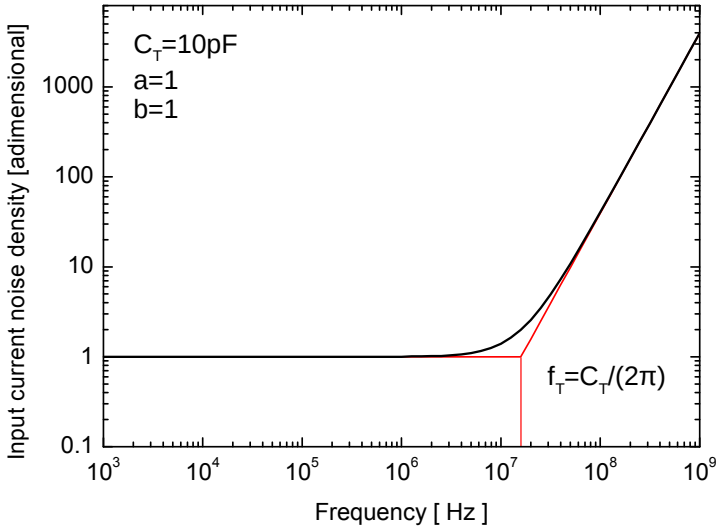

Figure 2.17: Equivalent input current noise produced by a CSP with series voltage current generator "a", parallel current noise generator "b" and total capacitance referred to the input C_T equal to 10 pF. Please notice that both "a" and "b" are unitary and adimensional.

The total noise generated by the charge-sensitive preamplifier can thus be correctly modelled with a single parallel current noise generator at the input b_{TOT} that is the sum of b and b_{EQ} (figure 2.17).

$$b_{TOT} = b + b_{EQ} = b + \frac{a}{R_F^2} + a\omega^2 C_T^2 = b + \psi\frac{4kT}{g_m R_F^2} + \psi\omega^2 C_T^2 \frac{4kT}{g_m} \tag{2.98}$$

A typical value of R_F in gamma spectroscopy is 1GΩ while g_m is generally under 10mS. This makes the second term in equation 2.98 almost negligible. The expression of b_{EQ} becomes:

$$b_{TOT} = 2qI_L + \frac{4kT}{R_F}\left(1 + \frac{\psi}{g_m R_F}\right) + \psi\frac{4kT}{g_m}\omega^2 C_T^2 = b + aC_T^2\omega^2 \tag{2.99}$$

The noise corner frequency ω_c can be easily calculated equating b and $aC_T^2\omega_c^2$.

$$b = aC_T^2\omega_c^2 \qquad \Rightarrow \qquad \omega_c = \sqrt{\frac{b}{a}} \cdot \frac{1}{C_T} \qquad \Rightarrow \qquad \tau_c = C_T\sqrt{\frac{a}{b}} \tag{2.100}$$

2.3 Some considerations about real distributed-impedance feedback resistors

As described diffusely in the previous section, the feedback resistor has the role of progressively discharge the feedback capacitor avoiding an unbearable pile-up of the signals and providing a precise DC working point to the CSP. Since the parallel current noise generated by this passive device sums up directly with the one produced by the detector, the value of the resistance must be high in order to keep the spectral power noise low. Generally for gamma spectroscopy a 1 GΩ or 2 GΩ resistor is chosen. They provide respectively a spectral power density of $1.66 \cdot 10^{-29} \frac{A^2}{Hz}$ and $8.28 \cdot 10^{-30} \frac{A^2}{Hz}$. These values are in agreement with the required spectroscopic resolutions. Traditionally these resistors are discrete thin-film type. Nowadays ASICs are progressively substituting the old discrete-type circuits due to numerous benefits in terms of readout granularity and power consumption. However the physical implementation of a feedback resistor on a standard silicon CMOS chip is absolutely non trivial. Contemporary fabrication technologies provide modules specifically designed for high-value resistance, but their planar resistivity is around $1 \frac{k\Omega}{\square}$. If the minimum width of the polysilicon resistor is 1 μm the area of the resistor (without considering the empty areas within the resistance's bends) is 1 mm^2. This means that the area occupied by the single feedback resistance can be considerably larger than a complete charge-sensitive preamplifier, feedback and Miller capacitors included. Area consumption is however not the biggest problem regarding integrated feedback resistances. Due to their huge area they suffer from a strong coupling to bulk (or to the n-wells placed under the resistors). This coupling modifies significantly not only the resistance impedance but also its physical noise source. In order to understand this concept properly we start from the analysis of a simple lumped-parameters resistance with capacitive coupling, as in the left diagram of figure 2.18.

2.3.1 Impedance of a distributed-parameter resistance with capacitive coupling

The calculation of the impedance of a resistance with distributed capacitance starts with the analysis of a simple lumped-parameters R-C cell. The circuit on the left of figure 2.18 obeys to the following relation.

$$\begin{bmatrix} V_0 \\ V_1 \end{bmatrix} = \begin{bmatrix} R + \frac{1}{sC} & -\frac{1}{sC} \\ \frac{1}{sC} & -\frac{1}{sC} \end{bmatrix} \cdot \begin{bmatrix} I_0 \\ I_1 \end{bmatrix} \tag{2.101}$$

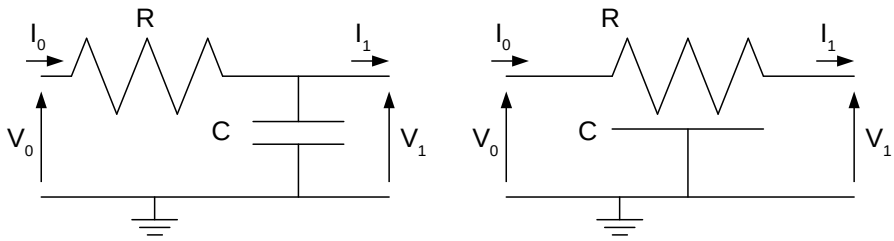

Figure 2.18: Left: simple lumped-parameter resistance with capacitive coupling to bulk which is shorted to ground. Right: distributed-parameter resistance of value R with total capacitive coupling C.

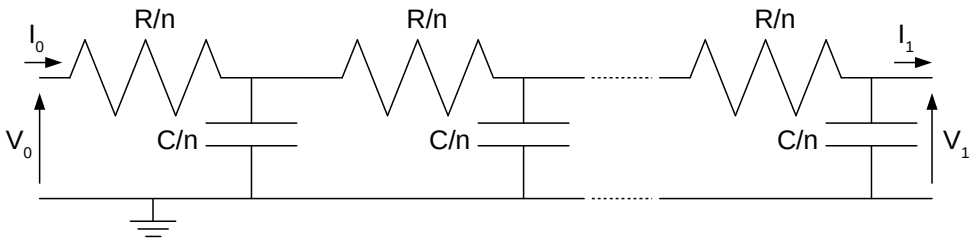

Figure 2.19: First-order approximation of a distributed resistance R with capactive coupling C made of a series of n R-C cells with resistance $\frac{R}{N}$ and capacitance $\frac{C}{N}$.

Even if 2.102 is absolutely correct, we are going to use a different formalism since it's more practical in our problem.

$$\begin{bmatrix} V_0 \\ I_0 \end{bmatrix} = \begin{bmatrix} 1+sRC & R \\ sC & 1 \end{bmatrix} \cdot \begin{bmatrix} V_1 \\ I_1 \end{bmatrix} \tag{2.102}$$

This expression is really handy when we want to write the relations between voltages and currents for a double bipole made of a series of R-C circuits. In fact the simplest way to approximate a distributed-parameter resistance with capacitive coupling is to divide the total resistance and capacitance in n segments and to connect the output of each to the input of the next one like in figure 2.19. The equation that represents the behaviour of the circuit can be obtained starting from equation 2.102.

$$\begin{bmatrix} V_0 \\ I_0 \end{bmatrix} = \begin{bmatrix} 1+s\frac{RC}{n} & \frac{R}{n} \\ \frac{sC}{n} & 1 \end{bmatrix}^n \cdot \begin{bmatrix} V_1 \\ I_1 \end{bmatrix} \tag{2.103}$$

The direction of the output current of an R-C cell I_1 is such that its sign is the same of the input current I_0 of the next R-C cell. Obviously the output voltage V_1 of the preceding cell is equal to the input voltage V_0 of the following cell. Now let us diagonalize the matrix in equation 2.103. To do so we must evaluate the eigenvalues $\lambda_{1,2}$ and eigenvectors $v_{1,2}$.

$$\begin{bmatrix} V_0 \\ I_0 \end{bmatrix} = \begin{bmatrix} B \end{bmatrix} \cdot \begin{bmatrix} \lambda_1^n & 0 \\ 0 & \lambda_2^n \end{bmatrix} \cdot \begin{bmatrix} B^{-1} \end{bmatrix} \cdot \begin{bmatrix} V_1 \\ I_1 \end{bmatrix} \tag{2.104}$$

The matrix B can be calculated from the expression of the eigenvectors while B^{-1} is obtained inverting B.

$$\lambda_{1,2} = \frac{\mp\sqrt{sRC\,(sRC + 4n^2)} + sRC + 2n^2}{2n^2} \tag{2.105}$$

$$v_{1,2} = \begin{bmatrix} -\dfrac{R\sqrt{sC} \pm \sqrt{R\,(4n^2 + sRC)}}{2n\sqrt{sC}} \\ \\ 1 \end{bmatrix} \tag{2.106}$$

$$B = \begin{bmatrix} -\dfrac{R\sqrt{sC} + \sqrt{R\,(4n^2 + sRC)}}{2n\sqrt{sC}} & -\dfrac{R\sqrt{sC} - \sqrt{R\,(4n^2 + sRC)}}{2n\sqrt{sC}} \\ \\ 1 & 1 \end{bmatrix} \tag{2.107}$$

$$B^{-1} = \begin{bmatrix} -\dfrac{n\sqrt{sC}}{\sqrt{R\,(4n^2 + sRC)}} & \dfrac{R\sqrt{sC + \sqrt{R\,(4n^2 + sRC)}}}{2\sqrt{R\,(4n^2 + sRC)}} \\ \\ \dfrac{n\sqrt{sC}}{\sqrt{R\,(4n^2 + sRC)}} & -\dfrac{R\sqrt{sC - \sqrt{R\,(4n^2 + sRC)}}}{2\sqrt{R\,(4n^2 + sRC)}} \end{bmatrix} \tag{2.108}$$

The higher the number n of R-C cells, the better the approximation of the resistance R with distributed capacitance C. We thus evaluate for $n \to \infty$ the expressions of the eigenvalues matrix, B and B^{-1} separately. Their analytical expressions converge and thus we can re-write equation 2.104 in the limit for $n \to \infty$.

$$\begin{bmatrix} V_0 \\ I_0 \end{bmatrix} = \begin{bmatrix} -\sqrt{\dfrac{R}{sC}} & \sqrt{\dfrac{R}{sC}} \\ \\ 1 & 1 \end{bmatrix} \cdot \begin{bmatrix} e^{-\sqrt{sRC}} & 0 \\ \\ 0 & e^{\sqrt{sRC}} \end{bmatrix} \cdot \begin{bmatrix} -\dfrac{\sqrt{sC}}{2\sqrt{R}} & \dfrac{1}{2} \\ \\ \dfrac{\sqrt{sC}}{2\sqrt{R}} & \dfrac{1}{2} \end{bmatrix} \cdot \begin{bmatrix} V_1 \\ I_1 \end{bmatrix} \tag{2.109}$$

Multiplying the second and third matrix we obtain the following equation.

$$\begin{bmatrix} V_0 \\ I_0 \end{bmatrix} = \begin{bmatrix} -\sqrt{\frac{R}{sC}} & \sqrt{\frac{R}{sC}} \\ 1 & 1 \end{bmatrix} \cdot \begin{bmatrix} -\frac{\sqrt{sC}}{2\sqrt{R}} e^{-\sqrt{sRC}} & \frac{e^{-\sqrt{sRC}}}{2} \\ \frac{\sqrt{sC}}{2\sqrt{R}} e^{\sqrt{sRC}} & \frac{e^{\sqrt{sRC}}}{2} \end{bmatrix} \cdot \begin{bmatrix} V_1 \\ I_1 \end{bmatrix} \tag{2.110}$$

The final result comes after the multiplication of the two so-obtained matrices.

$$\begin{bmatrix} V_0 \\ I_0 \end{bmatrix} = \begin{bmatrix} \cosh\left(\sqrt{sRC}\right) & \sqrt{\frac{R}{sC}} \sinh\left(\sqrt{sRC}\right) \\ \sqrt{\frac{sC}{R}} \sinh\left(\sqrt{sRC}\right) & \cosh\left(\sqrt{sRC}\right) \end{bmatrix} \cdot \begin{bmatrix} V_1 \\ I_1 \end{bmatrix} \tag{2.111}$$

Equation 2.111 contains implicitly the expression of the impedance of the resistance with distributed capacitance. The impedance matrix can be obtained rearranging the terms so as to obtain a voltage-only vector on the left and a current-only vector on the right. It is straightforward to see that, for $s \to 0$ equation 2.111 assumes the trivial expression in equation 2.112

$$\begin{bmatrix} V_0 \\ I_0 \end{bmatrix} = \begin{bmatrix} 1 & R \\ 0 & 1 \end{bmatrix} \cdot \begin{bmatrix} V_1 \\ I_1 \end{bmatrix} \tag{2.112}$$

This ensures that such physical resistance behaves for DC currents exactly as a ideal one and somehow confirms that the adopted procedure is correct. Now that we have found a valid method to describe the impedance of a distributed-parameter resistance starting from a multiple-cell approximation, we must find out if the same procedure gives some results if used to calculate the noise generated by this kind of device.

2.3.2 Noise produced by a distributed-parameter resistance with capacitive coupling

We thus adopt the same approach to evaluate the spectral noise density produced by a resistor with distributed capacitance. The first step is to subdivide the resistance into n cells. Each cell is made of a resistance $\frac{R}{n}$ and a capacitor $\frac{C}{n}$. To each resistance is associated a voltage noise generator v_n with spectral power density of the noise $4kT\frac{R}{n}$ (figure 2.20). The spectral density of rms voltage fluctuation associated to such noise generator is $2\sqrt{kT\frac{R}{n}}$. The formalism used in the previous subsection is not adequate to describe the effects of the noise generators in the circuit. In the previous case the output

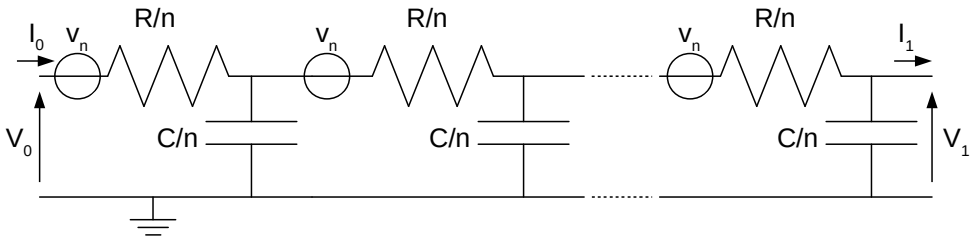

Figure 2.20: Resistance with distributed capacitance modelled with a series of n R-C cells. Each one is made of a resistance $\frac{R}{n}$ and a capacitance $\frac{C}{n}$. To each resistance a voltage noise generator v_n is associated with spectral power density $4kT\frac{R}{n}$.

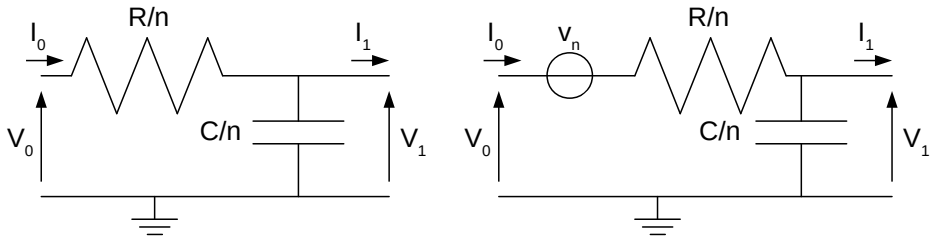

Figure 2.21: Left: R-C cell without noise generator. The values of resistance and capacitance are, as usually, $\frac{R}{n}$ and $\frac{C}{n}$. Right: R-C cell with voltage noise generator associated to $\frac{R}{n}$. In a 3-dimensional affine space these two systems are described by equations 2.113 and 2.114.

voltage of the previous cell was equal to the input voltage of the next one. In this case the input voltage of the following cell is equal to the sum of the output voltage of the previous cell and the rms voltage fluctuation introduced by the noise generator. We can easily obtain this result if we move the matrix formalism of the previous subsection to an affine space. This means that we will implement a 3-dimensional vector form even if it would naturally be 2-dimensional. The equation that describe the behaviour of a simple R-C cell without noise generator, like the left one in figure 2.21, is:

$$\begin{bmatrix} V_0 \\ I_0 \\ 1 \end{bmatrix} = \begin{bmatrix} 1+\frac{sRC}{n^2} & \frac{R}{n} & 0 \\ \frac{sC}{n} & 1 & 0 \\ 0 & 0 & 1 \end{bmatrix} \cdot \begin{bmatrix} V_1 \\ I_1 \\ 1 \end{bmatrix}. \tag{2.113}$$

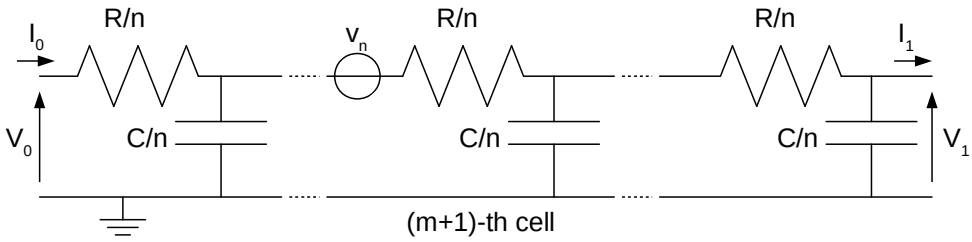

Figure 2.22: Resistance with distributed capacitance modeled with n R-C cells of which only the (m+1)-th is noisy. The relations between voltages and currents at the terminals are written in equation 2.115

If we want to add the voltage noise generator we just have to add a term in the matrix of equation 2.113, obtaining equation 2.114.

$$\begin{bmatrix} V_0 \\ I_0 \\ 1 \end{bmatrix} = \begin{bmatrix} 1+\frac{sRC}{n^2} & \frac{R}{n} & 2\sqrt{\frac{kRT}{n}} \\ \frac{sC}{n} & 1 & 0 \\ 0 & 0 & 1 \end{bmatrix} \cdot \begin{bmatrix} V_1 \\ I_1 \\ 1 \end{bmatrix}. \tag{2.114}$$

In order to evaluate the noise produced by the resistance with distributed capacitance we must follow this procedure. First of all we subdivide the resistor in n simple R-C cells. Then we evaluate the noise produced by the whole device if only the (m+1)-th cell is noisy. We finally sum up the contributes of every single cell and we evaluate the result for the number of cells that goes to infinity. This procedure is possible because the noise generators are completely uncorrelated and thus they sum up quadratically. Let us evaluate the noise induced at the terminals of the whole resistance by the noisy (m+1)-th cell. This means that we connect together n-m-1 noiseless cells, a noisy cell and, finally, m noiseless cells. This can be seen in figure 2.22.

$$\begin{bmatrix} V_0 \\ I_0 \\ 1 \end{bmatrix} = \begin{bmatrix} 1+\frac{sRC}{n^2} & \frac{R}{n} & 0 \\ \frac{sC}{n} & 1 & 0 \\ 0 & 0 & 1 \end{bmatrix}^{n-m-1} \begin{bmatrix} 1+\frac{sRC}{n^2} & \frac{R}{n} & 2\sqrt{\frac{kRT}{n}} \\ \frac{sC}{n} & 1 & 0 \\ 0 & 0 & 1 \end{bmatrix} \begin{bmatrix} 1+\frac{sRC}{n^2} & \frac{R}{n} & 0 \\ \frac{sC}{n} & 1 & 0 \\ 0 & 0 & 1 \end{bmatrix}^{m} \begin{bmatrix} V_1 \\ I_1 \\ 1 \end{bmatrix} \tag{2.115}$$

Solving equation 2.115 leads to the following expression:

$$\begin{bmatrix} V_0 \\ I_0 \\ 1 \end{bmatrix} = \left[M_{m,n} \right] \cdot \begin{bmatrix} V_1 \\ I_1 \\ 1 \end{bmatrix} \tag{2.116}$$

where $M_{m,n}$ is a bidimensional matrix equal to the expression 2.117. The matrices 2.113 and 2.114 were diagonalized in order to solve easily the exponentiation. The matrix B is made of the eigenvectors of the matrix in equation 2.113 while B^{-1} is its inverse. The eigenvalues are λ_1 and λ_2.

$$M_{m,n} = \left[B \right] \cdot \begin{bmatrix} \lambda_1^{n-m-1} & 0 & 0 \\ 0 & \lambda_2^{n-m-1} & 0 \\ 0 & 0 & 1 \end{bmatrix} \cdot \left[B^{-1} \right] \cdot \begin{bmatrix} 1 + \frac{sRC}{n^2} & \frac{R}{n} & 2\sqrt{\frac{kRT}{n}} \\ \frac{sC}{n} & 1 & 0 \\ 0 & 0 & 1 \end{bmatrix} \cdot$$

$$\cdot \left[B \right] \cdot \begin{bmatrix} \lambda_1^m & 0 & 0 \\ 0 & \lambda_2^m & 0 \\ 0 & 0 & 1 \end{bmatrix} \cdot \left[B^{-1} \right] \tag{2.117}$$

Now it's time to reflect on the application of the resistance with distributed capacitance. In fact we want to use it as a feedback resistor for an integrated CSP. One terminal is connected to the input of the preamplifier which is virtual ground. The other is connected to the low-impedance output of the CSP. This means that, for the noise analysis of the circuit, both the terminals are shorted to ground. Also the bulk is connected to ground at both sides. With this approximation we want to evaluate the spectral power density of the current noise produced by the resistance and referred to the input. Such noise generator will substitute the simpler expression of $i^2_{thermal}$. Since both V_0 and V_1 are known variables, we want to calculate only I_0 and I_1. To do so we rewrite equation 2.116 in order to obtain 2.118.

$$\begin{bmatrix} I_1 \\ I_0 \\ 1 \end{bmatrix} = \left[M'_{m,n} \right] \cdot \begin{bmatrix} V_1 \\ V_0 \\ 1 \end{bmatrix} \tag{2.118}$$

Now we impose $V_1 = V_0 = 0$. In this way we obtain two terms, $I_{0,m,n}$ and $I_{1,m,n}$ which represent the current noise generated respectively at the left and right terminal of the

resistance by the (m+1)-th noisy cell only, if it is subdivided into n elementary R-C cells.

$$\begin{bmatrix} I_{1,m,n} \\ I_{0,m,n} \\ 1 \end{bmatrix} = \left[M'_{m,n}\right] \cdot \begin{bmatrix} 0 \\ 0 \\ 1 \end{bmatrix} \tag{2.119}$$

The total current noise i^2_{NOISE} generated at one terminal (if this one is shorted to ground) is equal to the sum of the noise coming from all the cells. This means that we must sum up all the $I_{0,m,n}$ (or $I_{1,m,n}$) with m that goes from 0 to n-1. The best model for the resistance with distributed capacitance is the one with higher n. In order to evaluate i^2_{NOISE} properly we must let n go to infinity.

$$i^2_{NOISE} = \lim_{n\to\infty} \sum_{m=0}^{n-1} |I_{0,m,n}|^2 = \lim_{n\to\infty} \sum_{m=0}^{n-1} |I_{1,m,n}|^2 \tag{2.120}$$

The current noise produced at the two terminals should be equal due to straightforward considerations about symmetry. The analytical solution of equation 2.120, expressed as a function of frequency f gives the following result.

$$i^2_{NOISE} = 4KT\sqrt{\frac{\pi Cf}{R}} \cdot \left[\frac{\sin\left(2\sqrt{\pi RCf}\right) + \sinh\left(2\sqrt{\pi RCf}\right)}{\cosh\left(2\sqrt{\pi RCf}\right) - \cos\left(2\sqrt{\pi RCf}\right)}\right] \tag{2.121}$$

Both for $f \to 0$ or $C \to 0$, that means in the limit for low frequencies (DC) or for negligible capacitive coupling ($C = 0$) the expression of the current noise density in equation 2.121 becomes the usual one from an ideal resistor.

$$\lim_{s\to 0} i^2_{NOISE} = \lim_{C\to 0} i^2_{NOISE} = \frac{4kT}{R} \tag{2.122}$$

This suggest that the model proposed is coherent with the one of a physical resistor. Let's consider a realistic example. The technology on which our ASIC preamplifier is based (AMS C35B4C3) provides a high-resistance polysilicon module. The resistances realized with this module have a minimum width of 0.8 μm. An integrated polysilicon resistor of 10 MΩ has a total parasitic coupling to bulk equal to ≈1 pF. If we connect such a resistor to the input of a charge-sensitive preamplifier, the spectral noise density it produces is equal to the one of an ideal resistor ($1.656 \cdot 10^{-27} A^2/\,Hz$) only for low frequencies, where the contribute of the capacitive coupling is negligible. For frequencies higher than some KHz the spectral noise density starts to rise. The spectral noise density for high frequencies

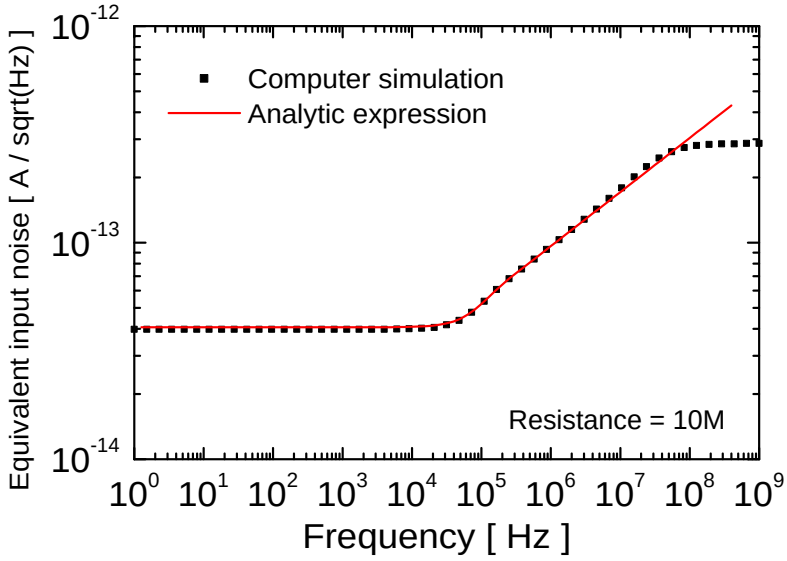

Figure 2.23: Equivalent input noise produced by an integrated 10 MΩ feedback resistance of a CSP with total parasitic capacitance to bulk equal to 1 pF. The lumped-parameter computer simulation is compared to the analytical model.

show an asymptotic behaviour like $\sqrt{f}$. In figures 2.23, 2.24 and 2.25 we compare the power density of noise calculated with our model and the one obtained from computer simulations. The resistance model used by the simulator is a lumped-parameter one made of 25 R-C cells. In the simulation results the spectral noise density shows a plateau at high frequencies. This is due to a natural limitation in a lumped-parameter model respect to a distributed one.

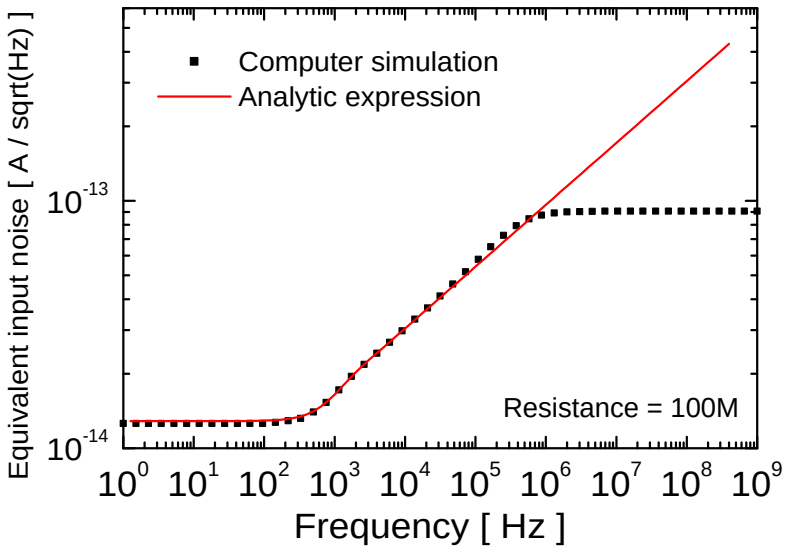

Figure 2.24: Equivalent input noise produced by an integrated 100 MΩ feedback resistance of a CSP with total parasitic capacitance to bulk equal to 10 pF. The lumped-parameter computer simulation is compared to the analytical model.

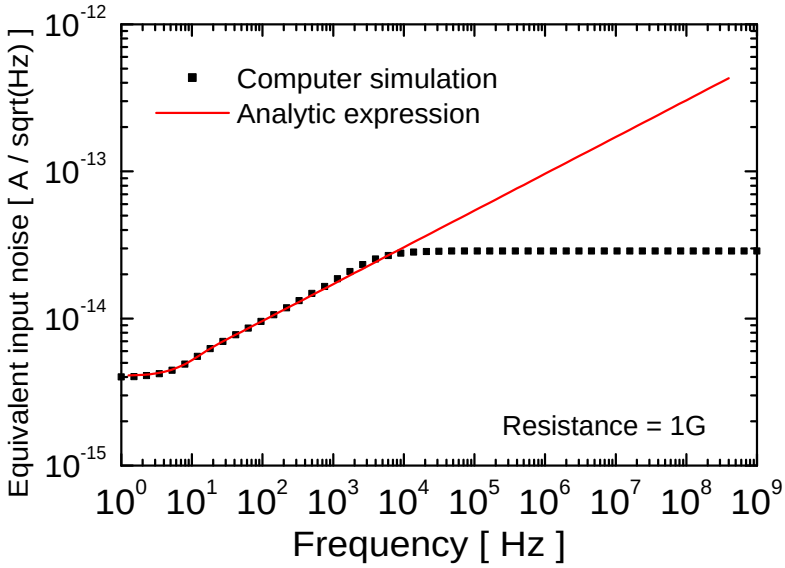

Figure 2.25: Equivalent input noise produced by an integrated 1 GΩ feedback resistance of a CSP with total parasitic capacitance to bulk equal to 100 pF. The lumped-parameter computer simulation is compared to the analytical model.

Chapter 3

Asic preamplifier

In this chapter we will present the multichannel ASIC charge-sensitive preamplifier we have designed realized and tested. It is specifically designed to be compliant with the requirements of the TRACE detector array. It is made of silicon pad detectors with 60 front pads connections and one back connection. The front pads are decoupled from the CSP input by capacitors realized directly on the detector. The back connection must be decoupled by an external capacitor. The ASIC is realized in C35B4C3 technology and occupies an area of 5 mm^2 (see figure 3.1). The ASIC is composed of four front channels and one back channel. The front channels are specifically designed to receive hole signals while the back channel is optimized for electrons. The back channel is separately powered and can be shut down if not used.

The preamplifier was designed with the following specifications in mind: low power consumption, low noise, fast risetime and wide bandwidth. The ASIC preamplifier will be put inside the reaction chamber next to the detectors and thus the heat dissipation can be a concern. A low power consumption ensures a proper operation of the devices without the need of big dissipating structures. The noise should be low in order to achieve the best resolution possible. Even if particle spectroscopy has less stringent requirements respect to gamma spectroscopy, a resolution in the order of 2% is mandatory. The collection time of the charge carriers inside the detector is in the order of few tens on ns. The analysis of the current profile of the detector signals (Pulse-Shape Analysis, or PSA) can give information about the mass and charge of the impinging particles. A risetime in the order of 10 ns is absolutely mandatory, otherwise the PSA cannot give any result. This means that the preamplifier must have a wide bandwidth and a very high slew rate. The CSP implements the fast-reset technology. In case of saturation a precise and constant

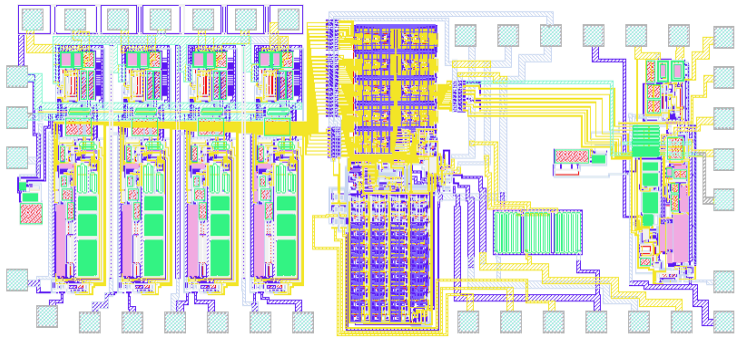

Figure 3.1: Layout of the multichannel ASIC charge-sensitive preamplifier. The dimensions are 1.5 mm and 3.3 mm. On the left we can see the four channels designed for hole signals. In the middle there is the I^2C engine and on the right the channel designed for electron signals.

current generator swiftly discharges the input node until the output baseline voltage is restored. This technique on the front channels is used just to minimize the dead-time, while on the back channel is used to extend the dynamic range by more than one order of magnitude. The preamplifier is equipped with an I^2C engine. With a simple digital stream we can choose some critical parameters of the circuit selecting from a predefined set of values. In this way we can adjust the bandwidth, the feedback capacitor and the reset speed of the preamplifier. In the following sections we will analyse in detail every single part of the circuit.

3.1 ASIC block diagram

As can be seen in figure 3.2, the ASIC is made of four front channels and one back channel, which share the same design concept but with complementary structures. The front channels must be optimized for hole signals, which generate negative signals at the output. For this reason in these channels the available output voltage swing is maximized in the negative direction. The back channel, on the other hand, is optimized for electron signals. Since to collect all the signals coming from the detector we need 60 front channels (equivalent to an array of 15 ASICs), it is obvious that not all the back channels in the ASIC array will be used. For this reason the back channel on each chip is separately powered and can be shut down if not used. In each channel the analog components that can be adjusted are the feedback capacitor, the Miller capacitor, the bias current of the input stage and the reset current. Each one of these can assume four values. Each channel

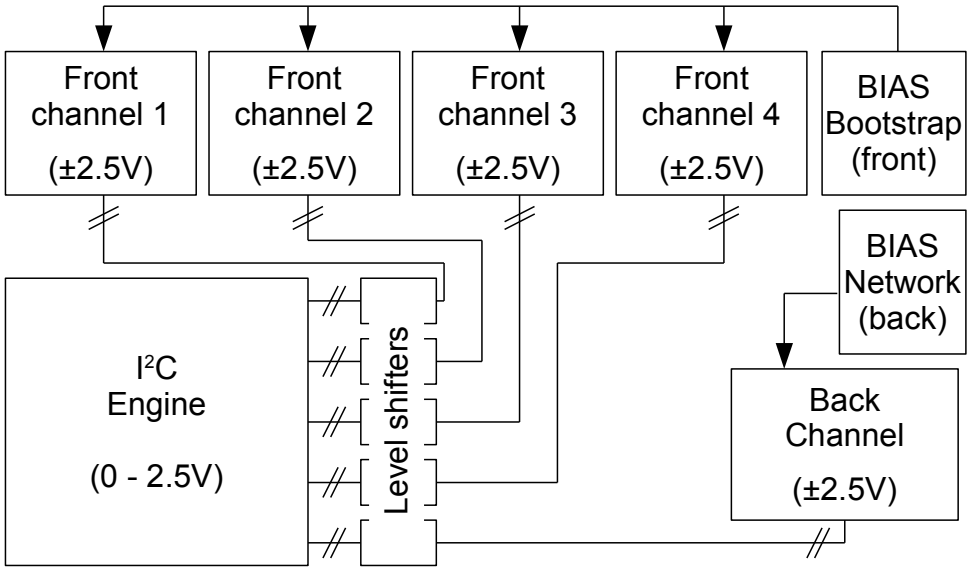

Figure 3.2: Block diagram of the ASIC. The whole chip is powered with a dual ±2.5 V power rail. The I^2C engine works between 2.5 V and ground. The adjustment of the parameters of the channels is accomplished via transmission gates. For this reason level shifters are needed to convert 0-2.5 V logic signals into ±2.5 V ones. The back channel can be shut down if not used.

thus receives eight digital controls. These ones come from the I^2C engine, but need to be converted from the 0-2.5 V level of the digital part of the ASIC to the ±2.5 V of the analog one. This is accomplished by a series of level shifters with a very simple structure, visible in figure 3.3. The 0-2.5 V signal ν_D and its negated $\bar{\nu_D}$ are used to drive a differential pair with both sources connected to the power rail that remains constant through the conversion. In our case in the conversion from 0-2.5 V to ±2.5 V the differential pair is made of pmos transistors with the sources connected to +2.5 V. The load of the differential pair is made of two transistors (nmos transistors, in our case) with the gate of the one connected to the drain of the other. The output is then sent to a simple inverter that acts as a buffer. By means of proper dimensioning, this simple circuit can act as a level shifter. Since all the digital part of the ASIC is just a slow-control system, we are not concerned about the commutation speed.

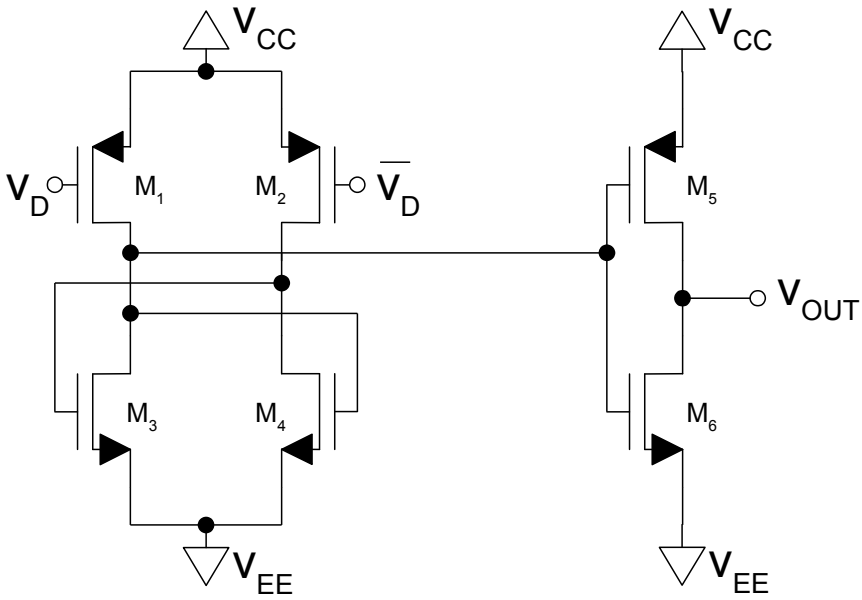

Transistor	M_1	M_2	M_3	M_4	M_5	M_6
W [µm]	10	10	5	5	10	10
L [µm]	0.5	0.5	4	4	0.5	0.5

Figure 3.3: Schematic of a single cell of the level shifter. The input signal V_D and its negated value $\bar{V_D}$ come directly from the SRAM of the I^2C engine. They both swing between 0 V and 2.5 V. The output signal V_{OUT} swings from -2.5 V to +2.5 V.

3.2 Block diagram of the fast-reset preamplifier

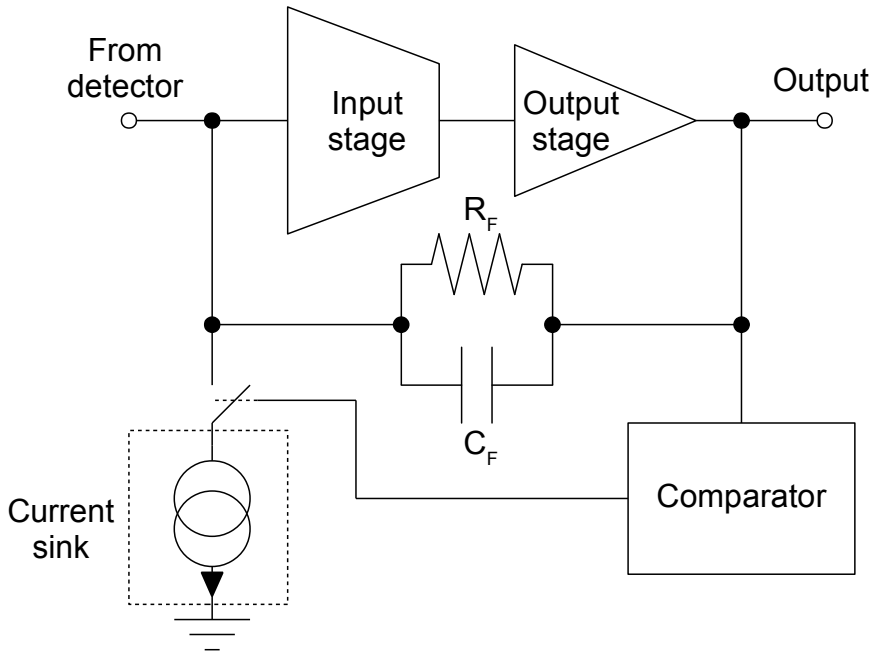

Figure 3.4: Block diagram of a preamplifier channel. Please notice that the sign of the current generator of the current sink block depends on the sign of the charge carriers released by the detector during the events. R_F is an external 0402 1 GΩ thin-film resistor. C_F is a digitally switchable capacitor that can assume the following values: 0.2 pF, 0.5 pF, 0.7 pF and 1 pF. The comparator is configured as a Schmitt-trigger that activates the switch of the current sink if the output signal saturates.

Figure 3.4 shows that every preamplifier channel consists of four main blocks. The first consists of the input and gain stage of the operational amplifier. We will generally refer to this block as the "input stage" of the preamplifier. The second block is the low-impedance output stage. This one is necessary to drive the terminated 50 Ω coaxial cables. The third block is the comparator. This device is used to monitor the output signal of the preamplifier. In case of saturation this device triggers the fourth block, that is the current sink. The current sink is used to implement the fast-reset technology. This one not only reduces dramatically the dead time but also enables the energy measurement of saturated signals using a time-over-threshold algorithm. The feedback resistance is a discrete 0402 1 GΩ one, while the feedback capacitor is integrated and digitally adjustable. It can

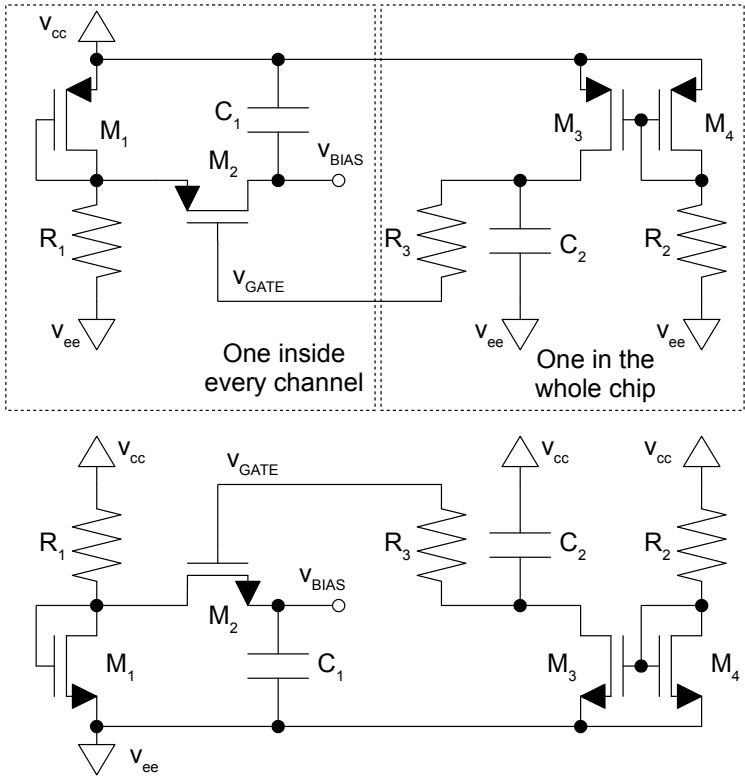

Front channels

Transistor	M_1	M_2	M_3	M_4
W [μm]	10	10	2	200
L [μm]	2	2	0.5	0.5

Front channels

Component	C_1	C_2	R_1	R_2	R_3
Value	8 pF	8 pF	33 kΩ	500 kΩ	10 kΩ

Back channel

Transistor	M_1	M_2	M_3	M_4
W [μm]	50	20	2	200
L [μm]	3	0.5	0.5	0.5

Back channel

Component	C_1	C_2	R_1	R_2	R_3
Value	6 pF	8 pF	33 kΩ	500 kΩ	10 kΩ

Figure 3.5: Schematic diagrams of the bias networks. Top: front channels bias network. Bottom: back channel bias network. In both figures V_{BIAS} controls the state of M_2. Immediately after startup the charge on C_2 is almost zero and M_2 works as a short circuit, while after M_3 has charged C_2 the transistor M_2 behaves like a resistance with very high value and filters V_{BIAS} together with C_1.

assume the following values: 0.2 pF, 0.5 pF, 0.7 pF and 1 pF.

Every block is biased with a reference voltage. This one comes from a dedicated bias block (figure 3.5). Since the front channels and the back channel are based on complementary designs, there are two kinds of bias blocks in the chip. The bias block also includes a bootstrap device. There are two of these in the chip: one for the back channel and one in common to all the front channels. The bias block not only provides the reference signal but also applies a low-frequency filter to it in order to minimize the noise induced in the CSP from the power lines. Such low-frequency filtering could induce delays during the power-up procedure. In order to have the circuit ready and running immediately after power-up a simple additional circuit was added, as can be seen in figure 3.5. The resistor R_1 induces a current in the transistor M_1 that is configured as a transdiode. We can replicate the current of M_1 applying to other transistors with the same dimensions its gate voltage. The drain current of M_1 is affected by the noise induced by the power supplies and such noise affects directly the performance of the whole circuit. Such voltage reference thus must be filtered. This is achieved with a low-frequency R-C filter. The resistance is made with the transistor M_2 in under-threshold condition. During the power-up phase the charge on C_3 is approximately zero. This means that the voltage V_{GATE} is almost equal to V_{CC} in the back channel and to V_{EE} in the front ones. M_3 replicates the current of M_4 with a de-multiplication factor. In this way we can produce a very small current without the need for very big resistors. The current generated from M_3 charges C_3 so that V_{GATE} progressively reaches the opposite power rail. Immediately after the power-up M_2 behaves like a short-circuit and the gate voltage of M_1 is sampled on C_1. After $\approx$1.5 ms, V_{GATE} in the front channels has reached V_{CC} while in the back channel has reached V_{EE}. In both circuits M_1 starts to behave like a high-valued resistance achieving together with C_1 a very-low-frequency filtering on V_{BIAS}. In this way the bias voltage can be propagated to all the blocks of the circuit with an almost negligible amount of noise. The two V_{GATE} lines are connected to external pads and can be forced to the desired level by the user in case of biasing problems.

3.3 The fast-reset technique

If the energy of an event inside the detector is higher than the dynamic range of the charge-sensitive preamplifier, saturation occurs. In this condition the preamplifier is blind and the output signal is completely distorted and contains no information. The period is which the preamplifier is saturated is thus called dead-time. The duration of

the dead-time is generally longer than the characteristic time dictated by the feedback capacitor and resistance. However it depends on the amount of charge released by the high-energy event, the dynamic range of the preamplifier and the value of the feedback resistor. Discrete components have a higher breakdown voltage respect to integrated ones. The scaling of the integrated technologies leads to the progressive reduction of the maximum voltage that can be applied to the components without permanent damage. In a charge-sensitive preamplifier the dynamic range is limited by the output voltage excursion, which, in turn, is limited by the power rails of the circuit. This means that ASIC CSPs have an intrinsically lower dynamic range respect to traditional ones made with discrete components [17, 18].

In case of saturation the output signal loses its information but the charge coming from the detector is not completely lost. That charge is still trapped on the parasitic capacitances of the input node and can be measured with proper methods. The fast-reset technique, as previously mentioned, not only reduces dramatically the dead-time but also allows to perform high-resolution spectroscopy even if the preamplifier is in deep saturation condition. This is achieved by means of a time-over-threshold technique [19]. The comparator in figure 3.4 is configured as a Schmitt-trigger. It is activated if the output voltage crosses the threshold of saturation. The comparator signal triggers the switch that connects the current sink to the input node. The current sink is a precise and constant current generator. When the switch is closed the current sink starts to drain charge from the input node. The output voltage of the preamplifier reaches the predefined baseline level when the residual charge on the input node becomes zero. In that condition the comparator switches again and the reset procedure finishes. Being I the precise and constant current generated by the current sink block, Q the charge trapped on the input node when saturation occurs and T the duration of the fast-reset process, it is straightforward that $Q = I \cdot T$. The analysis of the duration of the square pulses produced by the comparator can give high-resolution spectroscopic information even in case of deep saturation of the output stage of the CSP. Moreover the reset speed is typically around 10 MeV/μs. This means that even for energies of some hundreds of MeV the reset times are no longer than some tens of μs, with a dead-time reduction of 2-3 orders of magnitude. After the reset the CSP is immediately ready to process new detector signals. This feature could be very useful also for decay spectroscopy. In this case an heavy ion stopped in a germanium detector releases a big amount of energy. After a short time the ion decays emitting low-energy gamma radiation. A charge-sensitive

preamplifier equipped with fast-reset device would be able to measure the high energy of the impact, reset quickly and then be ready after some microseconds to measure the energy of the emitted photons in a conventional way. The fast-reset device is used just to minimize the dead-time in the front channels while it is used to extend the dynamic range of the back channel. For this reason the comparator signals of the front channels of the ASIC are not connected to any pad. The fast-reset process starts when the output voltage crosses the threshold of saturation and ends when the predefined baseline is restored. This means that the duration of the reset is proportional to the amount of charge present on the input node when saturation occurs. This charge is constituted mainly by the one released during the last event, but some residual charge of previous ones can be still present. This charge is directly proportional to the output voltage baseline of the CSP. This unwanted charge is summed up with the one released by the last event and can deteriorate significantly the energy information carried by the duration of the reset process. For this reason an additional algorithm is needed, that can correct the spectra obtained from the comparator signals from the baseline dependency.

Important remarks about the circuit descriptions of the following sections

As mentioned before the front channels and the back channel are based on complementary designs. This means that each pmos of the first circuit corresponds to an nmos in the second one and vice versa. The component enumeration in the schematic diagrams reflect this complementarity. The description of the working principles, except where otherwise indicated, is referred to the "front" version of every circuit block. The comprehension of the "back" version of these circuits is trivial: all the information can be easily deducted from the description of the "front" counterpart.

3.4 The input stage

The input stage circuit, depicted in figures 3.6 and 3.12 is quite simple and self-explanatory. The chosen structure is based on a differential pair (M_1 and M_2) as input with a cascoded mirror as active load. The second stage is based on a common-source gain unit with Miller compensation. The dimensions and the operating point of the input transistors were carefully chosen in order to fulfil noise and speed requirements. From one side we would like M_1 and M_2 to have the maximum W/L ratio possible, in order to maximize the transconductance and achieve the best speed and gain performance with lowest amount of channel noise at the input. Unfortunately we could choose the shortest channel length available (0.35 μm) because the 1/f noise goes as the inverse of the transistor area. The dimensions chosen (3200 μm/0.4 μm) are thus a trade-off between best transconductance and lowest 1/f noise at the input. The cascode transistors M_3 and M_4 are used both to increase the output resistance of the input stage and to minimize the effect of the big gate-drain parasitic capacitance of the input transistors. The mirror M_5/M_6 is not cascoded due to headroom reasons. The enhancement of the output resistance operated by the cascode transistors is useful also to reduce the dimensions of the Miller capacitance required to perform compensation. This capacitor can be adjusted via digital slow-control. In this way the bandwidth can be reduced in case of low detector capacitance in order to avoid ringing or instability. On the other hand it can also be enhanced in case of more capacitive detectors in order to minimize the risetime. The tail generator is made with the transistors M_9, M_{10} and M_{11}. The first one is directly connected to the input differential pair. Transistors M_{10} and M_{11} Can be turned off by means of M_7 and M_8, that act as switches connected to the I^2C slow-control. In this way the current flowing in the input stage can be adjusted. This feature was mainly planned to reduce the bandwidth of the preamplifier in case of cryogenic applications, where noise is not a concern. The reduction of the bias current of the input stage does not affect the DC gain of the circuit since the reduction of transconductance of M_1 and M_2 is counter-balanced by the enhancement of the output resistances of the cascode and mirror transistors. The bandwidth reduction is possible since the frequency of the Miller compensation pole depends on the output resistance of the input stage. The choice of a differential input structure instead of a single-ended one was mainly influenced by the following reason. The feedback loop of the charge-sensitive preamplifier is made with a discrete resistance and an integrated capacitor.

The feedback resistor not only impedes an otherwise unavoidable saturation of the

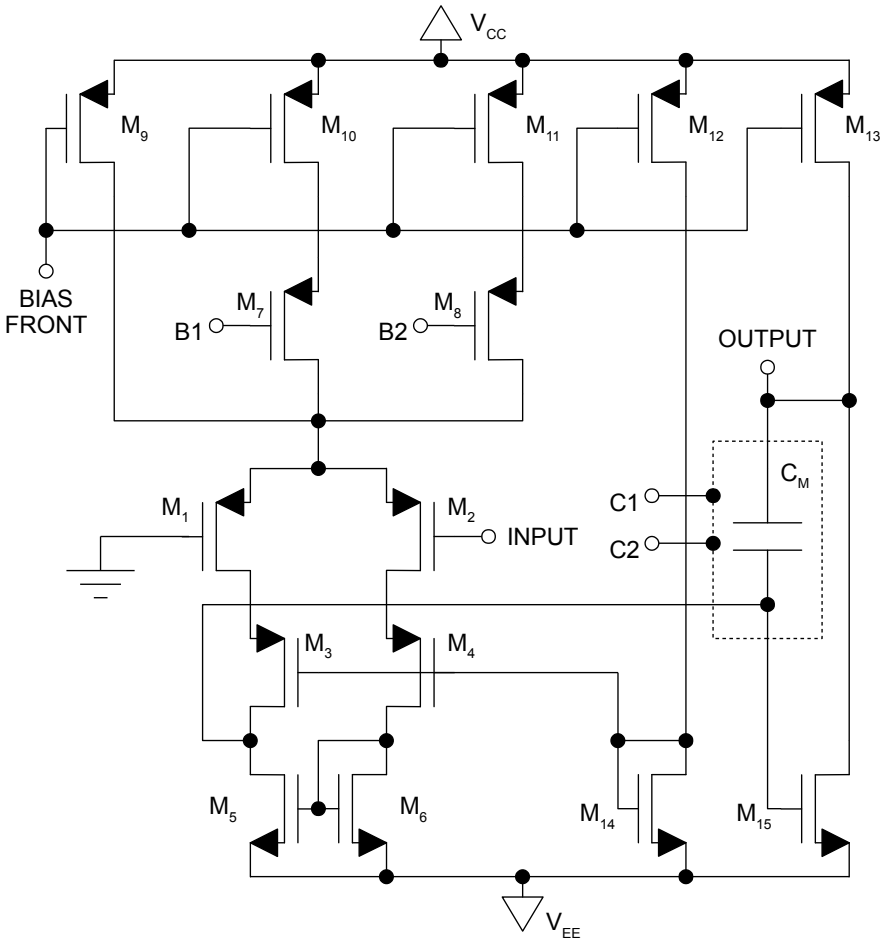

The capacitance C_M can be adjusted with the controls C1 and C2 and can assume the following values: 2 pF, 3 pF, 4 pF and 5 pF.

Transistor	M_1	M_2	M_3	M_4	M_5	M_6	M_7	M_8
W [μm]	3200	3200	200	200	120	120	50	50
L [μm]	0.4	0.4	0.35	0.35	6	6	0.5	0.5

Transistor	M_9	M_{10}	M_{11}	M_{12}	M_{13}	M_{14}	M_{15}
W [μm]	25	50	50	3	70	100	200
L [μm]	3	3	3	3	3	10	0.5

Figure 3.6: Schematic diagram of the input stage of front channel.

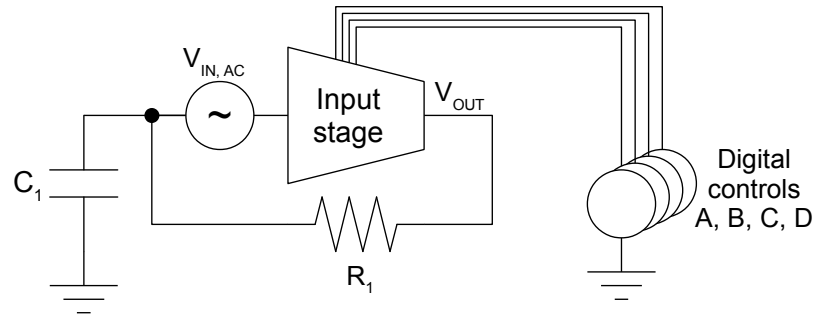

Figure 3.7: Schematic diagram of the test bench used to perform AC analysis on the input stage circuit. C_1 is equal to 1 F, R_1 is equal to 1 TΩ. A, B, C and D are the digital slow-controls. These controls are named A, B, C and D and are in "0 state" when equal to 0 V and in "1 state" when equal to 5.2 V.

CSP but also determines the output DC bias point of the preamplifier. Since no DC current is flowing from the detector into the CSP (it is AC coupled) the DC voltage level at the output is equal to the one on the gate of the input transistor. If a single-ended input structure was chosen, the output bias voltage of the preamplifier would be equal to the threshold voltage of the input transistors plus overdrive. The preamplifier was designed with the capability of directly drive a terminated 50 Ω coaxial cable and such DC bias voltage at the output would induce a consistent and useless power dissipation on the load resistance. The choice of a differential input, even if slightly unfavourable for gain and noise, can on the other hand ensure an almost zero DC bias voltage at the output, with great reduction of the power dissipation. Another solution could be the use of integrated active transconductors as feedback resistors. This solution unties the DC bias output voltage from the one on the gate of the input transistor. A physical resistance was preferred because of its lower noise and V-I curve linearity. Both this aspects have in fact great impact on the resolution of the preamplifier. The AC analysis of the input stage, both in its schematic and post-layout form, was performed on the test bench in figure 3.7. The output of the circuit was connected to a 1 TΩ resistor in series with a huge capacitance (1 F). In this way the circuit automatically reaches the correct bias point. A voltage AC generator was connected between the capacitor and the inverting input of the circuit. Figures 3.8 and 3.10 shows the Bode diagrams of the circuit AC response (gain and phase) for different conditions of the digital slow-controls. These controls are named A, B, C and D and are in "0 state" when equal to 0 V and in "1 state" when equal to 5.2 V. Figures 3.9 and 3.11 shows the same diagrams for post-layout simulations.

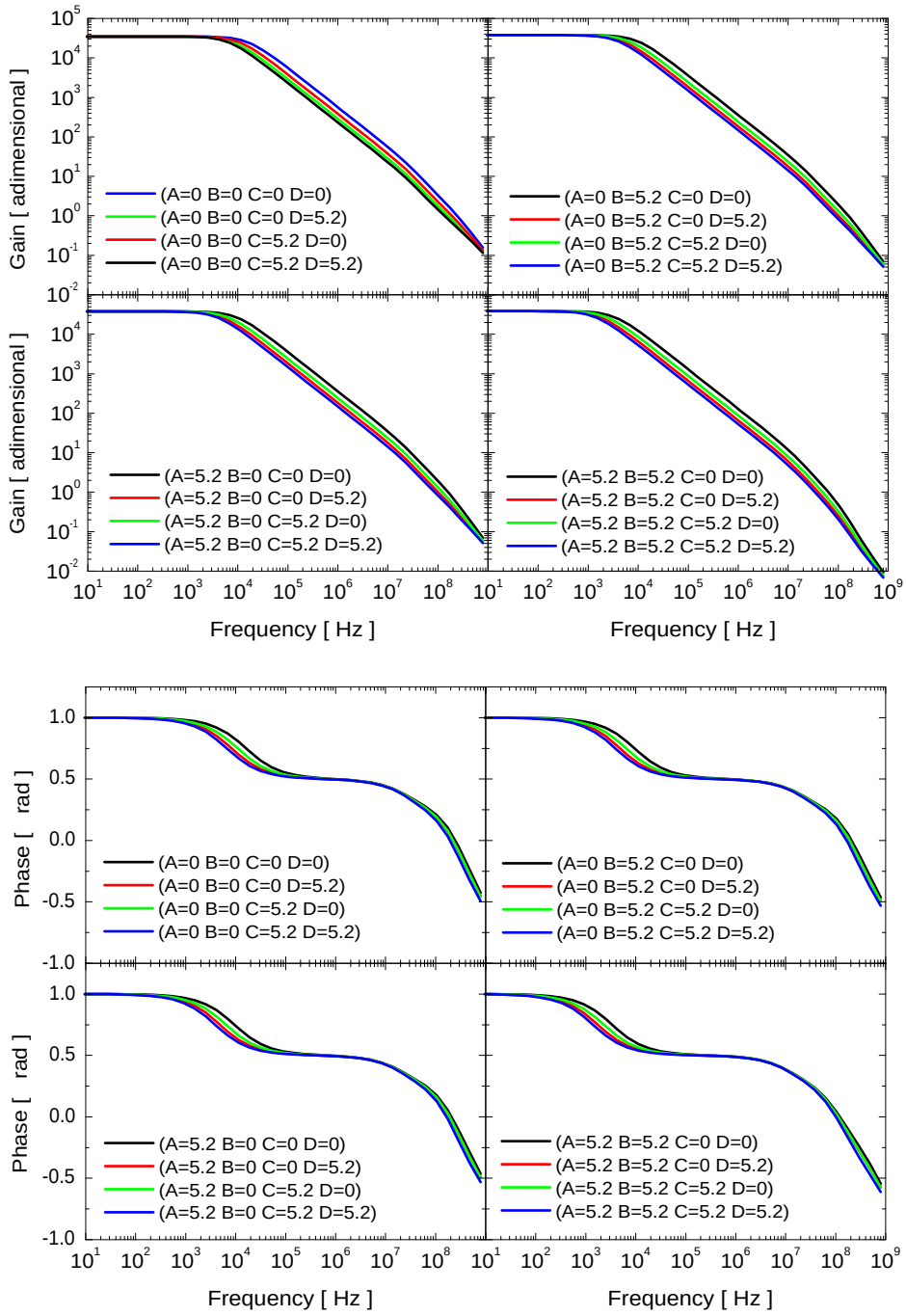

Figure 3.8: Top: Bode gain diagram of the input stage of the front preamplifier. Bottom: Bode phase diagram of the input stage of the front preamplifier. The digital slow controls A and B are connected to the input bias current controls while C and D adjust the Miller compensation capacitor.

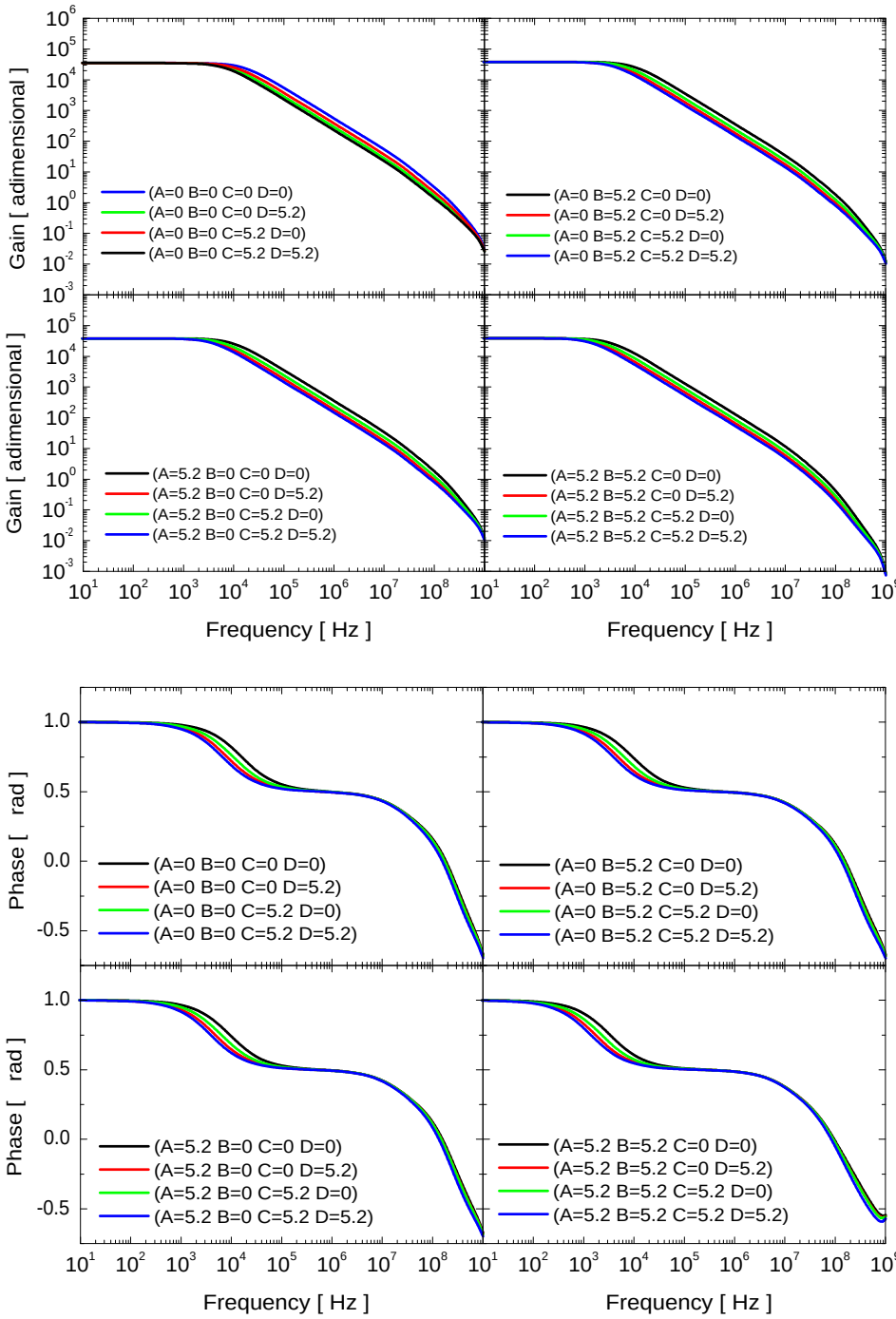

Figure 3.9: Top: Bode gain diagram of the input stage of the front preamplifier. Bottom: Bode phase diagram of the input stage of the front preamplifier. The digital slow controls A and B are connected to the input bias current controls while C and D adjust the Miller compensation capacitor. Post-layout simulation.

Table 3.1: Gain-bandwidth product [MHz] of the input stage (front channel) for different conditions of the digital slow-controls A, B, C and D [V].

(A=0 B=0 C=0 D=0)	(A=0 B=0 C=0 D=5.2)	(A=0 B=0 C=5.2 D=0)	(A=0 B=0 C=5.2 D=5.2)
5.629E+02	2.885E+02	3.816E+02	2.320E+02
(A=0 B=5.2 C=0 D=0)	(A=0 B=5.2 C=0 D=5.2)	(A=0 B=5.2 C=5.2 D=0)	(A=0 B=5.2 C=5.2 D=5.2)
3.584E+02	1.835E+02	2.428E+02	1.475E+02
(A=5.2 B=0 C=0 D=0)	(A=5.2 B=0 C=0 D=5.2)	(A=5.2 B=0 C=5.2 D=0)	(A=5.2 B=0 C=5.2 D=5.2)
3.584E+02	1.835E+02	2.428E+02	1.475E+02
(A=5.2 B=5.2 C=0 D=0)	(A=5.2 B=5.2 C=0 D=5.2)	(A=5.2 B=5.2 C=5.2 D=0)	(A=5.2 B=5.2 C=5.2 D=5.2)
1.297E+02	6.638E+01	8.784E+01	5.337E+01

Table 3.2: DC gain of the input stage (front channel) for different conditions of the digital slow-controls A, B, C and D [V].

(A=0 B=0 C=0 D=0)	(A=0 B=5.2 C=0 D=0)	(A=5.2 B=0 C=0 D=0)	(A=5.2 B=5.2 C=0 D=0)
3.483E+04	3.793E+04	3.793E+04	3.838E+04
(A=0 B=0 C=0 D=5.2)	(A=0 B=5.2 C=0 D=5.2)	(A=5.2 B=0 C=0 D=5.2)	(A=5.2 B=5.2 C=0 D=5.2)
3.483E+04	3.793E+04	3.793E+04	3.839E+04
(A=0 B=0 C=5.2 D=0)	(A=0 B=5.2 C=5.2 D=0)	(A=5.2 B=0 C=5.2 D=0)	(A=5.2 B=5.2 C=5.2 D=0)
3.483E+04	3.793E+04	3.793E+04	3.839E+04
(A=0 B=0 C=5.2 D=5.2)	(A=0 B=5.2 C=5.2 D=5.2)	(A=5.2 B=0 C=5.2 D=5.2)	(A=5.2 B=5.2 C=5.2 D=5.2)
3.483E+04	3.793E+04	3.793E+04	3.839E+04

Table 3.3: Frequency [Hz] of the dominant pole of the input stage (front channel) for different conditions of the digital slow-controls A, B, C and D [V].

(A=0,B=0,C=0,D=0)	(A=0,B=0,C=0,D=5.2)	(A=0,B=0,C=5.2,D=0)	(A=0,B=0,C=5.2,D=5.2)
-1.62E+04	-8.29E+03	-1.10E+04	-6.66E+03
(A=0,B=5.2,C=0,D=0)	(A=0,B=5.2,C=0,D=5.2)	(A=0,B=5.2,C=5.2,D=0)	(A=0,B=5.2,C=5.2,D=5.2)
-9.46E+03	-4.84E+03	-6.41E+03	-3.89E+03
(A=5.2,B=0,C=0,D=0)	(A=5.2,B=0,C=0,D=5.2)	(A=5.2,B=0,C=5.2,D=0)	(A=5.2,B=0,C=5.2,D=5.2)
-9.46E+03	-4.84E+03	-6.41E+03	-3.89E+03
(A=5.2,B=5.2,C=0,D=0)	(A=5.2,B=5.2,C=0,D=5.2)	(A=5.2,B=5.2,C=5.2,D=0)	(A=5.2,B=5.2,C=5.2,D=5.2)
-3.38E+03	-1.73E+03	-2.29E+03	-1.39E+03

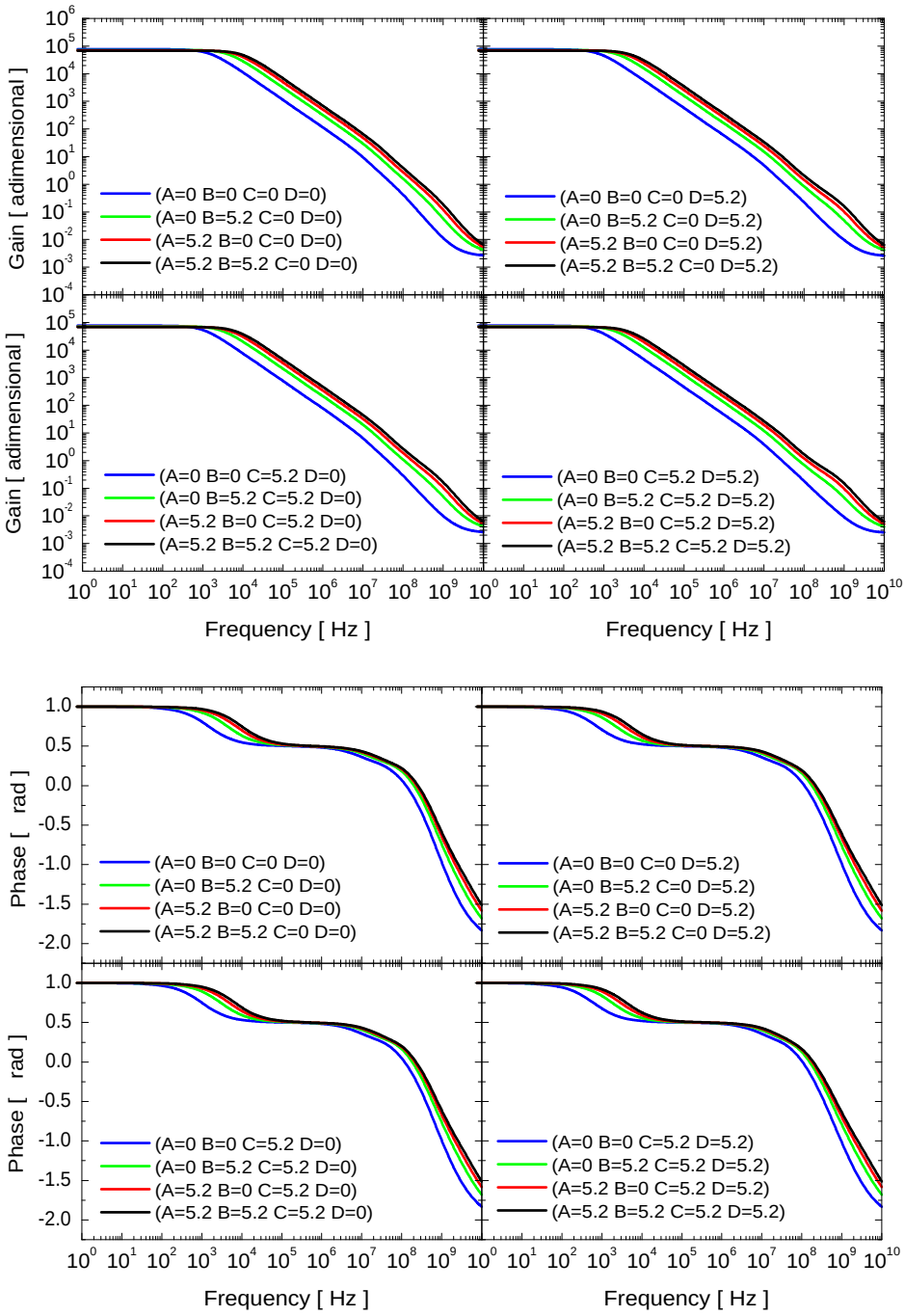

Figure 3.10: Top: Bode gain diagram of the input stage of the back preamplifier. Bottom: Bode phase diagram of the input stage of the back preamplifier. The digital slow controls A and B are connected to the input bias current controls while C and D adjust the Miller compensation capacitor.

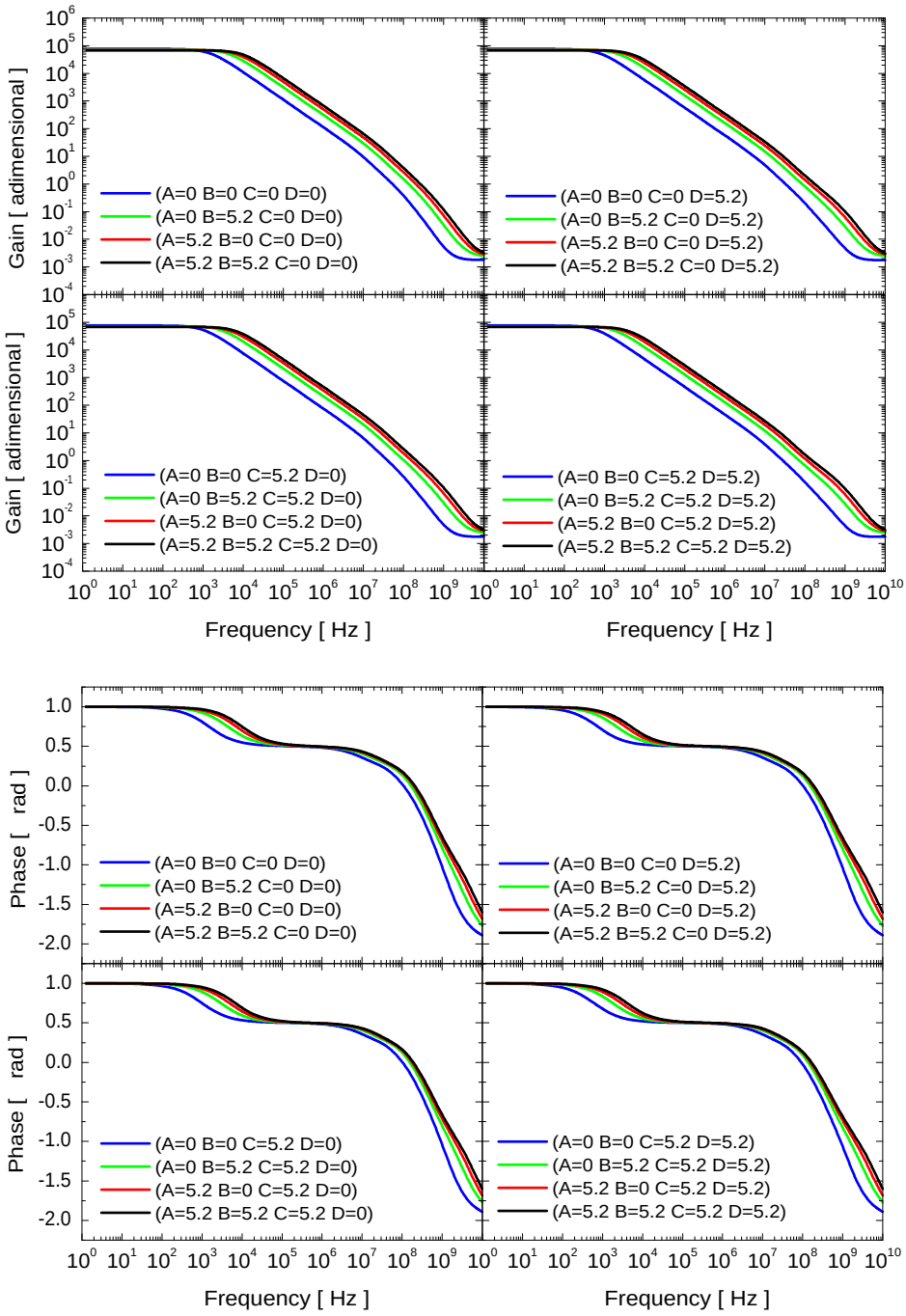

Figure 3.11: Top: Bode gain diagram of the input stage of the back preamplifier. Bottom: Bode phase diagram of the input stage of the back preamplifier. The digital slow controls A and B are connected to the input bias current controls while C and D adjust the Miller compensation capacitor. Post-layout simulation.

Table 3.4: Gain-bandwidth product [MHz] of the input stage (back channel) for different conditions of the digital slow-controls A, B, C and D [V].

(A=0 B=0 C=0 D=0)	(A=0 B=0 C=0 D=5.2)	(A=0 B=0 C=5.2 D=0)	(A=0 B=0 C=5.2 D=5.2)
1.131E+02	5.761E+01	7.636E+01	4.627E+01
(A=0 B=5.2 C=0 D=0)	(A=0 B=5.2 C=0 D=5.2)	(A=0 B=5.2 C=5.2 D=0)	(A=0 B=5.2 C=5.2 D=5.2)
3.157E+02	1.606E+02	2.130E+02	1.290E+02
(A=5.2 B=0 C=0 D=0)	(A=5.2 B=0 C=0 D=5.2)	(A=5.2 B=0 C=5.2 D=0)	(A=5.2 B=0 C=5.2 D=5.2)
5.050E+02	2.568E+02	3.405E+02	2.061E+02
(A=5.2 B=5.2 C=0 D=0)	(A=5.2 B=5.2 C=0 D=5.2)	(A=5.2 B=5.2 C=5.2 D=0)	(A=5.2 B=5.2 C=5.2 D=5.2)
6.840E+02	3.475E+02	4.609E+02	2.789E+02

Table 3.5: DC gain of the input stage (back channel) for different conditions of the digital slow-controls A, B, C and D [V].

(A=0 B=0 C=0 D=0)	(A=0 B=0 C=0 D=5.2)	(A=0 B=0 C=5.2 D=0)	(A=0 B=0 C=5.2 D=5.2)
7.638E+04	7.638E+04	7.638E+04	7.638E+04
(A=0 B=5.2 C=0 D=0)	(A=0 B=5.2 C=0 D=5.2)	(A=0 B=5.2 C=5.2 D=0)	(A=0 B=5.2 C=5.2 D=5.2)
7.192E+04	7.192E+04	7.192E+04	7.192E+04
(A=5.2 B=0 C=0 D=0)	(A=5.2 B=0 C=0 D=5.2)	(A=5.2 B=0 C=5.2 D=0)	(A=5.2 B=0 C=5.2 D=5.2)
6.975E+04	6.975E+04	6.975E+04	6.975E+04
(A=5.2 B=5.2 C=0 D=0)	(A=5.2 B=5.2 C=0 D=5.2)	(A=5.2 B=5.2 C=5.2 D=0)	(A=5.2 B=5.2 C=5.2 D=5.2)
6.823E+04	6.823E+04	6.823E+04	6.823E+04

Table 3.6: Frequency [Hz] of the dominant pole of the input stage (back channel) for different conditions of the digital slow-controls A, B, C and D [V].

(A=0 B=0 C=0 D=0)	(A=0 B=0 C=0 D=5.2)	(A=0 B=0 C=5.2 D=0)	(A=0 B=0 C=5.2 D=5.2)
1.481E+03	7.543E+02	9.997E+02	6.057E+02
(A=0 B=5.2 C=0 D=0)	(A=0 B=5.2 C=0 D=5.2)	(A=0 B=5.2 C=5.2 D=0)	(A=0 B=5.2 C=5.2 D=5.2)
4.390E+03	2.234E+03	2.961E+03	1.793E+03
(A=5.2 B=0 C=0 D=0)	(A=5.2 B=0 C=0 D=5.2)	(A=5.2 B=0 C=5.2 D=0)	(A=5.2 B=0 C=5.2 D=5.2)
7.240E+03	3.681E+03	4.881E+03	2.955E+03
(A=5.2 B=5.2 C=0 D=0)	(A=5.2 B=5.2 C=0 D=5.2)	(A=5.2 B=5.2 C=5.2 D=0)	(A=5.2 B=5.2 C=5.2 D=5.2)
1.002E+04	5.093E+03	6.755E+03	4.088E+03

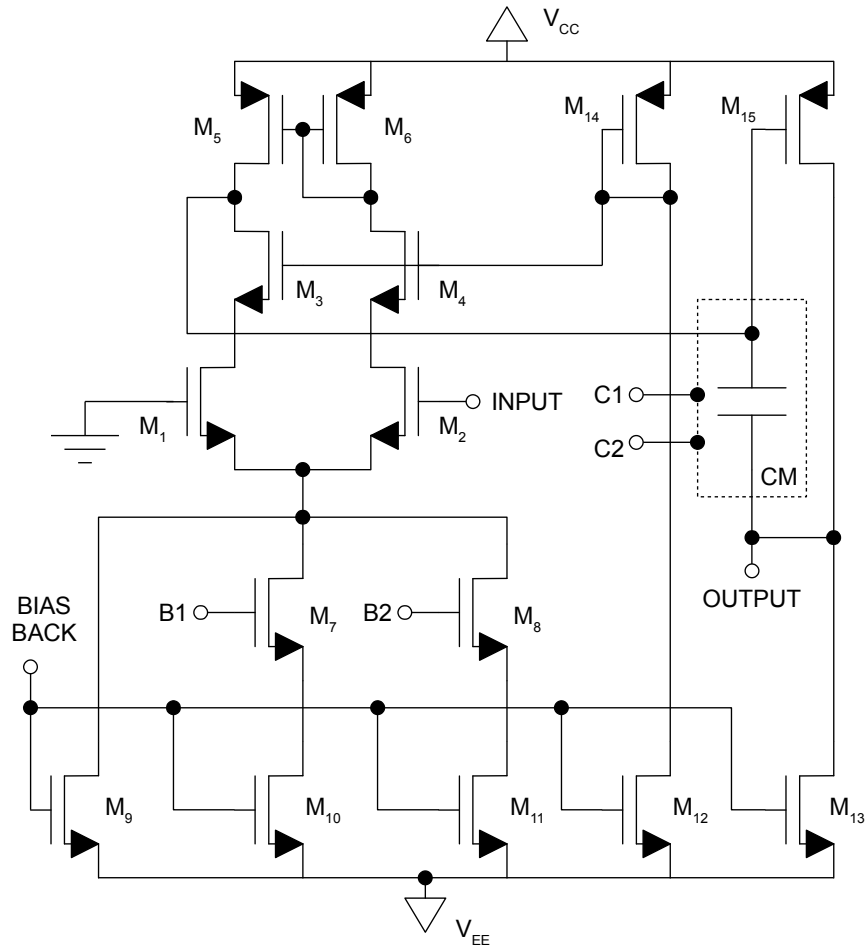

The capacitance C_M can be adjusted with the controls C1 and C2 and can assume the following values: 2 pF, 3 pF, 4 pF and 5 pF.

Transistor	M_1	M_2	M_3	M_4	M_5	M_6	M_7	M_8
W [μm]	3200	3200	200	200	480	480	50	50
L [μm]	0.8	0.8	0.35	0.35	3.5	3.5	0.5	0.5

Transistor	M_9	M_{10}	M_{11}	M_{12}	M_{13}	M_{14}	M_{15}
W [μm]	75	150	300	50	160	40	500
L [μm]	5	5	5	15	1	1	0.5

Figure 3.12: Schematic diagram of the input stage of the back channel.

3.5 The output stage

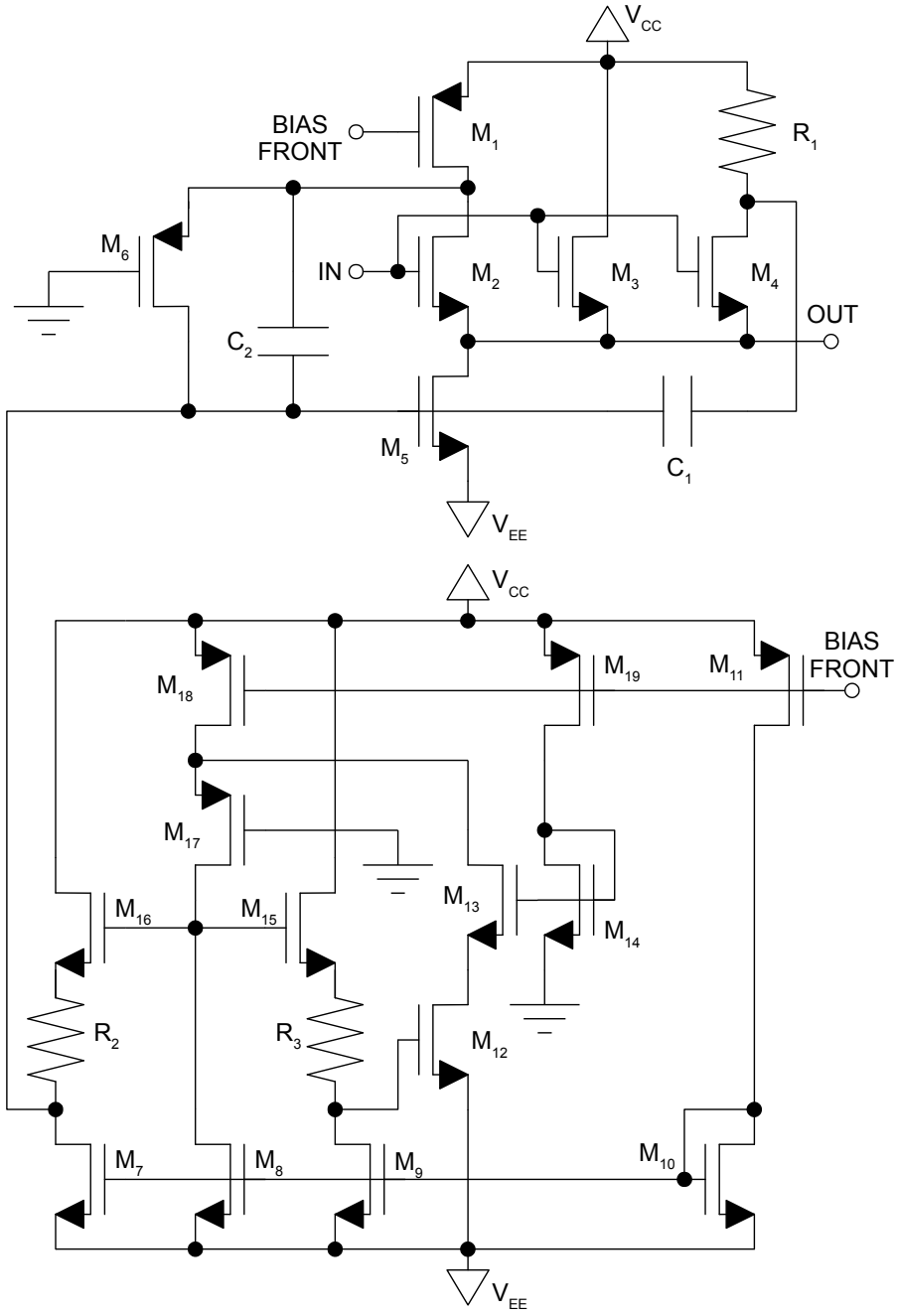

Figure 3.13: Schematic diagram of the output stage of front channel. The transistor dimensions and other component values are reported in table 3.7.

Table 3.7: Transistor dimensions and component values of the output stage of the front channels. For diagram please refer to figure 3.13.

Transistor	M_1	M_2	M_3	M_4	M_5	M_6	M_7	M_8	M_9	M_{10}
W [μm]	20	400	200	40	400	50	1	1	1	1
L [μm]	3	0.5	0.5	0.5	0.5	0.5	1	0.5	1	0.5

Transistor	M_{11}	M_{12}	M_{13}	M_{14}	M_{15}	M_{16}	M_{17}	M_{18}	M_{19}
W [μm]	5	200	40	10	10	10	10	20	5
L [μm]	3	0.5	0.5	0.5	0.5	0.5	0.5	3	3

Component	R_1	R_2	R_3	C_1	C_2
Value	10k	60k	60k	3 pF	3 pF

The output stage (figures 3.13 and 3.22) has a complex structure based on the original idea of the White follower. It is capable of driving a terminated 50 Ω coaxial cable. Its output voltage excursion is directly proportional to the dynamic range of the preamplifier. There is no need for a rail-to-rail driving capability. Front channels in fact will just receive hole signals while the back channel only electron ones. For this reason the output stage of the front channels was designed in order to maximize the negative voltage swing while the back one works on the positive side. We will now describe in detail the "front" output stage. We will omit the description of the "back" one due to its perfect complementarity. In order to understand the basic mechanisms of this circuit we will analyse first the simplified version in figure 3.14. The circuit is based on a source-follower stage. The transistor M_5 acts as a driver for transistor M_2. The transistor M_1 works as a current generator and all its current is absorbed by M_2 and I_{REF}. When the input voltage goes low the current flowing through M_2 tends to decrease. The excess current generated by M_1 and not absorbed by M_2 is collected by M_6 and injected on the gate of M_5. This means that, when the input voltage goes low, the feedback path of M_1 and M_6 senses that the current flowing through M_2 is decreasing. The driver M_5 is thus forced to generate a higher current. Equilibrium is reached when the original current of M_2 is restored. The best part of the current generated by the driver transistor however does not flow through M_2 but is used to drive the output load R_{LOAD}. In this way this stage can drive a 100 Ω load down to V_{EE}. If the detector is AC coupled to the CSP the average DC current that flows through the bypass capacitor is zero. This means that the baseline voltage undergoes a net shift V_{SHIFT}. If $\langle r \rangle$ is the average event rate, $\langle Q \rangle$ the average charge released during an event and C_F the feedback capacitor, the baseline voltage shift

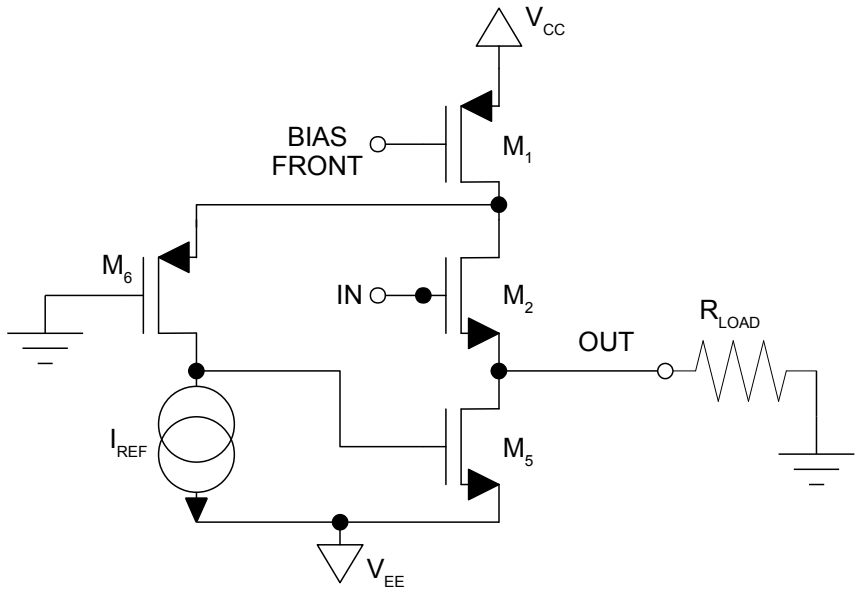

Figure 3.14: Schematic diagram of a simplified version of the front channel output stage. Load resistance is added for clarity.

is equal to

$$V_{SHIFT} = \frac{\langle r \rangle \cdot \langle Q \rangle}{C_F}. \tag{3.1}$$

The sign of this voltage shift is opposite to the one of the signals generated during the events. In the case of the front channel the output waveforms produced by hole signals are negative and the average baseline shift if positive. If the output stage needs to drive a positive output voltage the driver transistor M_5 could be temporary shut down by the feedback loop of M_1 and M_6. If the output voltage must rapidly cross the zero-level (from above to under) M_5 must start to absorb current quickly. However if M_5 is shut down due to the positive baseline it takes several nanoseconds to be operative again. This phenomenon introduces cross-over distortions on the waveforms that make the pulse-shape analysis completely useless. In order to avoid such distortions M_5 should never be shut down completely but must have a predictable minimum current flow even when the output voltage level is positive. This is made possible by the auxiliary structure of the complete version of the circuit, represented in figure 3.13. The working principle of the complete circuit is the same as the simplified one, unless that the DC bias current of M_6 is zero. The voltage at the gate of M_5 is determined by the auxiliary structure made of the transistors from M_7 to M_{19}. The goal of this auxiliary structure is to replicate

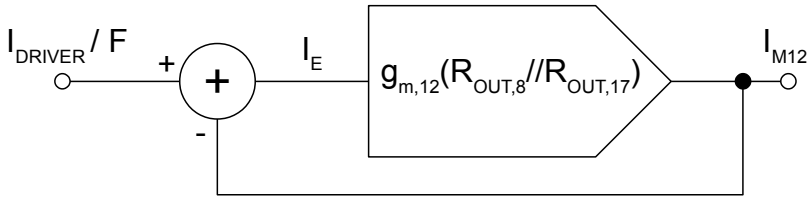

Figure 3.15: Block diagram of the feedback loop that controls the current I_{M12} that flows through the transistor M_{12}. I_{DRIVER}/F is the reference value and I_E is the error current.

on the gate of M_5 the same voltage at the gate of the reference transistor M_{12} like in a mirror. Let us define W_D and L_D the dimensions of the driver transistor M_5. The dimensions of the reference transistor M_{12} are the following: $\frac{W_D}{F}$ and L. M_{12} has thus the same channel length of M_5 and a fraction F of its width. Let us define I_{DRIVER} the current we want to flow through the driver transistor in idle condition. M_{12} is biased with a DC current equal to $\frac{I_{DRIVER}}{F}$. The choice of the width and current reduction of M_{12} is due to power dissipation reasons. In replicating the current of M_{12} on M_5, the possible asymmetries between the drain voltages of these two transistors can induce a non perfect current mirroring. Since in idle condition the drain of M_5 should be at 0 V, we want to replicate the same voltage at the drain of M_{12}. This is accomplished by the two transistors M_{13} and M_{14}. M_{14} is configured as a transdiode with source connected to ground. M_{13} share the same gate voltage of M_{14}. The reciprocal relationship of the bias currents and the physical dimensions of M_{13} and M_{14} ensure that the drain voltage of M_{12} is as close as possible to 0 V. In order M_{12} to be biased correctly, M_{18} must provide a current equal to the sum of the ones of M_{12} and M_8. The bias point of M_{12} is forced by a feedback loop made of the following components: M_8, M_9, R_3, M_{15}, M_{17}, M_{18} and M_{13}. Let us define the "error current " I_E as the difference between the current of M_{12} and the desired value $\frac{I_{DRIVER}}{F}$. Such current is collected in sequence by M_{13} and M_{17} and injected on the drain of M_8. The error current I_E thus produces a voltage variation ΔV on the gate of M_{15} equal to $-I_E \cdot (R_{OUT,8}//R_{OUT,17})$. We define $R_{OUT,8}$ and $R_{OUT,17}$ to be the output resistance of the transistors M_8 and M_{15}. Being M_9 configured as current generator and neglecting his output resistance, the difference between the gate voltages of M_{15} and M_{12} is a constant value equal to $V_{OD,15} + V_{TH,15} + R_3 \cdot I_{M9}$. $V_{OD,15}$ and $V_{TH,15}$ are respectively the overdrive and threshold voltages of M_{15} and I_{M9} the bias current of M_9. Thus the "correction current" I_{CORR} induced on M_{12} by the "error current" I_E is

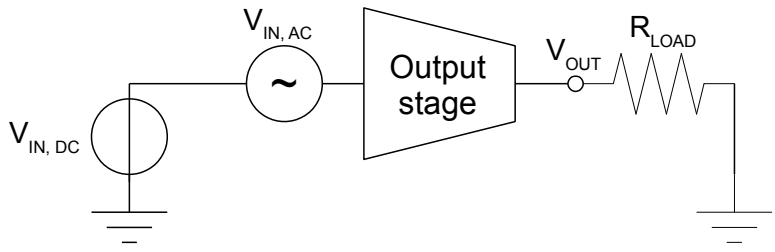

Figure 3.16: Schematic diagram of the test used to evaluate the DC and AC behaviour of the output stage, both in its schematic and post-layout form.

thus equal to

$$I_{CORR} = -I_E \cdot [g_{m,12} (R_{OUT,8} // R_{OUT,17})] . \tag{3.2}$$

This equation demonstrates that the circuit behaves as a negative feedback loop ensuring that the current on M_{12} is equal to $\frac{I_{DRIVER}}{F}$. Figure 3.15 contains the block diagram of this feedback loop. The role of the transistors M_7, M_{16} and the resistance R_2 is to replicate the gate voltage of M_{12} on M_5. For this reason the matching between M_{15} and M_{16}, R_3 and R_2 and M_9 and M_7 is crucial to achieve the best mirroring performance.

The current of M_7 is fixed and M_6 can only inject positive current on the gate of M_5. For this reason M_5 has a minimum, predictable current equal to the one of the reference transistor M_{12}. The idle current flow through M_6 is zero. If the baseline voltage of the output stage goes above 0 V, the current of M_2 becomes equal to the one of M_1, M_6 is off and the current flow of the driver transistor M_5 is equal to I_{DRIVER}. When the output signal must go under the 0 V level, M_6 starts to inject current on the gate of M_5 ensuring that the latter provides the current needed to drive the load of the terminated coaxial cable. When the output voltage must go above 0 V the maximum current that M_2 can deliver to the load is the one produced by M_1. In order to slightly improve the positive dynamic excursion of the output voltage we added the transistor M_3. This transistor can provide the necessary positive current to the load when the one coming from M_2 is not enough. The role of M_4, R_1, C_1 and C_2 is to stabilize the M_1-M_1-M_6-M_5 feedback loop. In particular C_2 works as a bootstrap for M_6 that is normally off when $V_{OUT} \geqslant 0$.

The analysis of the output stage must include a DC sweep and an AC analysis. The DC sweep is used to evaluate the dynamic excursion of the circuit and the AC analysis is used to verify the absence of undesired resonances and/or low frequency poles. The wide output voltage swing leads to an appreciable variation of the circuit operating point.

While performing AC analysis we must evaluate the small signal response of the circuit for different DC voltages at the input. To test the output stage, both in its schematic and post-layout form, we used the test bench in figure 3.16. The circuit has a very good dynamic excursion: the output voltage can reach V_{EE} even driving a terminated 50 Ω coaxial cable. The maximum positive output voltage is limited to $V_{CC} - V_{OD,3} + V_{TH,3}$ but is enough to provide the dynamic excursion required by the baseline voltage fluctuation induced by the AC detector coupling. In figures 3.17 and 3.18 we can see the DC response function of the output stage both in its front and back version, while in figures 3.19, 3.20 and 3.21 we can see the AC response function of the output stage for different DC input voltages.

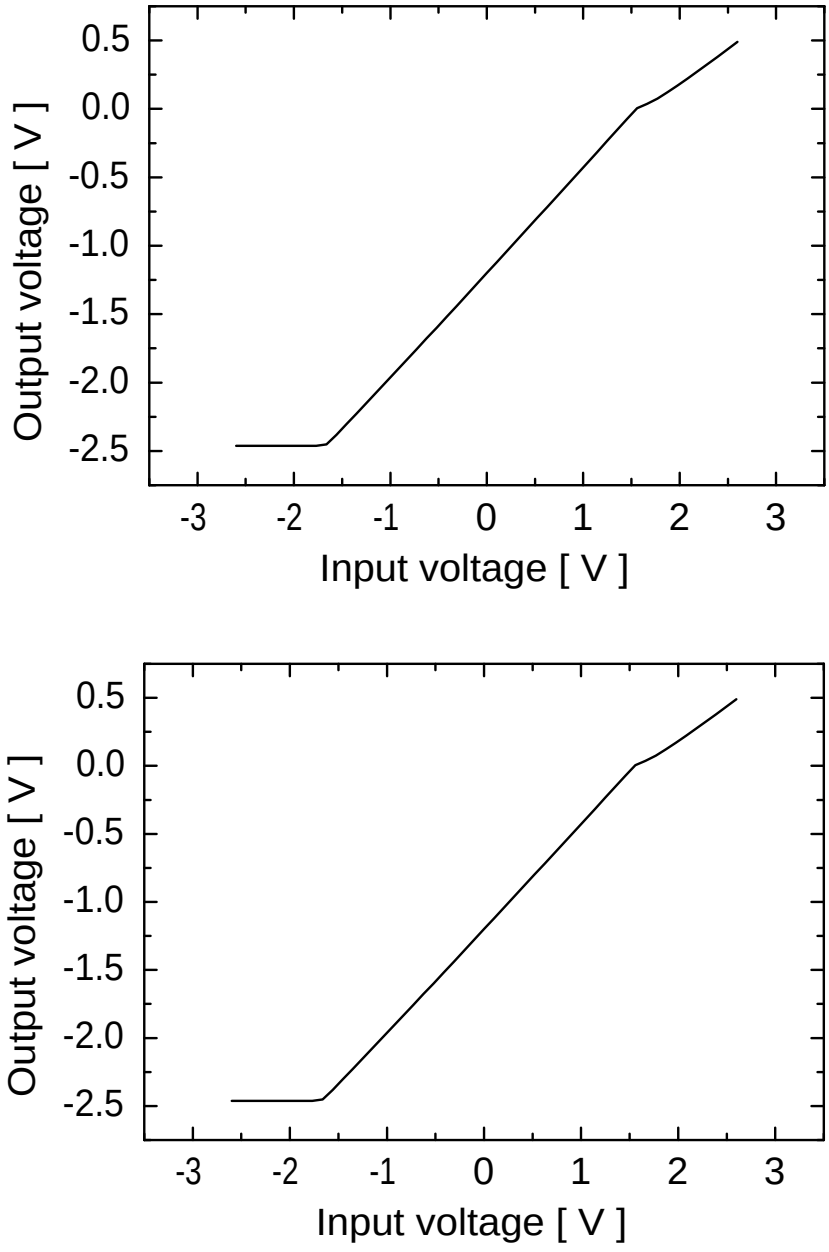

Figure 3.17: DC sweep diagrams of the output stage (front channel). The input voltage is on the x-axis while the output one is one the y-axis. The top figure shows the results obtained with the circuit in the schematic form while the bottom figure shows the post-layout ones.

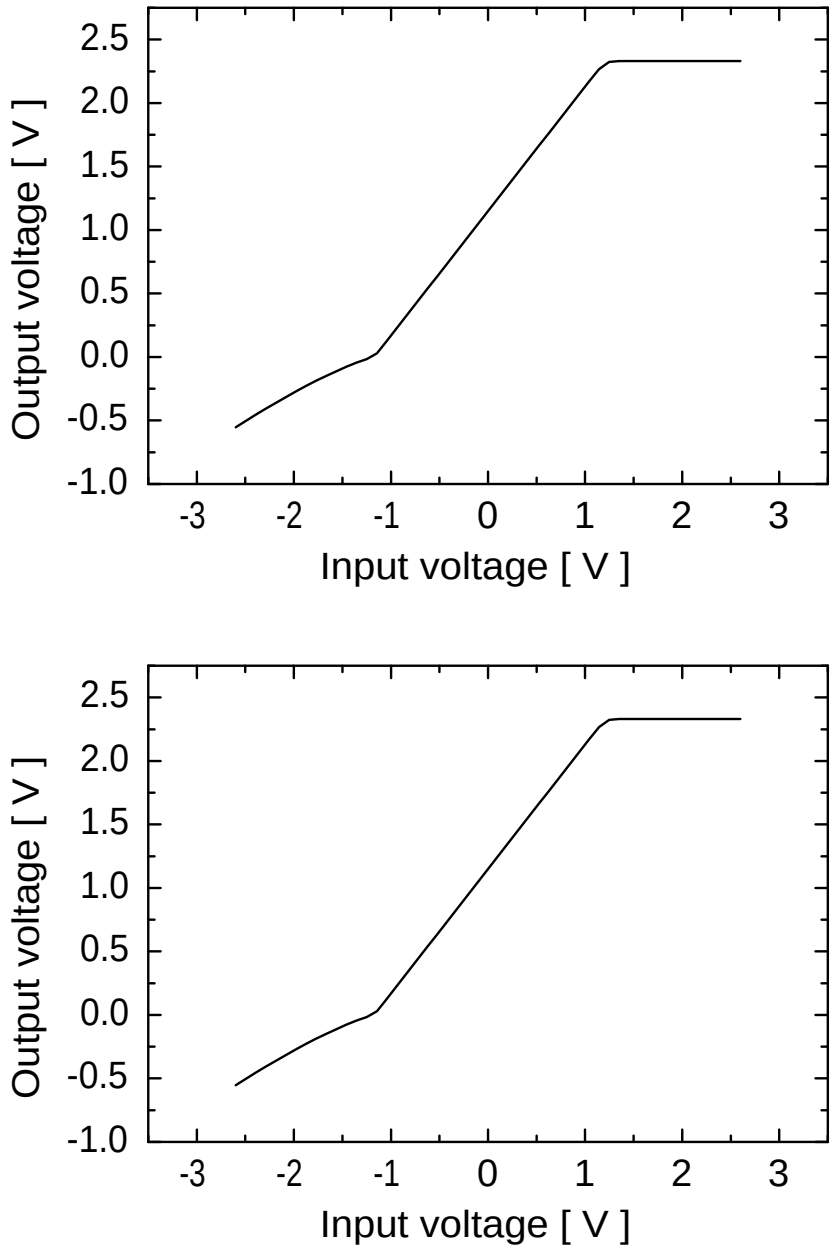

Figure 3.18: DC sweep diagrams of the output stage (back channel). The input voltage is on the x-axis while the output one is one the y-axis. The top figure shows the results obtained with the circuit in the schematic form while the bottom figure shows the post-layout ones.

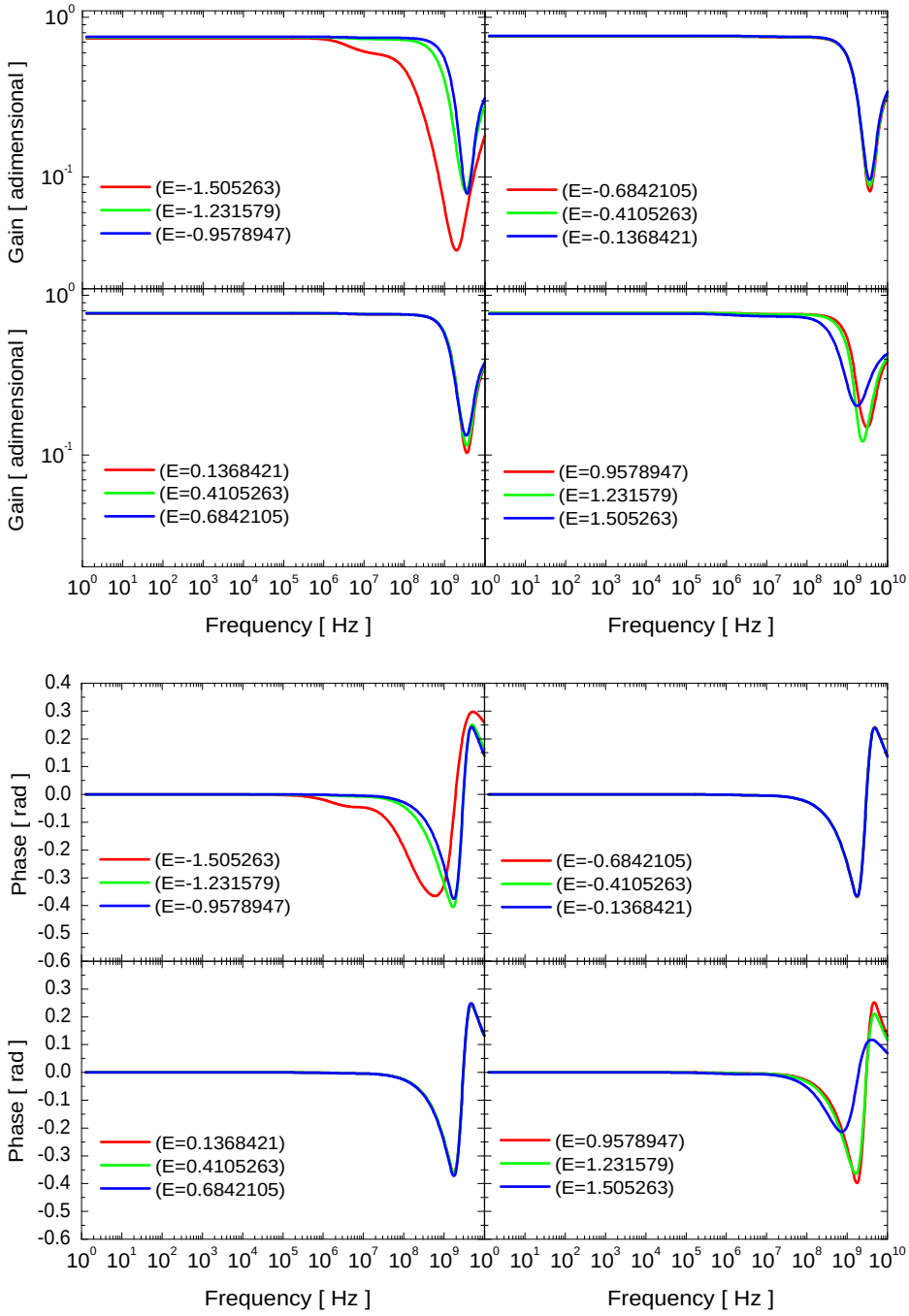

Figure 3.19: Bode diagrams of the output stage (front channel) AC response for different input DC voltages. Top: gain vs frequency. Bottom: phase vs frequency. The E parameter represent the amplitude [V] of the DC generator at the input.

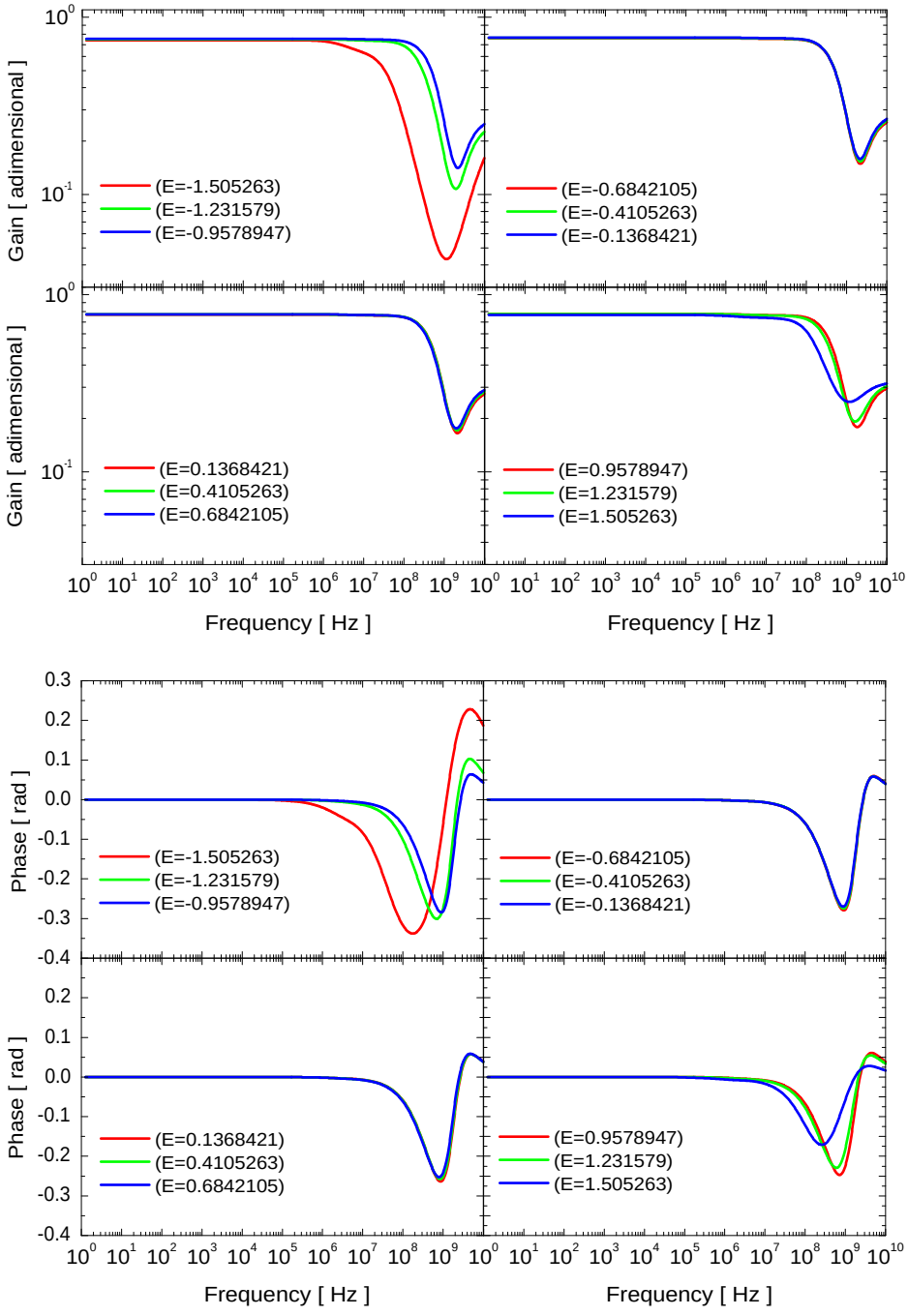

Figure 3.20: Bode diagrams of the output stage (front channel) AC response for different input DC voltages. Top: gain vs frequency. Bottom: phase vs frequency. The E parameter represent the amplitude [V] of the DC generator at the input. Post-layout simulation.

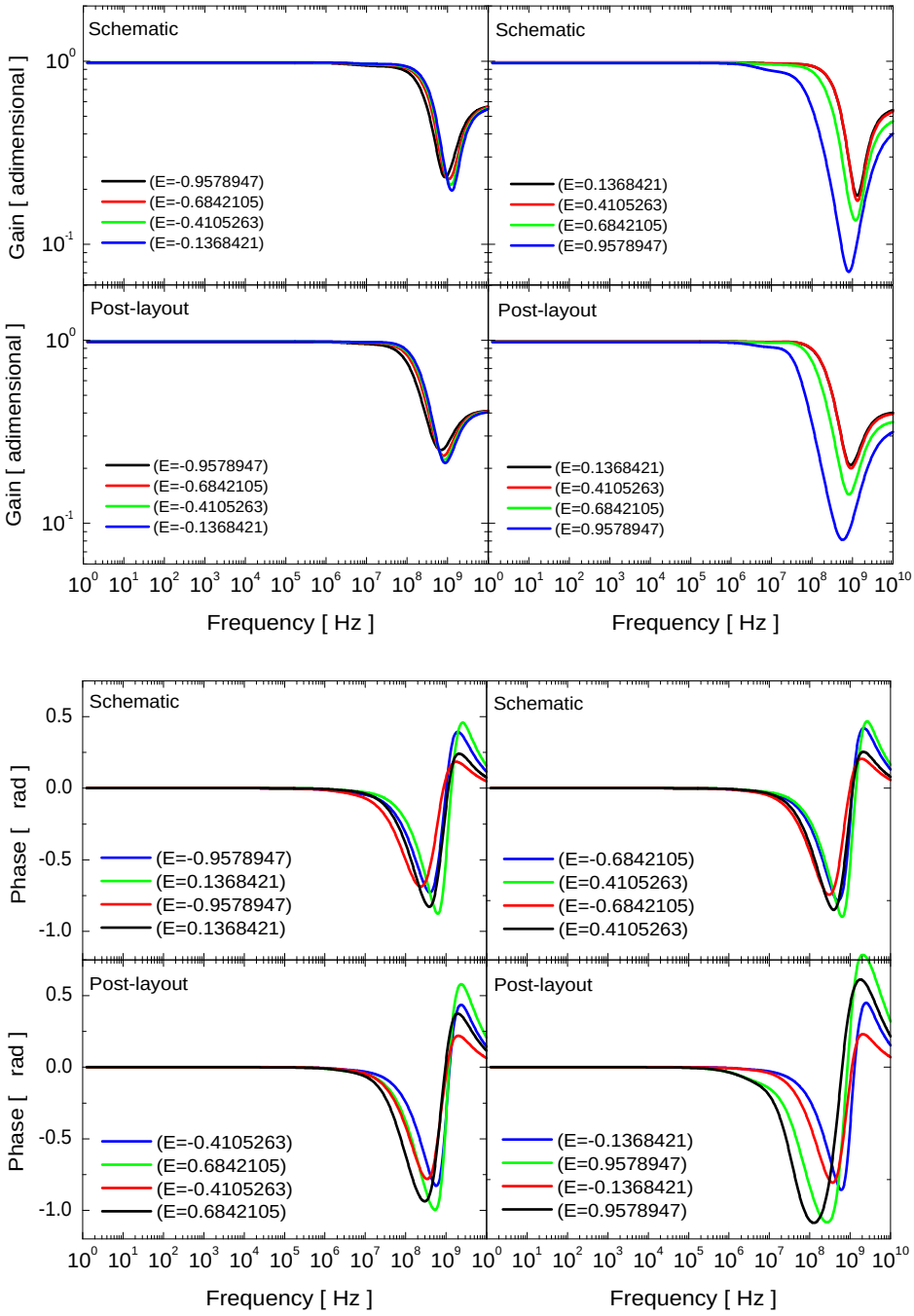

Figure 3.21: Bode diagrams of the output stage (back channel) AC response for different input DC voltages. Top: gain vs frequency. Bottom: phase vs frequency. The E parameter represent the amplitude [V] of the DC generator at the input.

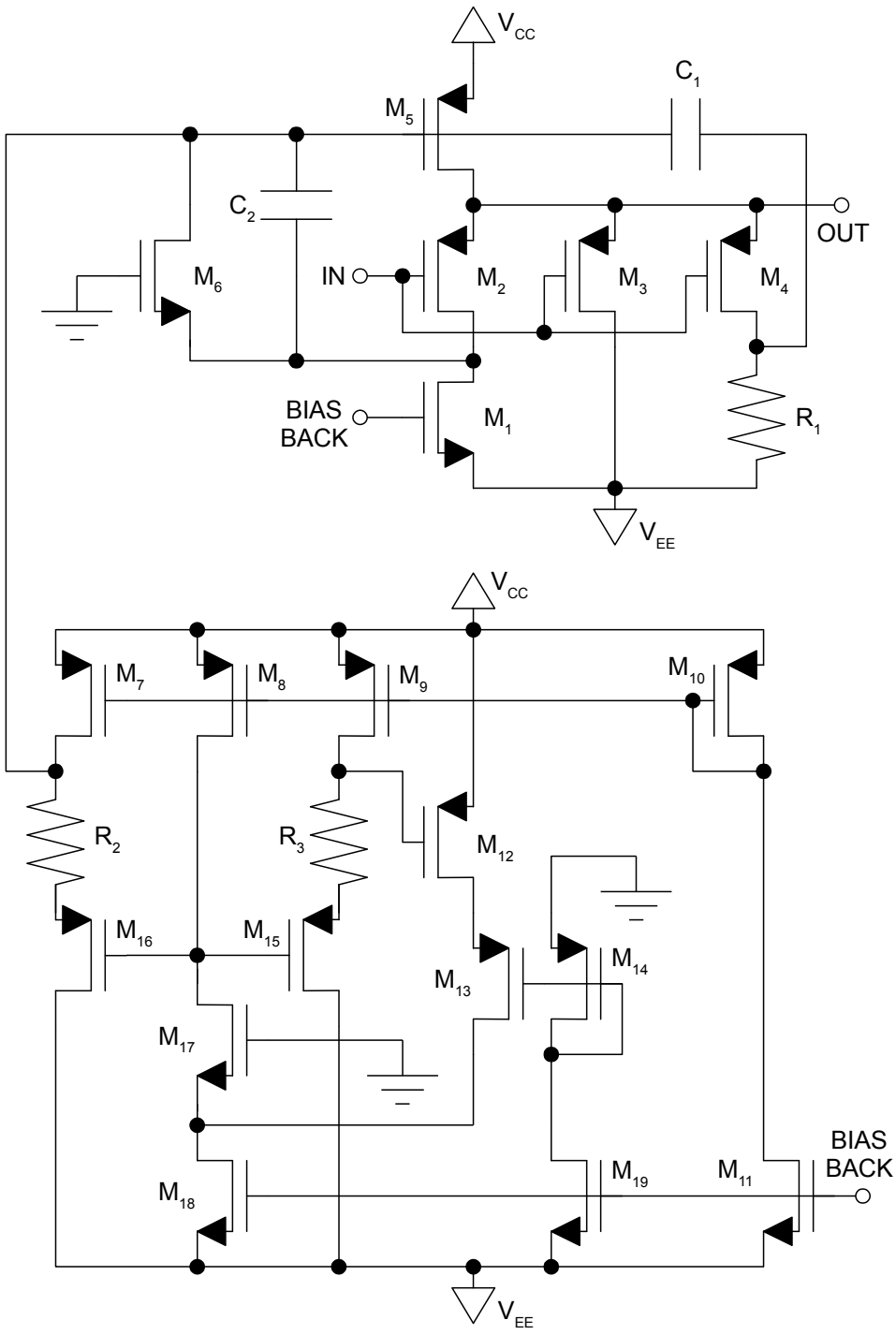

Figure 3.22: Schematic diagram of the output stage of the back channel. The transistor dimensions and other component values are reported in table 3.8.

Table 3.8: Transistor dimensions and component values of the output stage of the back channels. For diagram please refer to figure 3.22.

Transistor	M_1	M_2	M_3	M_4	M_5	M_6	M_7	M_8	M_9	M_{10}
W [µm]	100	600	300	60	800	50	10	10	10	10
L [µm]	3	0.5	0.5	0.5	0.5	0.5	0.5	0.5	0.5	0.5

Transistor	M_{11}	M_{12}	M_{13}	M_{14}	M_{15}	M_{16}	M_{17}	M_{18}	M_{19}
W [µm]	10	80	10	10	50	50	30	30	10
L [µm]	3	0.5	0.5	0.5	0.5	0.5	0.5	3	3

Component	R_1	R_2	R_3	C_1	C_2
Value	10 kΩ	60 kΩ	60 kΩ	3 pF	3 pF

3.6 Charge-sensitive preamplifier: dynamic range, risetime and noise performance

In this section we consider the whole charge-sensitive preamplifier as a single block. We thus connected the input stage to the output stage. This circuit, both in its schematic and post-layout forms, was tested using the test bench in figure 3.23.

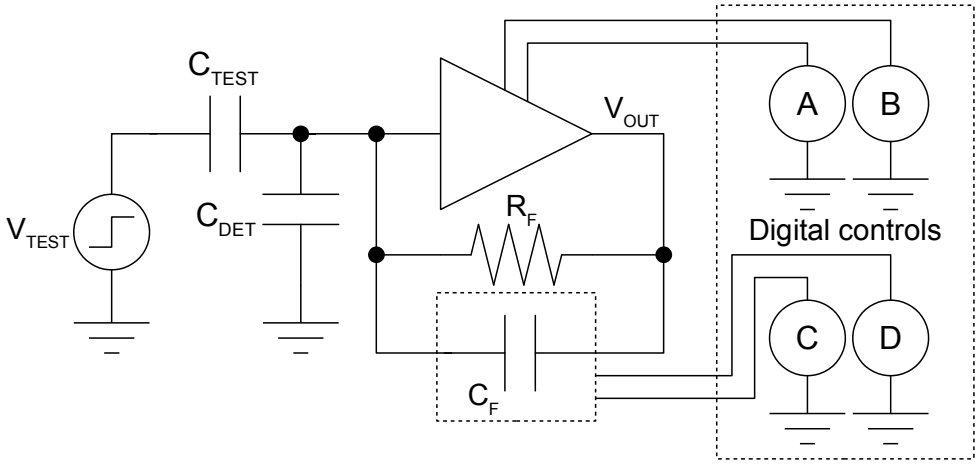

Figure 3.23: Schematic diagram of the test bench used to evaluate the performance of the charge-sensitive preamplifier. C_{TEST} is equal to 1 pF. For the study of the front channel C_{DET} is equal to 4 pF because it emulates the parasitic capacitance of a pad. We studied the behaviour of the back channel for values of C_{DET} equal to 4 pF, 16 pF or 50 pF. The digital slow controls A and B act on the bias current of the input stage of the preamplifier while C and D adjust the integrated feedback capacitance. The available values are 0.2 pF, 0.5 pF, 0.7 pF and 1 pF.

In this test bench the detector capacitance is emulated with the condenser C_{DET}. The current pulses produced by impinging particles or photons on silicon or germanium crystals are almost delta-like. The simulation of delta-like current pulses is not feasible due to practical reasons. The detector was thus simulated with a step-like voltage generator connected to the input of the CSP through a test capacitance C_{TEST}. The amount of charge released by this fictitious detector is equal to the product of the amplitude of the voltage step and C_{TEST}. The first test performed was the analysis of the transient response of the charge-sensitive preamplifier to detector events of different energy. A current pulse produced by 1 MeV event inside a germanium detector is emulated with a test capacitor of 1 pF and a voltage step of 54 mV. In case of a silicon detector the charge

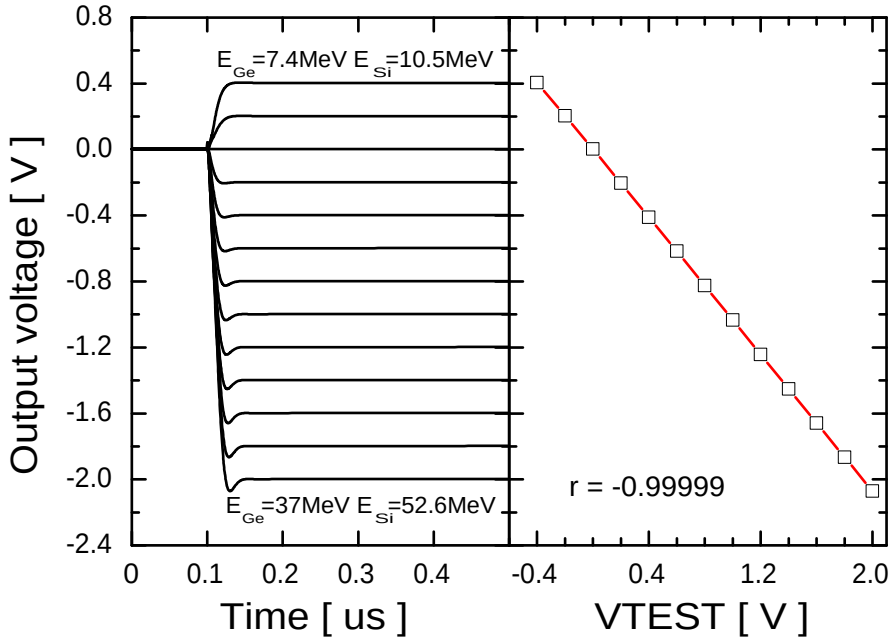

Figure 3.24: Linearity analysis of the front preamplifier. The positive waveforms are produced by electron signals while negative waveforms are produced by hole ones. The r coefficient of the linear regression demonstrates that the linearity is excellent all over the dynamic range. The value of the feedback capacitor in this test is 1 pF.

released by a 1 MeV event is equal to the one released by a test capacitance of 1 pF that undergoes a voltage variation of 38 mV. When the voltage step produced by V_{TEST} is positive it emulates hole signals while when it is negative it emulates electron ones. With 1 pF of feedback capacitance the dynamic range is ≈37 MeV in germanium and ≈52 MeV in silicon (figures 3.24 and 3.34).

The detector capacitance influences directly the CSP open-loop gain. While big detector capacitances tend to slow down the preamplifier response, smaller ones can cause unwanted ringing or even instability. The digital slow control allows to adjust the bandwidth of the preamplifier according to experimental needs. In this way we can optimize the CSP behaviour for different detector capacitances, ensuring the best risetime possible in every condition minimizing the over/undershoot. In figure 3.25 we can see the preamplifier response to 2.63 MeV events (in silicon) with different configurations of the Miller capacitor.

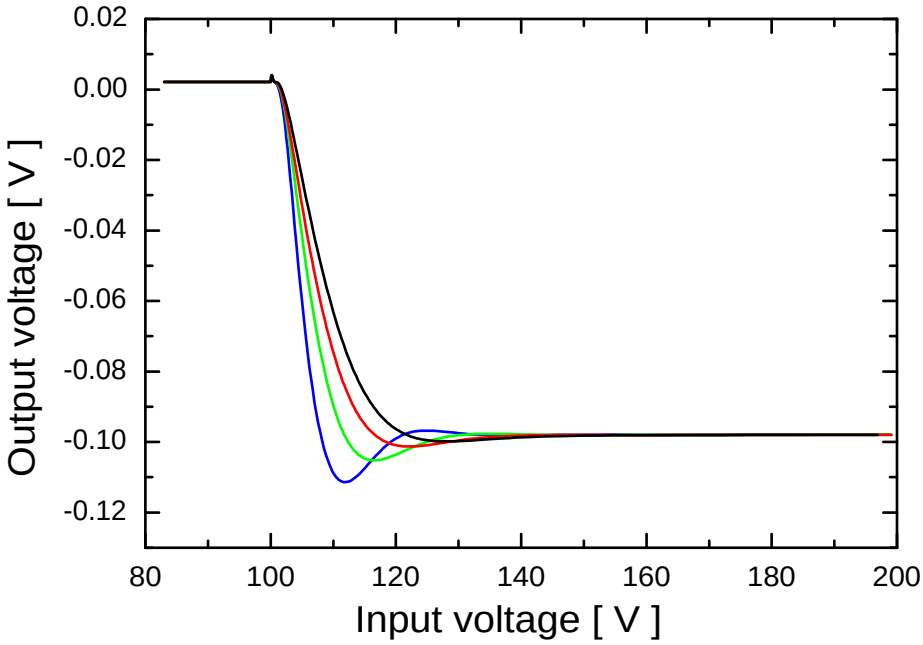

Figure 3.25: Front channel preamplifier response to 2.63 MeV events in silicon. The digital slow control is used to adjust the value of the Miller capacitor C_M. From the faster (blue) signal to the slowest (black) one the selected values of C_M are 2 pF, 3 pF, 4 pF and 5 pF. The detector capacitance C_{DET} is 4 pF.

Table 3.9: Risetime values of the signals in figure 3.25.

C_M [pF]	2	3	4	5
Risetime [ns]	4.8	7.4	10.4	13.3

The feedback capacitance C_F has a major impact on the overall behaviour of the charge-sensitive preamplifier. First of all, it determines the gain of the CSP. With events of the same energy, smaller C_F produce bigger waveforms at the output and vice versa. The feedback capacitance must be taken into account also in the calculation of the open-loop gain of the preamplifier and has big influence on the noise performance. Above all, given the maximum voltage excursion of the operational amplifier output stage, the feedback capacitance determines the dynamic range of the CSP. For all these reasons the possibility to adjust the value of the feedback capacitance is a very useful feature. With the digital slow control we can adjust the value of C_F choosing from the following values: 0.2 pF, 0.5 pF, 0.7 pF and 1 pF. In figure 3.26 we can find the preamplifier response to a 2.63 MeV event in a silicon detector with different values of feedback capacitance.

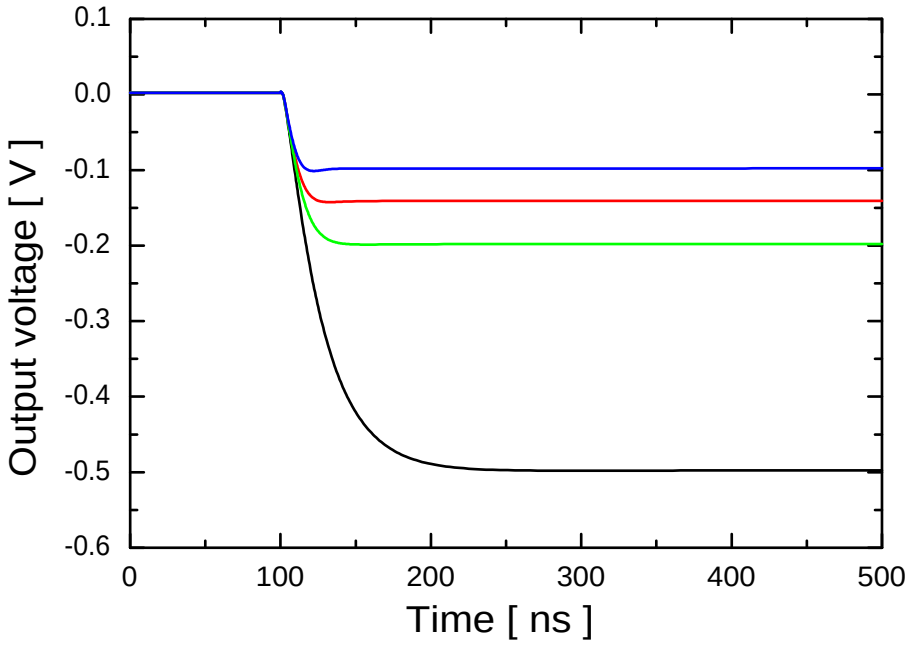

Figure 3.26: Front channel preamplifier response to 2.63 MeV events in silicon. The digital slow control is used to adjust the value of the feedback capacitor C_F. From the bigger (black) signal to the smaller (blue) one the selected values of C_F are 0.2 pF, 0.5 pF, 0.7 pF and 1 pF. The detector capacitance C_{DET} is 4 pF.

Table 3.10: Waveform amplitudes of the signals in figure 3.26

C_F [pF]	0.2	0.5	0.7	1
Amplitude [V]	0.49956	0.19995	0.14284	0.09999

The preamplifier risetime and gain were studied also for the post-layout model of the circuit. In figure 3.27 and in table 3.11 we can find the simulation results for different values of both the feedback capacitor and the Miller one. The simulation data demonstrate that the parasitic capacitances of the layout do not spoil the behaviour of the circuit and have an almost negligible effect on the CSP performance. In figures from 3.28 to 3.31 we can see the results of the AC analysis.

The equivalent rms current noise density at the input of the front channel was evaluated both for the schematic and post-layout model. The chosen detector capacitances are 4 pF and 16 pF. The feedback capacitor value is 1 pF. The results are reported in figures 3.32 and 3.33. The preamplifier performance shows to be in agreement with the experimental requirements of the TRACE detector array.

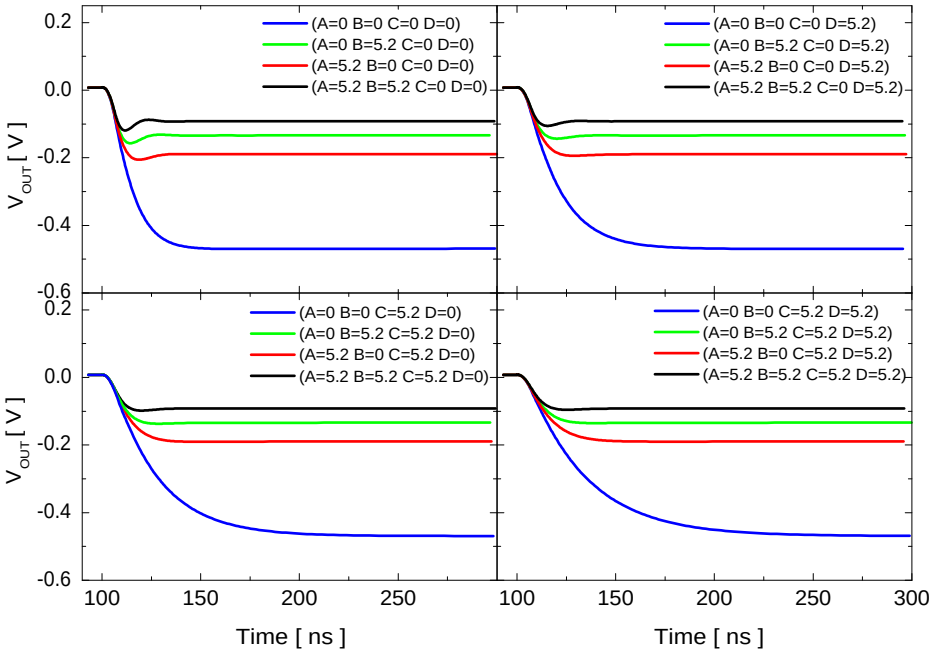

Figure 3.27: Transient simulations (front channel). The test voltage generator emulates a 2.63 MeV event in silicon. The slow controls A and B adjust the feedback capacitor while C and D adjust the Miller capacitor. The detector capacitance is 4 pF. Post-layout simulations.

Table 3.11: Risetime values [ns] of the signals in figure 3.27. The test voltage generator emulates a 2.63 MeV event in silicon. The slow controls A and B [V] adjust the feedback capacitor while C and D [V] adjust the Miller capacitor. The detector capacitance is 4 pF. Post-layout simulations.

(A=0 B=0 C=0 D=0)	(A=0 B=0 C=0 D=5.2)	(A=0 B=0 C=5.2 D=0)	(A=0 B=0 C=5.2 D=5.2)
21.9	36.1	52.0	65.3
(A=0 B=5.2 C=0 D=0)	(A=0 B=5.2 C=0 D=5.2)	(A=0 B=5.2 C=5.2 D=0)	(A=0 B=5.2 C=5.2 D=5.2)
5.6	8.6	12.4	16.2
(A=5.2 B=0 C=0 D=0)	(A=5.2 B=0 C=0 D=5.2)	(A=5.2 B=0 C=5.2 D=0)	(A=5.2 B=0 C=5.2 D=5.2)
8.0	12.3	18.7	24.2
(A=5.2 B=5.2 C=0 D=0)	(A=5.2 B=5.2 C=0 D=5.2)	(A=5.2 B=5.2 C=5.2 D=0)	(A=5.2 B=5.2 C=5.2 D=5.2)
4.6	6.4	8.8	11.2

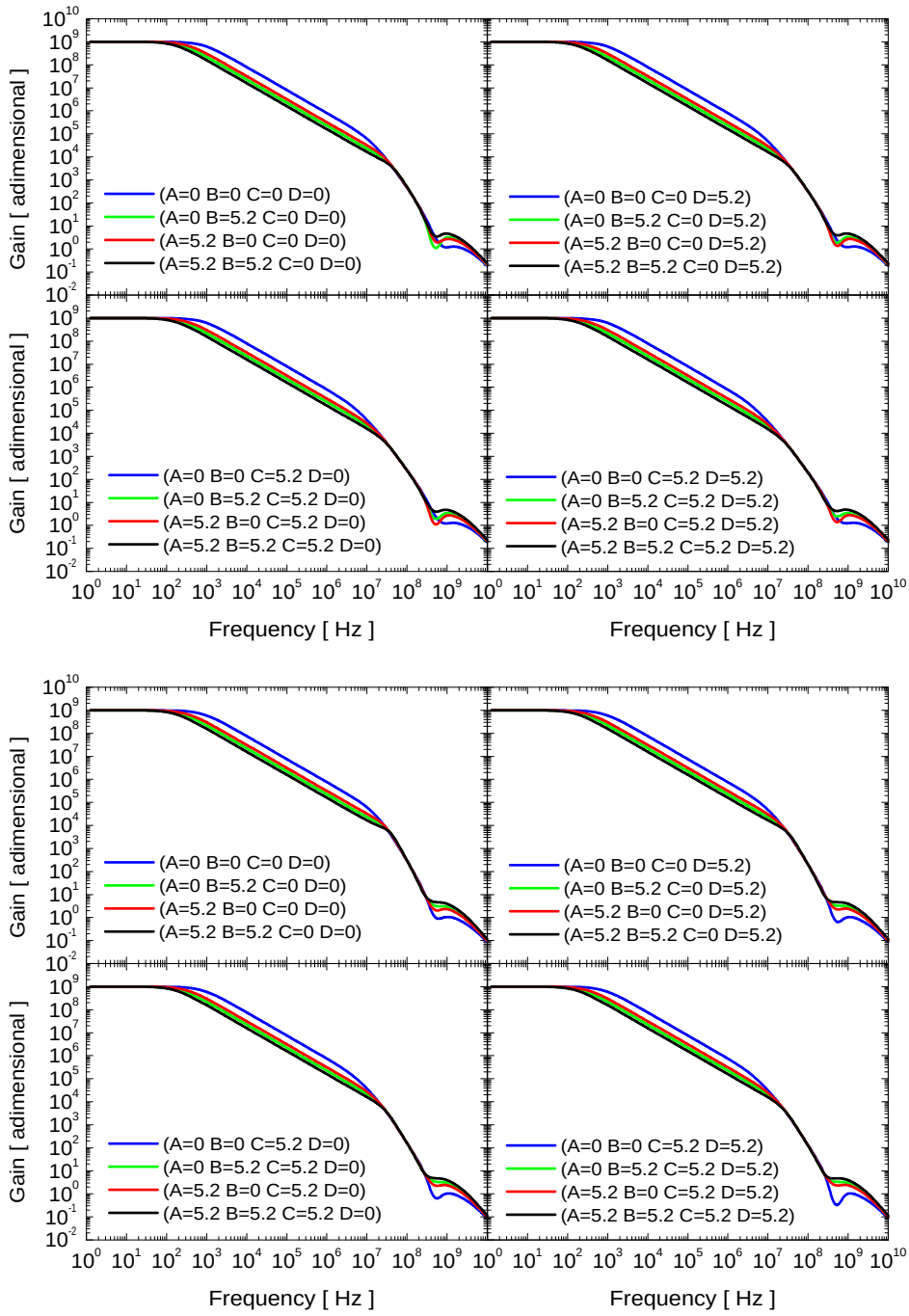

Figure 3.28: Bode diagram of the front channel (Gain versus frequency). Top: schematic simulation. Bottom: post-layout simulation. The detector capacitance is 4 pF.

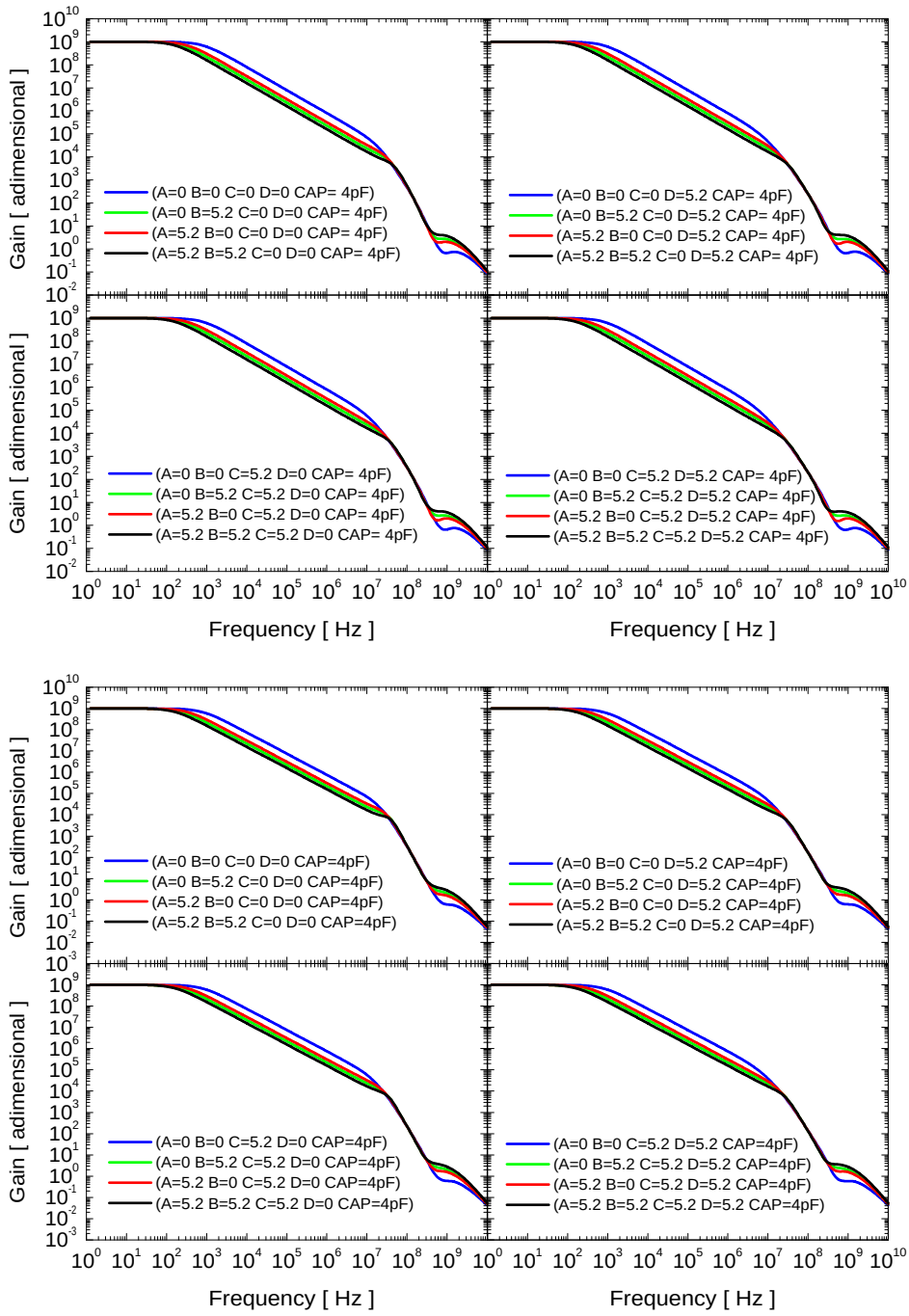

Figure 3.29: Bode diagram of the back channel (Gain versus frequency). Top: schematic simulation. Bottom: post-layout simulation. The detector capacitance is 4 pF.

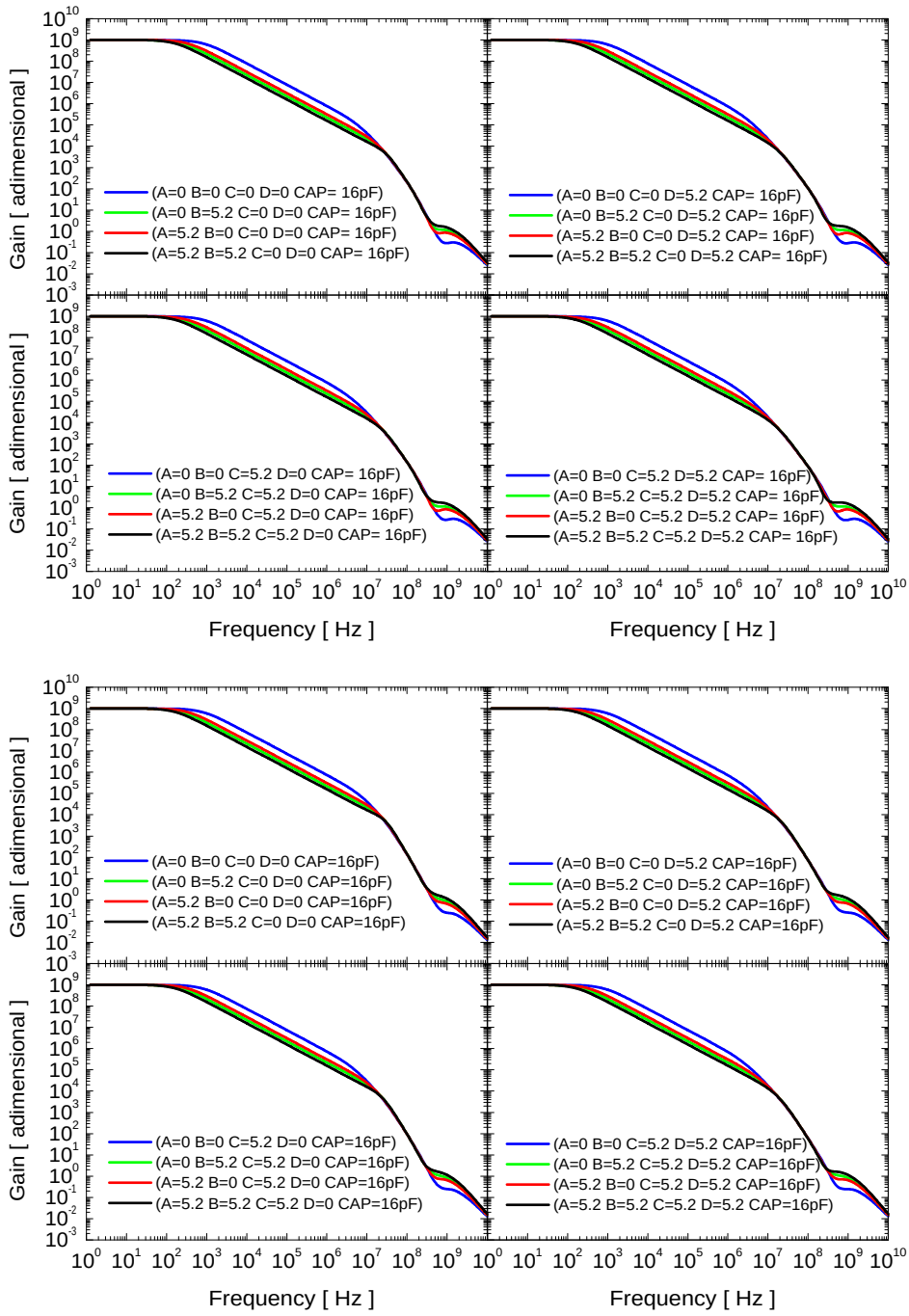

Figure 3.30: Bode diagram of the back channel (Gain versus frequency). Top: schematic simulation. Bottom: post-layout simulation. The detector capacitance is 16 pF.

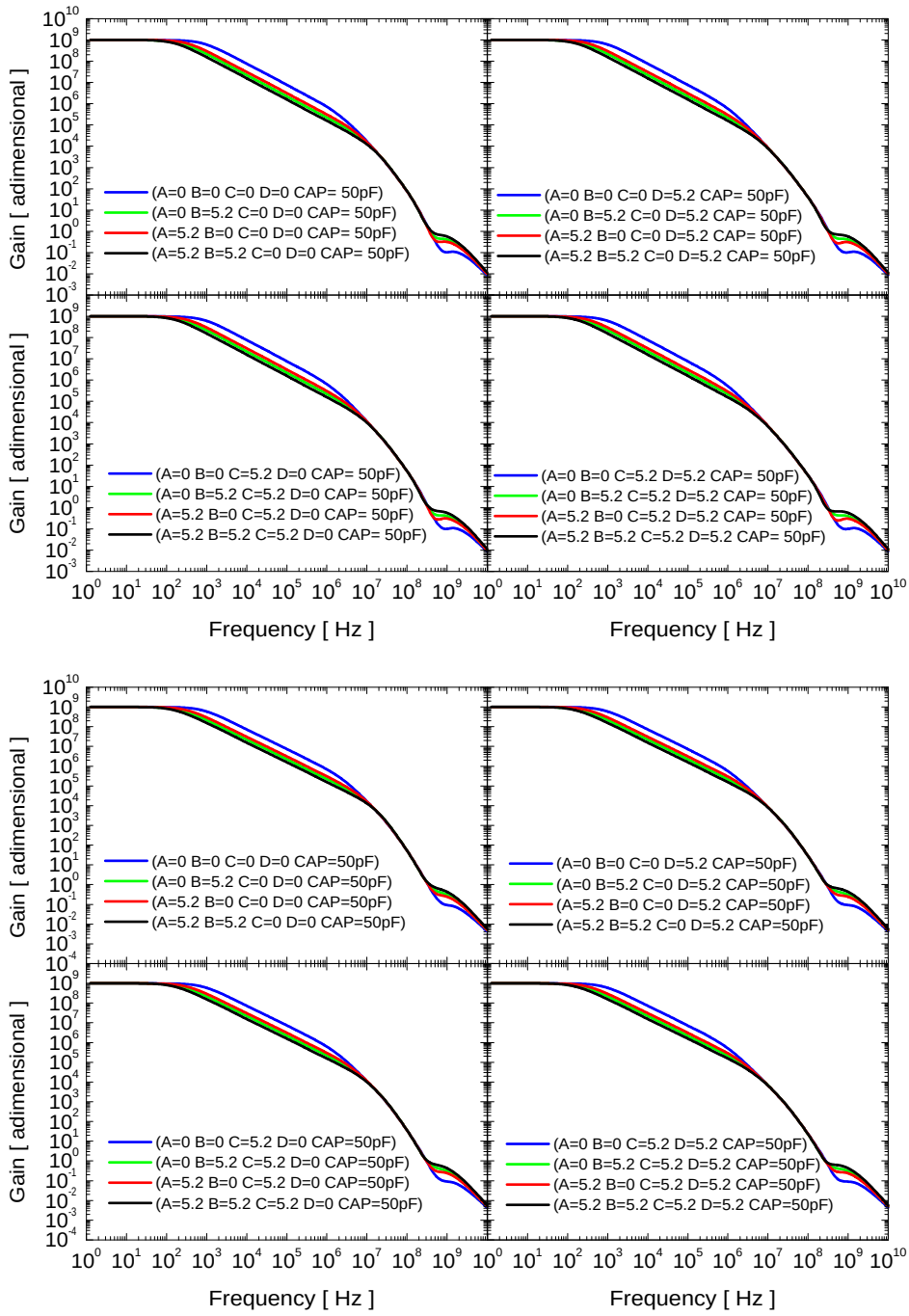

Figure 3.31: Bode diagram of the back channel (Gain versus frequency). Top: schematic simulation. Bottom: post-layout simulation. The detector capacitance is 50 pF.

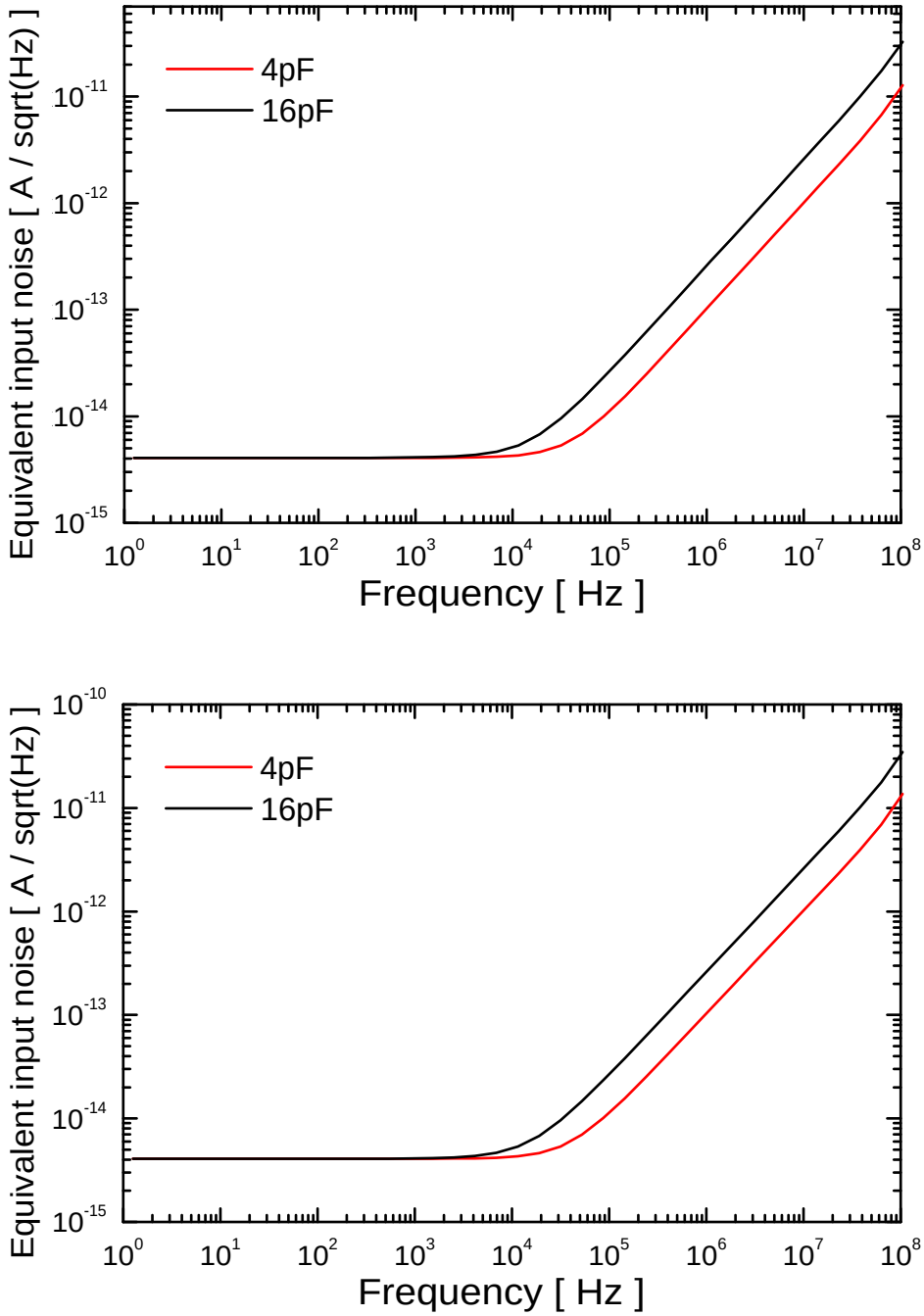

Figure 3.32: The equivalent rms current noise density at the input of the front channel. The chosen detector capacitances are 4 pF and 16 pF. The feedback capacitor value is 1 pF. Top: results obtained with the schematic model. Bottom: results obtained with the post-layout model.

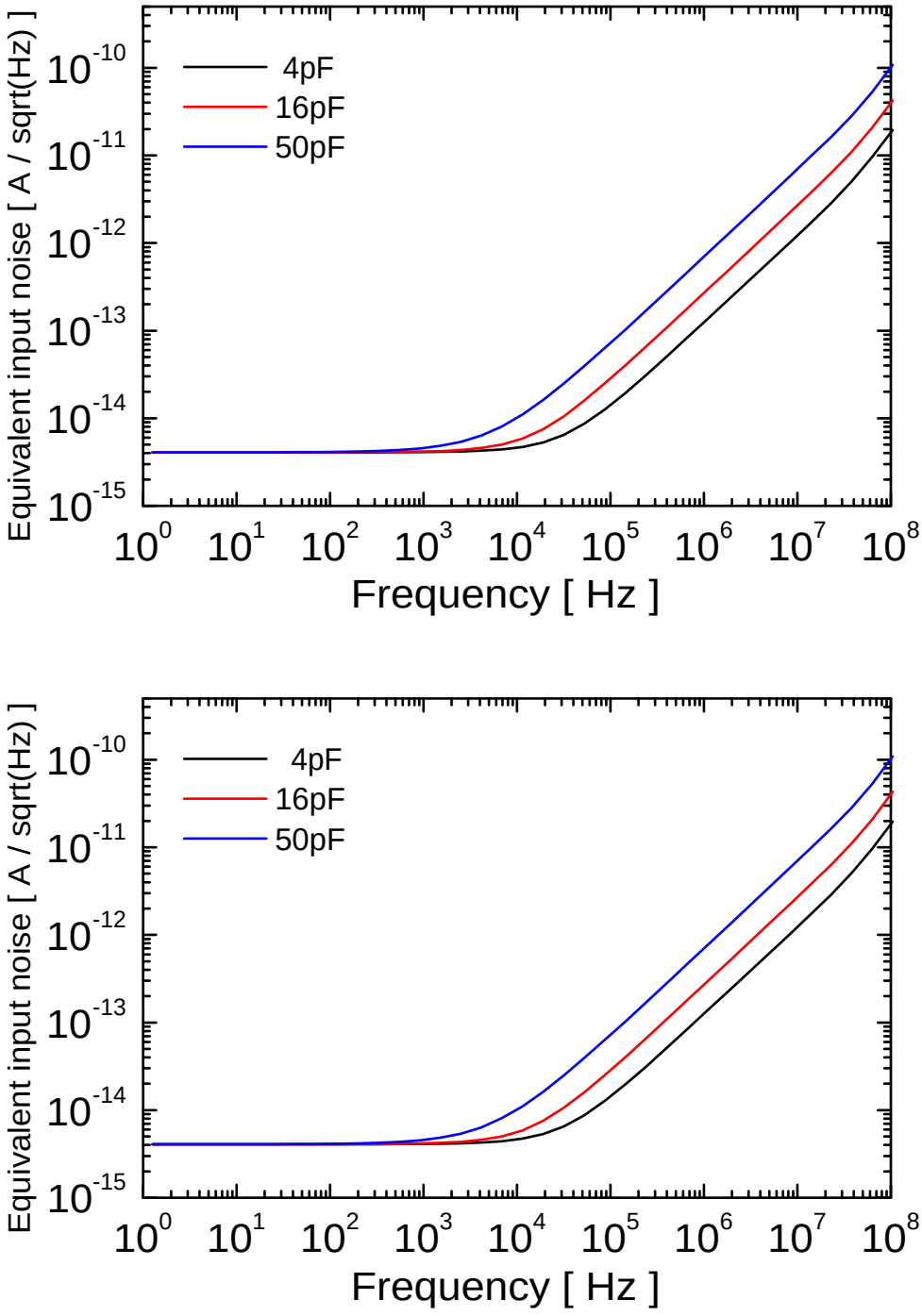

Figure 3.33: The equivalent rms current noise density at the input of the back channel. The chosen detector capacitances are 4 pF, 16 pF and 50 pF. The feedback capacitor value is 1 pF. Top: results obtained with the schematic model. Bottom: results obtained with the post-layout model.

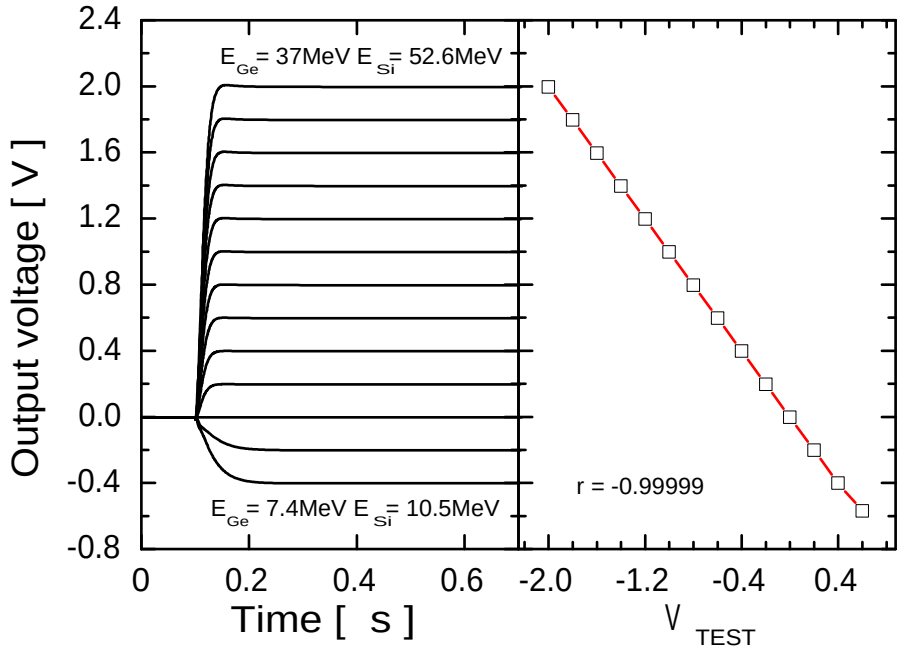

Figure 3.34: Linearity analysis of the back preamplifier. The positive waveforms are produced by electron signals while negative waveforms are produced by hole ones. The r coefficient of the linear regression demonstrates that the linearity is excellent all over the dynamic range. The value of the feedback capacitor in this test is 1 pF.

Table 3.12: White spectral noise density at the input at low frequency and corner frequency of both front and back channels for different detector capacitances.

	White noise	Noise corner frequency [Hz]		
	$[A^2/Hz]$	4pF	16pF	50pF
Front - schematic	1.66E-29	39845	15714	-
Front - post layout	1.66E-29	39419	15659	-
Back - schematic	1.66E-29	32814	15128	5834
Back - post layout	1.66E-29	32650	15197	5874

3.7 The comparator and current sink

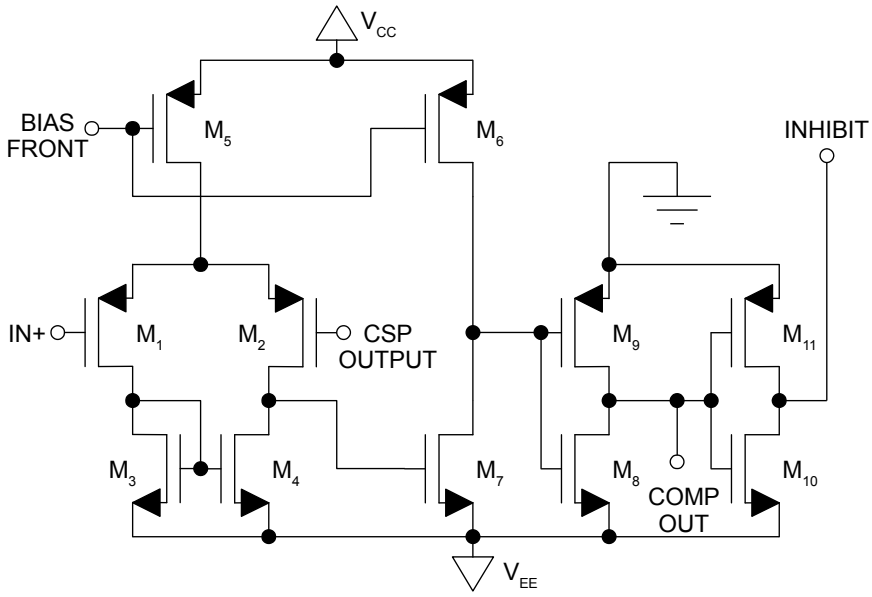

Transistor	M_1	M_2	M_3	M_4	M_5	M_6
W [μm]	10	10	10	10	10	10
L [μm]	0.5	0.5	1	1	2	0.5

Transistor	M_7	M_8	M_9	M_{10}	M_{11}
W [μm]	10	10	60	10	60
L [μm]	0.5	0.5	0.5	0.5	0.5

Figure 3.35: Schematic diagram of the comparator of front channel.

When a high-energy event saturates the output stage of the CSP the output signal becomes distorted and loses all its information. This does not mean that the information of the event energy is lost. In fact the charge released by the detector is not lost at all: it is just deposited on the capacitance of the input node. The fast-reset technique, in case of saturation, measures directly the charge deposited on the input node. The collection of the charge is operated by a precise and constant current generator. When the output voltage of the preamplifier becomes 0 V the fast-reset procedure ends. All the charge on the input node has been collected and the preamplifier is ready to work in normal conditions again. Since the reset speed is $\approx 10\ \frac{\text{MeV}}{\mu\text{s}}$ the dead time is greatly reduced. The

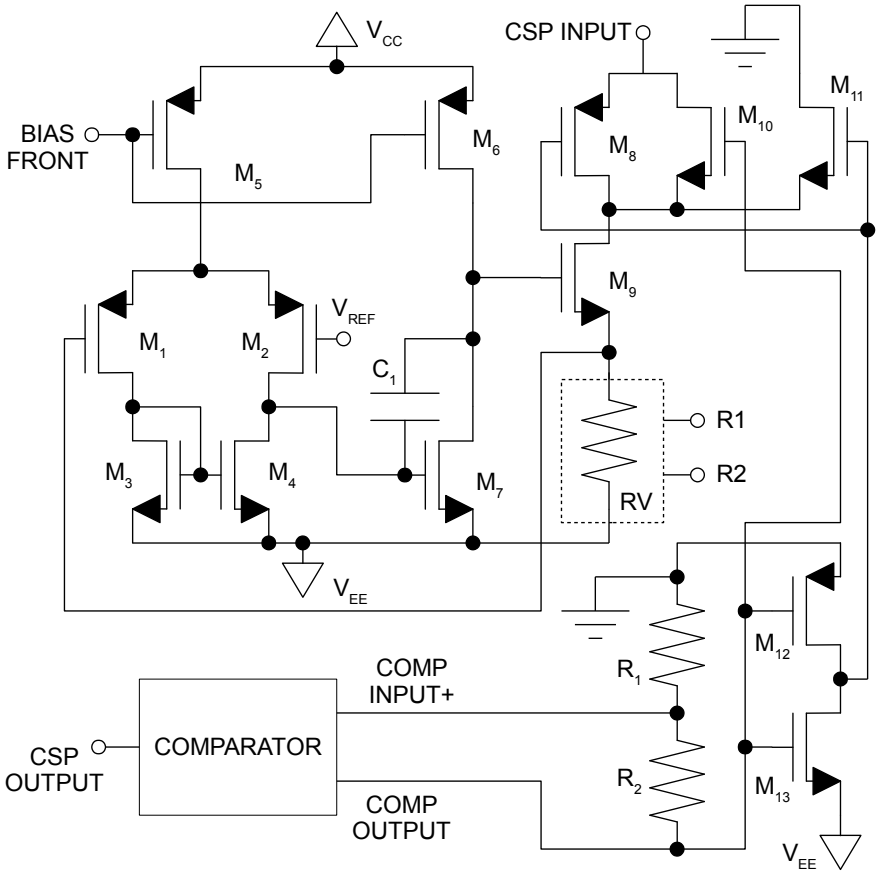

The resistance RV can be adjusted with the controls R1 and R2 and can assume the following values: 1.5 MΩ, 2.1 MΩ, 2.4 MΩ and 3 MΩ.

Transistor	M_1	M_2	M_3	M_4	M_5	M_6	M_7
W [μm]	10	10	10	10	10	10	37.5
L [μm]	0.5	0.5	1	1	2	2	0.5

Transistor	M_8	M_9	M_{10}	M_{11}	M_{12}	M_{13}
W [μm]	2	150	1	1	5	2.5
L [μm]	0.5	0.5	0.5	0.5	0.5	0.5

Component	R_1	R_2	C_1
value	24k	6k	1.4 pF

Figure 3.36: Schematic diagram of the current sink of front channel.

duration of the reset procedure is directly proportional to the amount of charge collected. In this way we can perform high-resolution spectroscopy even if the preamplifier is in deep saturation condition. The fast-reset device is made, as previously described, of two elementary blocks. The first one is the comparator and the second is the current sink. The comparator is a fast non-compensated operational amplifier: for the schematic diagram please refer to figures 3.35 and 3.41. M_8 and M_9 constitute an inverter that buffers the output and acts as a level shifter. In this way the output of the comparator swings between ground and V_{CC}. The negated value of the output, called INHIBIT, is buffered by the inverter M_{10} and M_{11}. The current sink is a compensated operational amplifier that is used to generate a precise and constant current: for the schematic diagram please refer to figures 3.36 and 3.42. The feedback loop on the gate of M_1 ensures that the voltage applied to the resistance RV is constant and equal to $V_{CC} - V_{REF}$. RV is an adjustable resistance that can assume the following values: 1.5 MΩ, 2.1 MΩ, 2.4 MΩ and 3 MΩ. The current that flows through RV is collected by M_9. In normal conditions this current is sent to ground through M_{11} because the transmission gate M_8-M_{10} is closed. When the comparator, configured as a Schmitt trigger, recognises that the output voltage of the preamplifier crosses the threshold of saturation (determined by R_1 and R_2) it opens the transmission gate M_8-M_{10} and shuts off M_{11}. In this way the current generated flows to the input node. When the output voltage of the CSP reaches the 0 V level the comparator triggers again, closes the transmission gate and the current generated by RV flows again through M_{11}. The inverter M_{12}-M_{13} is used to drive the transmission gate. The quality of the current generator is the key point of the fast-reset technique effectiveness. Using the same test bench pictured in figure 3.23 we evaluate the performance of the fast-reset device. The step-like voltage generator V_{TEST} is used to simulate events inside the detector with energy higher than the saturation limit of the CSP. We thus measure with a simple algorithm the length of the comparator signals. Since the duration of the fast-reset procedure is directly proportional to the energy of the event that caused saturation, we are interested in evaluating the linearity of this parameter across a wide energy range. In figures 3.37 and 3.39 we can see both the CSP output waveforms and the comparator signals during reset processes of different duration. Since the reset current is generated by an adjustable resistance, the reset procedure can assume different speeds. In figures 3.38 and 3.40 we plotted the reset durations vs the energy of the event for different reset speeds. The fast-reset device shows to be excellently linear in the tested energy range.

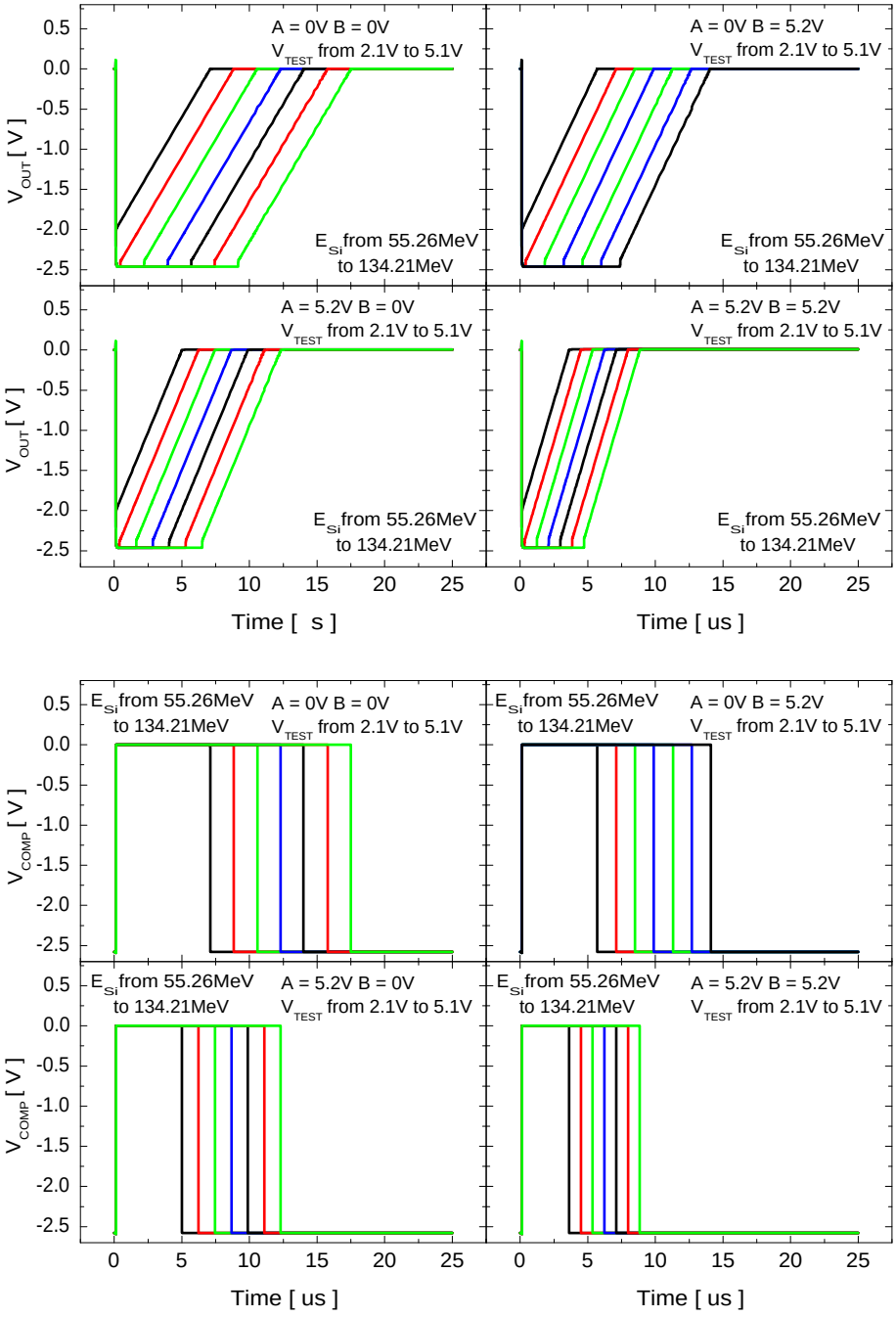

Figure 3.37: Top: preamplifier output signals (front channel) during fast-reset procedures for energies from 55.26 MeV to 134.21 MeV. Bottom: comparator output signals during fast-reset procedures for energies from 55.26 MeV to 134.21 MeV. The digital slow-controls A and B are used here to adjust the value of RV and thus the reset speed.

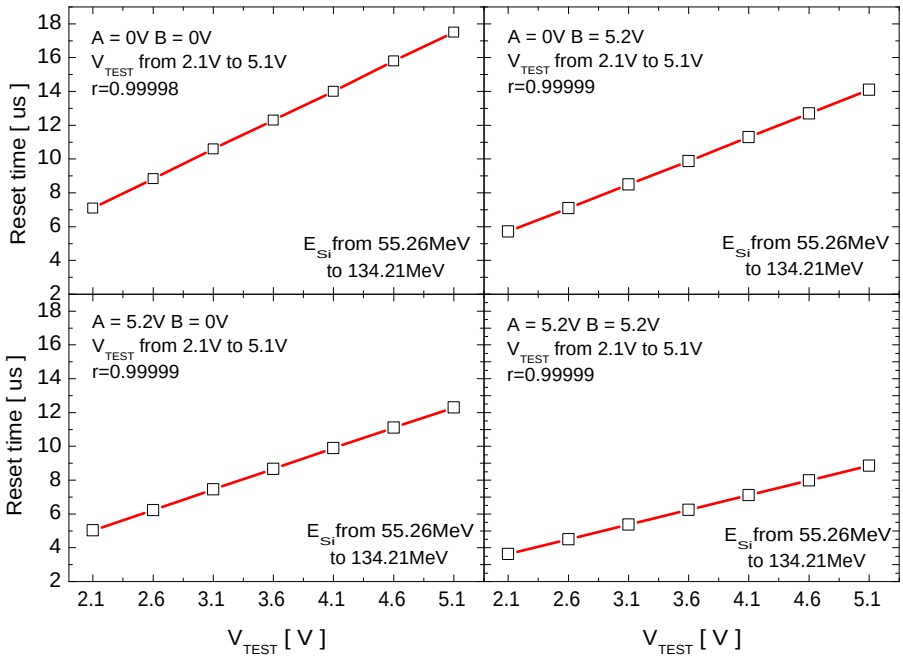

Figure 3.38: Durations of the reset procedures depicted in figure 3.37. The digital slow-controls A and B are used here to adjust the value of RV and thus the reset speed. The r coefficient of the linear regression demonstrates that the reset duration is very linear respect to the event energy.

Table 3.13: Reset speeds for different slow-control configuration calculated from the data in figure 3.38.

Slow-control configuration [V]	(A=0 B=0)	A=0 B=5.2)	(A=5.2 B=0)	(A=5.2 B=5.2)
Reset speed [MeV/µs]	7.7	9.5	10.9	15.1

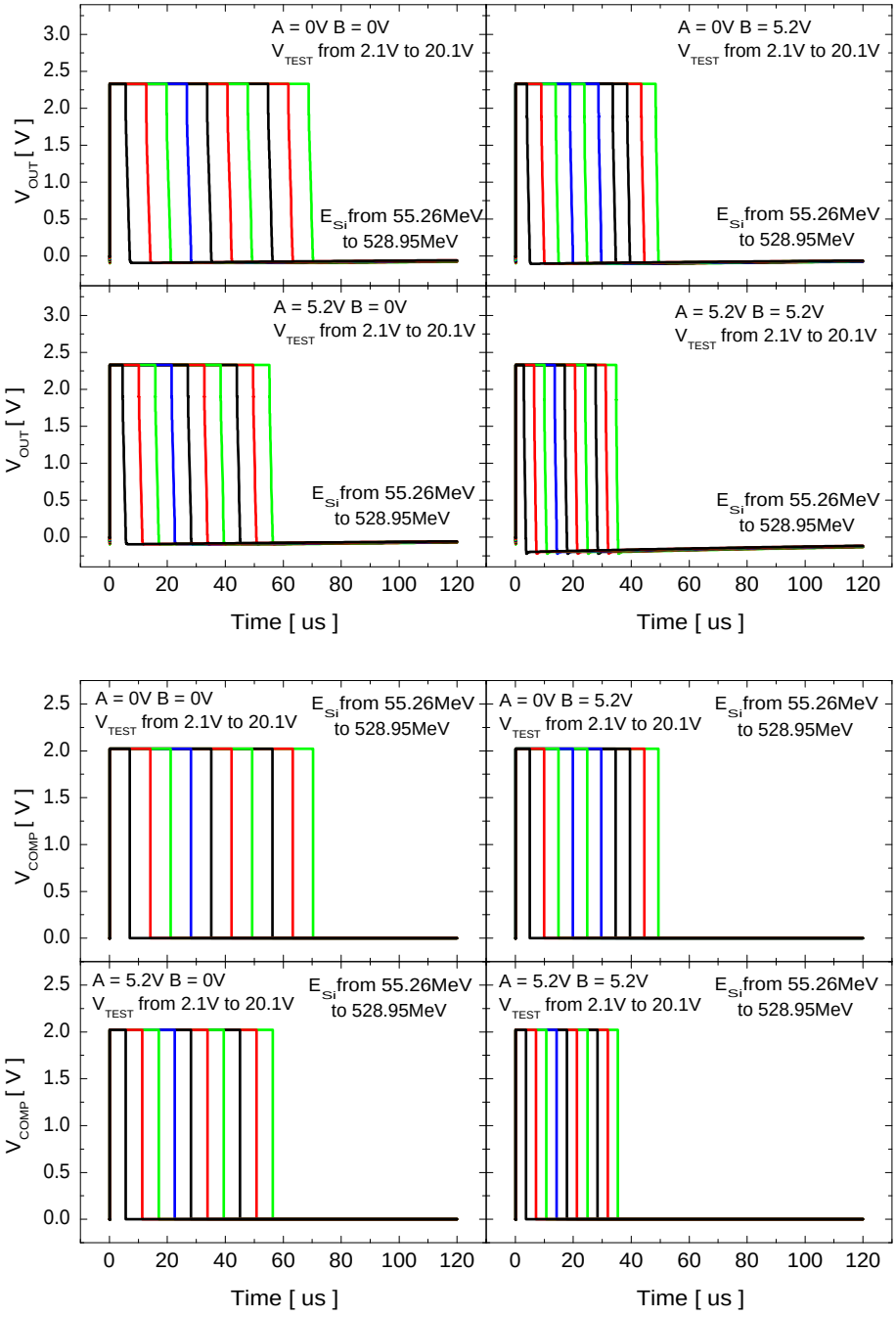

Figure 3.39: Top: preamplifier output signals (back channel) during fast-reset procedures for energies from 55.3 MeV to 529 MeV. Bottom: comparator output signals during fast-reset procedures for energies from 55.3 MeV to 529 MeV. The digital slow-controls A and B are used here to adjust the value of RV and thus the reset speed.

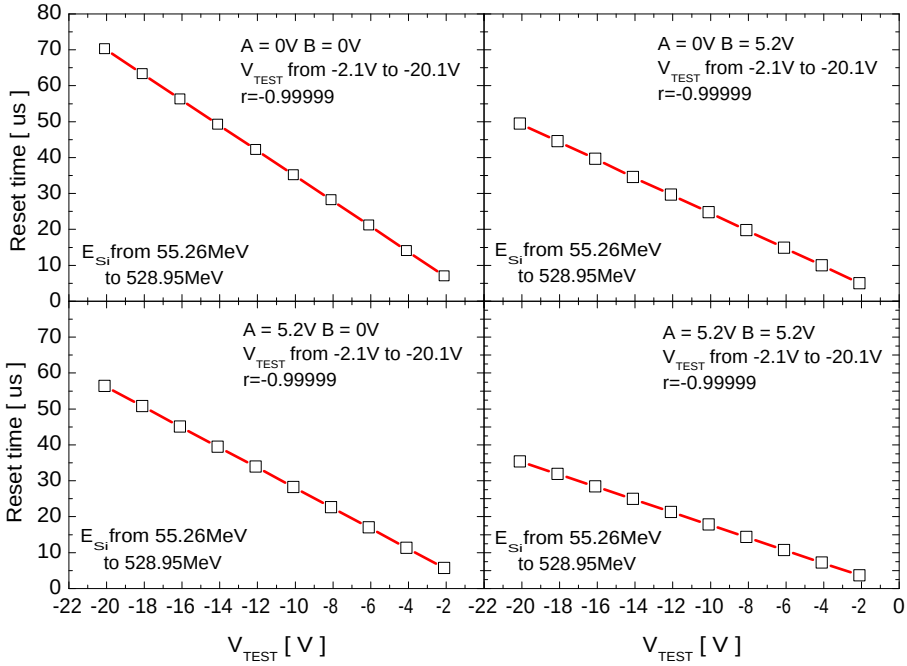

Figure 3.40: Durations of the reset procedures depicted in figure 3.39. The digital slow-controls A and B are used here to adjust the value of RV and thus the reset speed. The r coefficient of the linear regression demonstrates that the reset duration is very linear respect to the event energy.

Table 3.14: Reset speeds for different slow-control configuration calculated from the data in figure 3.40.

Slow-control configuration [V]	(A=0 B=0)	A=0 B=5.2)	(A=5.2 B=0)	(A=5.2 B=5.2)
Reset speed [MeV/µs]	7.5	9.3	10.7	14.9

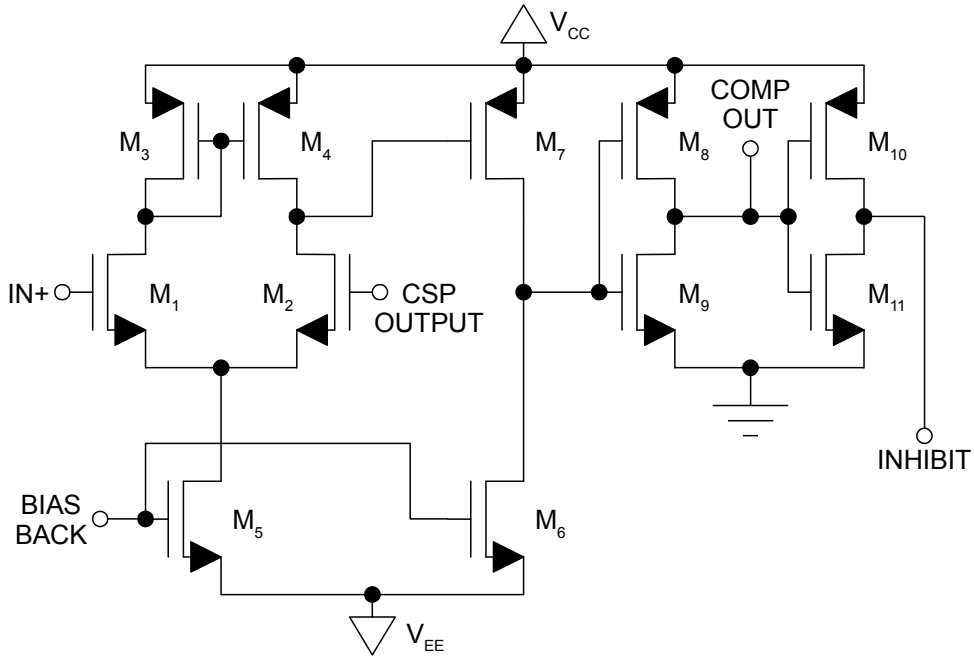

Transistor	M_1	M_2	M_3	M_4	M_5	M_6
W [μm]	10	10	10	10	50	10
L [μm]	0.5	0.5	0.5	0.5	1.5	0.5

Transistor	M_7	M_8	M_9	M_{10}	M_{11}
W [μm]	40	60	10	300	150
L [μm]	0.5	0.5	0.5	0.35	0.35

Figure 3.41: Schematic diagram of the comparator of the back channel.

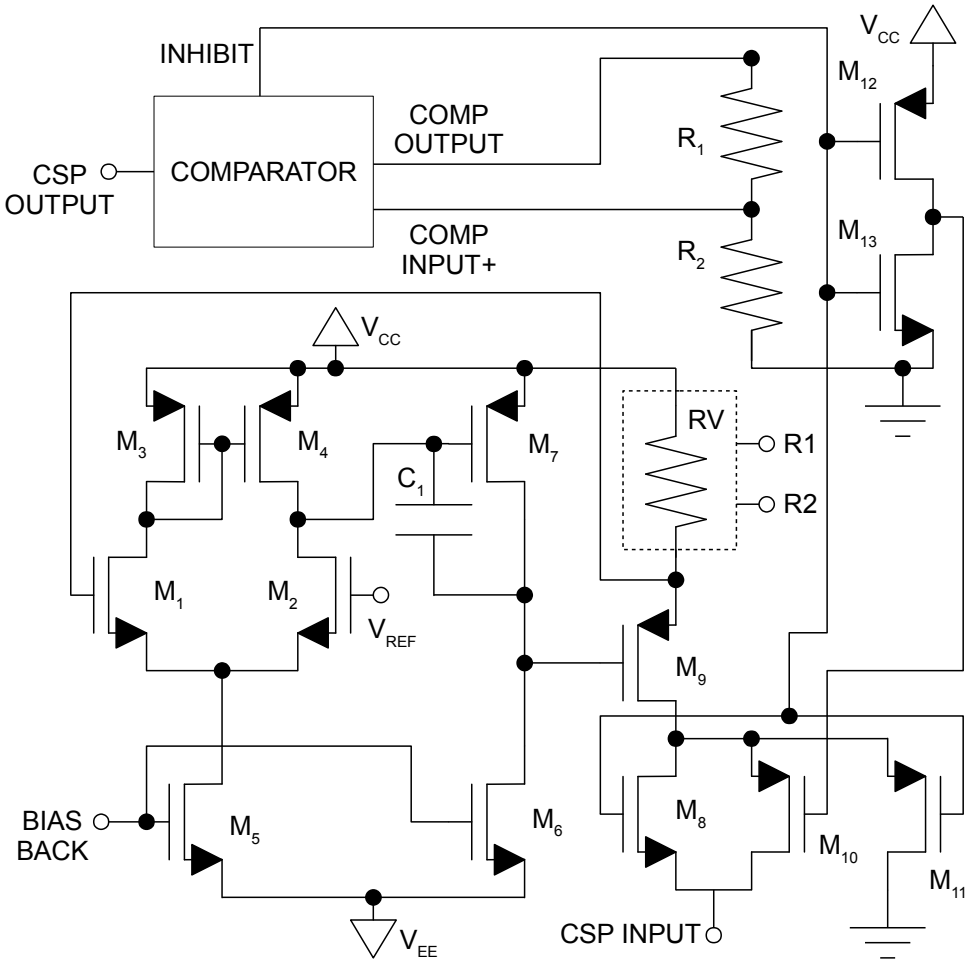

The resistance RV can be adjusted with the controls R1 and R2 and can assume the following values: 1.5 MΩ, 2.1 MΩ, 2.4 MΩ and 3 MΩ.

Transistor	M_1	M_2	M_3	M_4	M_5	M_6	M_7
W [μm]	10	10	10	10	60	10	150
L [μm]	0.5	0.5	0.5	0.5	2	0.5	0.5

Transistor	M_8	M_9	M_{10}	M_{11}	M_{12}	M_{13}
W [μm]	2	150	1	2	5	2.5
L [μm]	0.5	0.5	0.5	0.5	0.5	0.5

Component	R_1	R_2	C_1
value	24k	6k	1.4 pF

Figure 3.42: Schematic diagram of the current sink of back channel.

3.8 The I²C engine

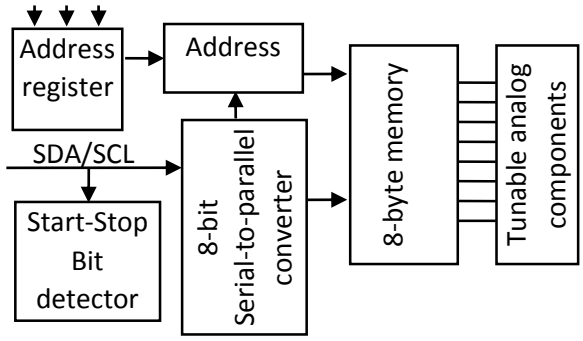

Figure 3.43: Building blocks of the I²C receiver. The address register is connected to three physical pins of the chip.

One of the most relevant features of the ASIC CSP is the possibility to adjust some critical parameters via slow control through a simple digital I²C interface. This is very useful for real time circuit optimization. Such feature makes the ASIC very flexible and suited to be used in conjunction with different detectors. The I²C engine is used to connect or disconnect analog components so as to adjust the most relevant circuit parameters. For the block diagram of the I²C engine please refer to figure 3.43 The state of three physical pins sets the I²C address of the chip. The digital data stream runs on two open collector lines, named SCL and SDA (figure 3.45). While the first carries the clock, the second carries the real information. When the system recognizes an I²C "start" condition, the FIFO undergoes reset. The data bits are fed one by one into the FIFO, which acts as a serial to parallel converter. The sequence obtained is checked against the address register. If the result is positive, the FIFO starts to store the second byte, which is used to determine which RAM channels will be programmed. The third byte contains the information about the desired electrical configuration. The channels can be programmed in group: just one or all together in a single shot. When the information is stored inside the static RAM, the corresponding digital lines are propagated across all the chip and used to trigger some transmission gates which connect or disconnect analog components inside the circuitry. The parameters that can be controlled are the value of the feedback capacitor, the current of the Fast Reset current sink, the value of the Miller compensation cap and the bias current of the input stage. The first one determines the gain of the preamplifier and has great impact on speed and noise. The second one

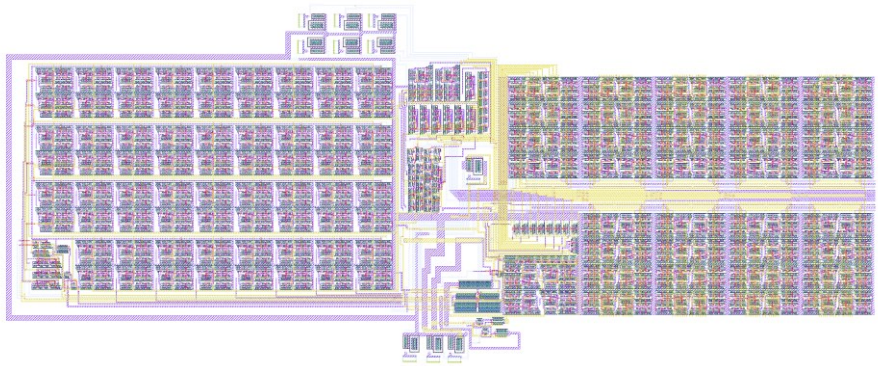

Figure 3.44: Layout of the I^2C engine. It is approximately 500µm wide and 1.5mm long. On the left we can see the FIFO while on the right the SRAM cells.

determines the speed of the reset process. The third one is used to control the bandwidth of the preamplifier and the last one is intended to reduce the transconductance of the input stage in particular conditions such as in cryogenic applications. The possibility to tune the bandwidth across a decade is really useful and gives great flexibility to the ASIC which can work with optimal trade-off between speed and ringing with very different detector capacitances. This means that the same preamplifier can be connected to Silicon Pads or Strips or even Germanium Detectors achieving the best performance possible without any circuit modification. The layout of the I^2C engine is reported in figure 3.44

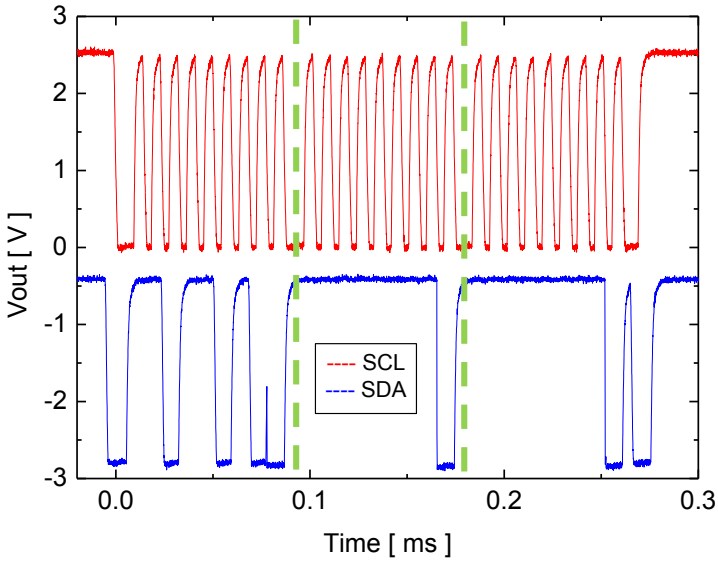

Figure 3.45: Example of I²C communication between a microcontroller and the ASIC preamplifier. The microcontroller is sending a simple programming instruction to the chip. The dashed green lines separate the three transmitted bytes. The first one contains the address of the chip, the second indicates the channels to be programmed and the third contains the desired electrical configuration. The signal in red is called SCL and carries the clock while the informations are carried by the blue signal called SDA. Signal captured with a digital scope.

Chapter 4

Experimental results

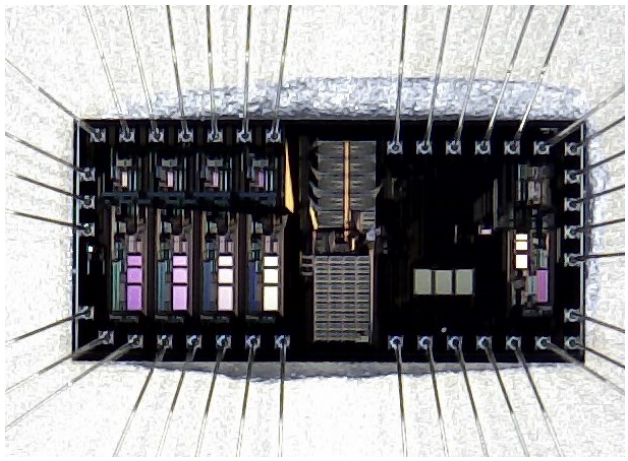

Figure 4.1: Photograph of the 3.3 mm x 1.5 mm chip wire-bonded in the cavity of a PLCC44 carrier. This image was taken with a magnifying camera connected to a PC through USB communication. The four blocks on the left are the hole channels, the block on the right is the electron one and the structure in the middle is the I^2C engine.

The chip was submitted to the foundry at the end of July 2014 and was received in October of the same year. In figure 4.1 we can see the die glued and wire-bonded on a PLCC44 carrier. Extensive tests have been performed both on single chips and on small arrays. The circuit characterization was performed on a test bench. The detector was simulated with a pulser and a test capacitance. We also designed and realized a preamplifier board with eight ASICs for a total of 32 channels. We connected it to a real detector and acquired the spectrum of an alpha source. In this chapter we will briefly summarize the results obtained.

4.1 Functionality test of the I²C engine

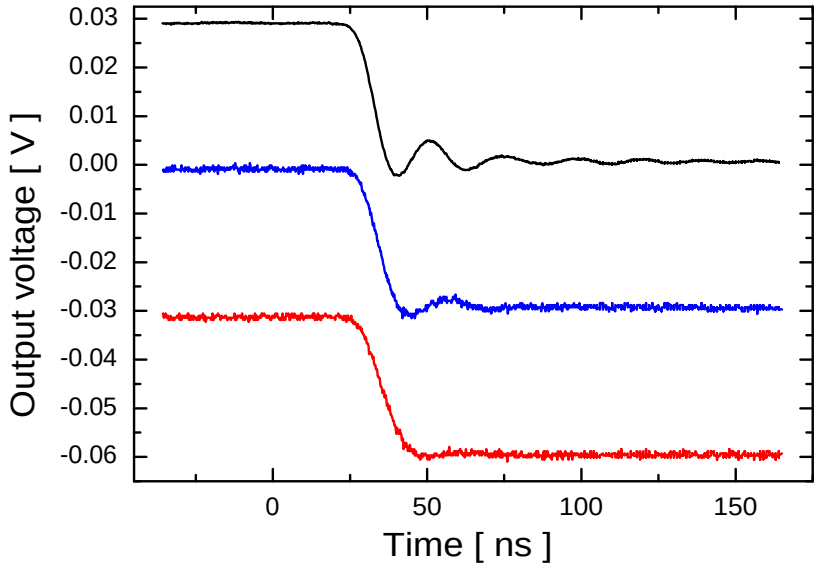

C_M	3 pF	4 pF	5 pF
Risetime [ns]	9.5	11.5	15.2

Figure 4.2: CSP output waveforms obtained with the same test pulse (1.57 MeV in silicon) but with three different bandwidth configurations. The black signal is too fast for a 4 pF detector capacitance and shows ringing. The red one instead is a good trade off between speed and ringing.

We designed and realized a small PCB on which we fitted a SMD PLCC44 socket for the ASIC, the feedback resistances and both the test and detector capacitors for all the channels of the chip. The power supplies were properly filtered in order to reduce noise and cross-talk between channels. We chose a PTFE (Polytetrafluoroethylene, also known as Teflon) substrate for the PCB because of its good noise performance and low dielectric loss. The PCB tracks were engraved with a CNC milling machine. We programmed the I²C master on an open-source microcontroller. Since the digital engine of the chip works between ground and V_{CC} (which is equal to 2.5 V-2.6 V) an I²C level shifter was necessary in order to connect the 5 V microcontroller to the ASIC without damage. We simulated some events with the pulser and recorded on a digital scope the output waveform of the preamplifier. In doing so we adjusted the electrical parameters of the CSP with the

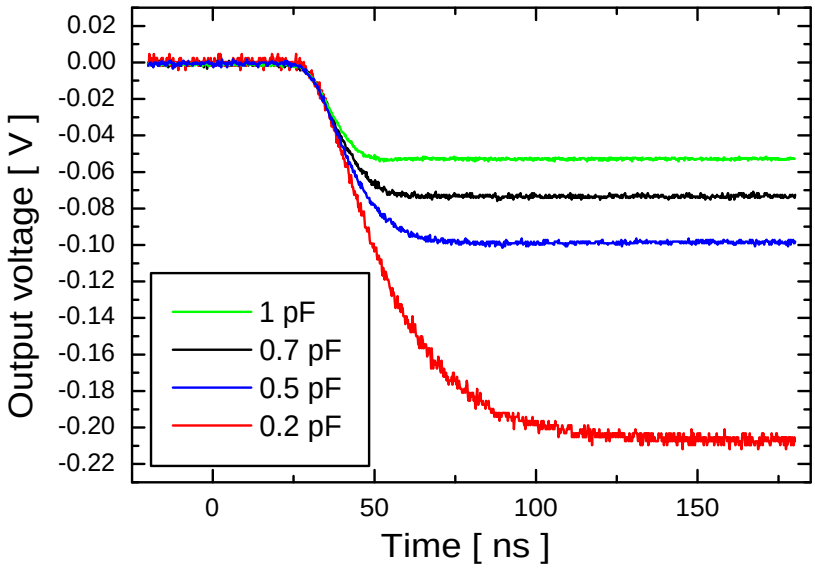

Figure 4.3: Output signals of different amplitudes. The pulser produced 50mV peak peak waveforms. The feedback capacitor of the CSP was digitally switched on four values: 0.2 pF, 0.5 pF, 0.7 pF and 1 pF. The Miller compensation capacitor was kept constant. The signal with bigger gain is slower because a smaller feedback capacitor means a lower loop gain and, in turn, a slower signal risetime.

digital slow-control. In figure 4.2 we can see the response of a front channel to an event of 1.57 MeV in silicon. The bandwidth was adjusted choosing different values of the Miller capacitor. The possibility to adjust the bandwidth to desire is an invaluable feature since, as can be seen in the aforementioned figure, we can maximize the speed of the preamplifier for different detector capacitances reducing ringing and avoiding instability on a case-by-case basis.

In figure 4.3 we can see the preamplifier response to a 2.63 MeV event (in silicon) selecting different feedback capacitances with the digital slow-control. Different experimental conditions can require higher or lower preaplifier gain. With a 1 pF feedback capacitor the amplitude of the CSP response function to a 1 MeV event is 0.038mV. We can boost the gain chosing a smaller feedback capacitance. For example, with 0.2 pF the CSP gain becomes 190mV / MeV. The value of the feedback capacitor not only determines the CSP gain but also the energy dynamic range. Being this component the crucial part of the CSP feedback network, it also determines the speed and bandwidth of the preamplifier. For all these reasons the possibility to adjust on-line the value of the feedback capacitor

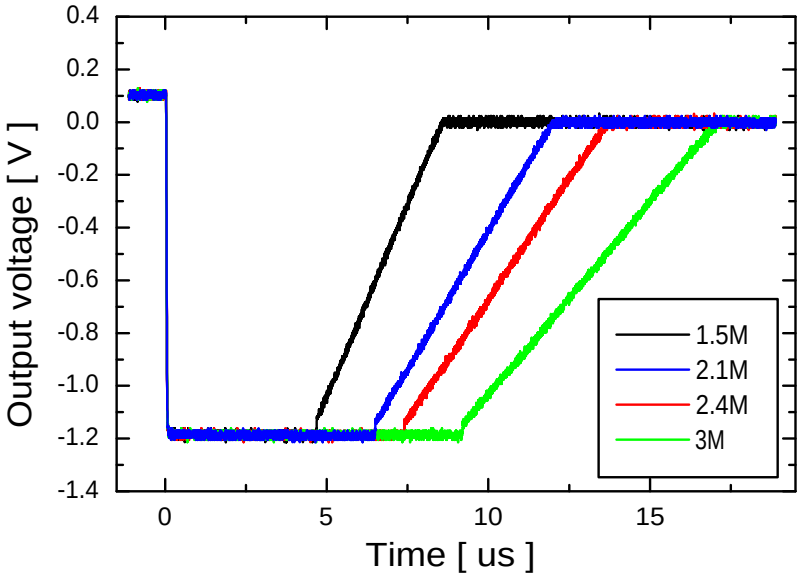

Figure 4.4: Output signals during the reset procedure. The pulser signal amplitude was kept constant and the reset current was set to four different values. The reset current is adjusted selecting different resistances connected to the current sink. The equivalent energy in germanium would be approximately 100 MeV while in silicon 142 MeV. The speed of the reset procedure is adjusted between 7.7 Mev/μs and 15 Mev/μs.

with a simple digital control is an invaluable feature in a lot of experimental situations. The speed of the reset procedure depends on the amplitude of the current generator of the "current sink" block. Higher reset currents lead to faster reset procedures, with a better minimization of the dead-time. If we are not interested only in dead-time reduction but we want also to perform high resolution spectroscopy with the Time-Over-Threshold (TOT) technique, smaller reset currents can induce smaller spectral broadening. We can adjust via digital slow-control the value of the resistance that generates the reset current. In this way the reset procedure can be optimized according to experimental needs. In figure 4.4 we can see the preamplifier output waveform produced by 142 MeV events in silicon. The speed of the reset procedure is adjusted between 7.7 Mev/μs and 15 Mev/μs.

4.2 Dynamic range and linearity

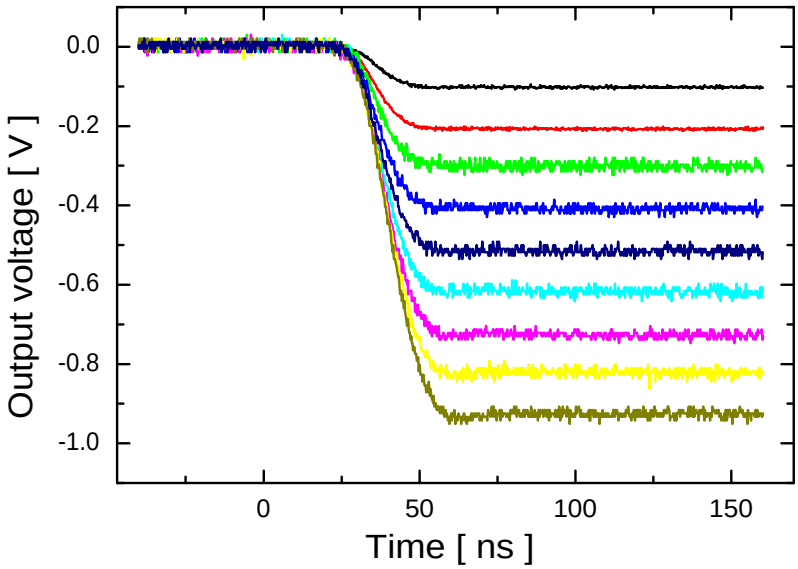

Figure 4.5: CSP output signals with different amplitude. The CSP was connected to a pulser through a test capacitor in order to evaluate the linearity of the response. The feedback capacitor chosen was 1 pF. The signals were generated simulating the detector with a pulser. The waveforms were recorded with a scope. The baseline was always kept to 0V.

The TRACE array is intended to detect and discriminate light charged particles in a wide energy range. A large output voltage swing is thus mandatory along with good linearity across the whole available dynamic range. In order to evaluate the circuit linearity and dynamic range we mounted the ASIC on the PCB described in the previous section. We simulated with a pulser a series of events with equally-spaced energies on a linear scale. We recorded the CSP output signals with a scope and measured the amplitudes of the response functions with a proper algorithm. The results in figures 4.5 and 4.6 show that the ASIC dynamic range extends up to 41 MeV in silicon. The linearity was evaluated by fitting the preamplifier output waveform amplitude vs the input test pulse amplitudes and fully meets the specifications.

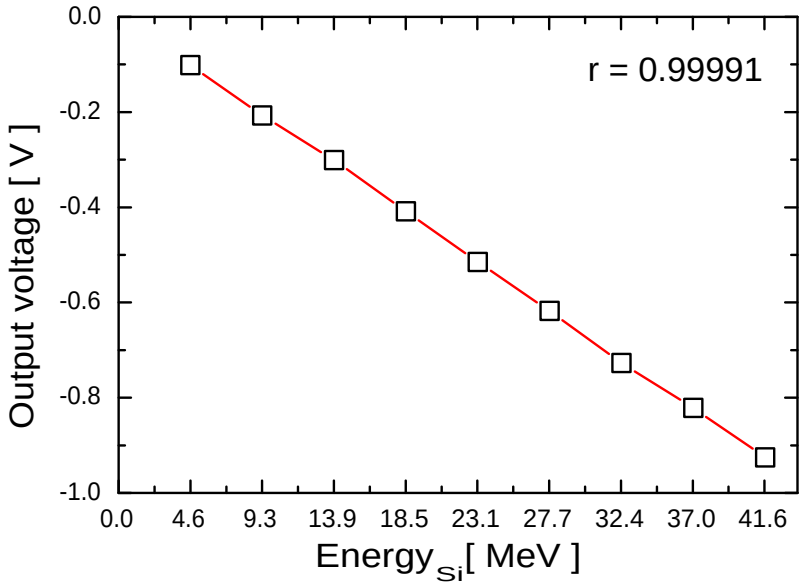

Figure 4.6: CSP signal amplitude versus event energy inside the detector. The feedback capacitor chosen was 1 pF. The signals were generated simulating the detector with a pulser. The waveforms were recorded with a scope.

4.3 Measurement of the equivalent noise charge at the input

The equivalent input noise was evaluated with the following setup. The pulser was connected to the preamplifier through a test capacitor. The output of the CSP was connected to a shaping amplifier with adjustable shaping time. The Gaussian signals thus obtained were recorded with a digital scope. The pulser was programmed to simulate 1 MeV events inside the detector. The pulse produced by the shaping amplifier was then normalized to a predefined amplitude. The pulser was then disconnected. The noise produced by the CSP and filtered by the shaping amplifier was recorded with the digital scope. The r.m.s. values of the random voltage fluctuations where then written in a table against the corresponding shaping time. This procedure was repeated for every channel of the preamplifier. The spectral content of the ENC was calculated with an algorithm that receives as input the ENC values against the shaping time. The results show a natural spread of the ENC values from channel to channel, but always in agreement both with simulations. The minimization of the equivalent input noise of the circuit is one of the aspects that deeply influenced the design of the ASIC. Particular care was taken in the reduction of the 1/f series noise contribute. The experimental results

reported in tables 4.1 and 4.2 are in agreement with the simulations and demonstrate that this ASIC fully meets the resolution requirements of the TRACE detector array.

Table 4.1: Equivalent noise charge at the input of the front channels, measured in electrons rms. The optimal shaping time is between 6 and 10 μs for every channel.

Shaping Time [μs]	ENC channel 1 [e^- rms]	ENC channel 2 [e^- rms]	ENC channel 3 [e^- rms]	ENC channel 4 [e^- rms]
0.5	265.7	242.1	258.4	246.1
1	214.6	193.8	207.9	198.3
2	175.3	155.6	170.2	160.1
3	161.8	143.8	157.9	145.5
6	150.6	131.5	147.2	128.1
10	151.7	130.9	146.6	132

Table 4.2: Equivalent noise charge at the input of the back channel, measured in electrons rms. The optimal shaping time is 10 μs.

Shaping Time [μs]	ENC back channel [e^- rms]
0.5	229.2
1	188.2
2	157.9
3	147.8
6	138.8
10	136.5

4.4 Acquisition of pulser-produced spectra

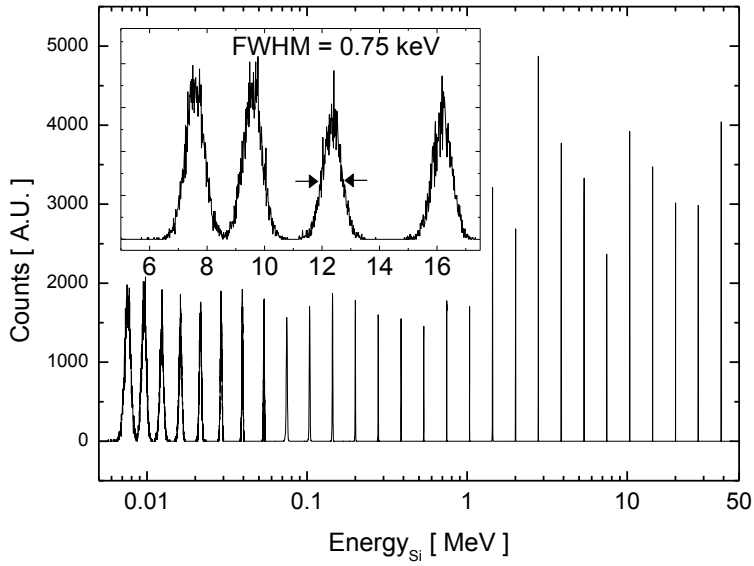

Figure 4.7: Energy spectrum obtained with a pulser connected to the fourth front channel of the ASIC preamplifier. Please note that the energy axis is in log scale. In the box in the upper-left corner the first four peaks are shown. The full width at half maximum of the peak at 12.5 keV is equal to 0.75 keV which is really good respect to the experimental requirements of the TRACE detector.

Beside analyzing the noise performances of the ASIC CSP with the aforementioned method, we wanted to evaluate the preamplifier performances with the acquisition of some spectra. The experimental setup was the following. We connected a pulser to the CSP input through a test capacitor of 1 pF. The pulser was programmed to simulate events in a detector equally spaced on an exponential scale between 7 keV and 700 MeV. In order to simulate low-energy events proper attenuators were connected between the pulser and the test capacitor. The CSP output signal was filtered with an ORTEC 572 shaping amplifier with 10us shaping time. The shaped pulses where then digitized with an Ortec MCB 926. The resulting spectrum was recorded on a PC with suitable software. This procedure was adopted for signals under the preamplifier saturation threshold.

For energies above the limit of 40 MeV and for the back channel only a time-over-threshold spectroscopic technique was used. The fast-reset device of the back channel produces a square pulse that lasts exactly the same time of the reset procedure. The length of the pulse is thus directly proportional to the charge removed from the input node. For

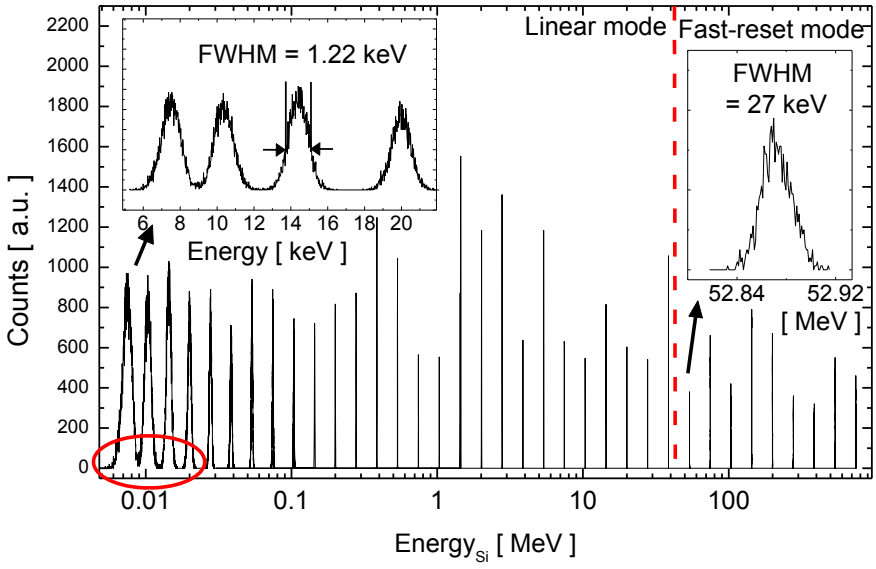

Figure 4.8: Energy spectrum obtained with a pulser connected to the back channel of the ASIC preamplifier. Please note that the energy axis is in log scale. In the box in the upper-left corner the first four peaks are shown. The full width at half maximum of the peak at 14.5 keV is equal to 1.22 keV which is acceptable for the experimental requirements of the TRACE detector.

over-threshold signals the usual analog output of the preamplifier was neglected. Only the auxiliary output of the fast-reset device was recorded using a digital oscilloscope. For every peak in figure 4.7 a thousand waveforms were recorded and inserted in a histogram according to the pulse duration. The histogram had 100 bins distributed around the peak mean value. The data collected with this new procedure were then calibrated and added to the low energy part of the spectrum to obtain the complete spectrum of figure 4.8. This experimental test not only demonstrated the good resolution capabilities of the preamplifier in the low-energy range but also confirmed the spectroscopic capabilities of the time-over-threshold method applied to the fast-reset signals. The Full-Width at Half-Maximum (FWHM) of the front channel, as can be seen in figure 4.7 is equal to 0.75 keV while the one of the back channel is 1.22 keV. These measures were obtained with a detector capacitance of 4 pF. The FWHM of the peaks produced by the Time-Over-Threshold method is equal to 27 keV. Considering that such technique is used only for energies above the limit of saturation (40 MeV with 1 pF of feedback capacitance) the relative broadeding is below 1‰ and thus is absolutely acceptable.

4.5 Experimental tests with a silicon pad detector and alpha source

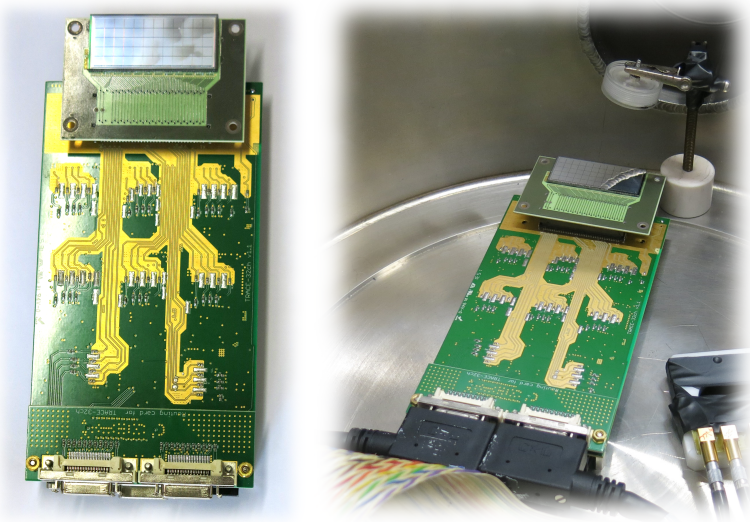

Figure 4.9: Left: photo of the TRACE-32ch v1.1 board connected to a TRACE silicon pad detector. Right: The preamplifier board inside the vacuum chamber with a ^{241}Am ^{244}Cm ^{239}Pu triple alpha source.

After having evaluated the ASIC functionality with the simple test PCB described in the previous sections we designed and realized a more complex preamplifier board: the TRACE-32ch v1.1. This is based on a 6-layer PCB made with a Rogers RO4003 hydrocarbon ceramic laminate. The total thikness is 1.6 mm. A poor-quality laminate can dramatically spoil the preamplifier performance. The choice of this material was due to its very good high-frequency performance and low dielectric loss. It is fully compatible with standard FR4 fabrication processes. This material, unlike PTFE ones, does not need special via preparation techniques like sodium etch. On the card there are six multichannel ASIC preamplifiers, for a total of 32 active front channels. Of the 8 back channels on the board only one was activated. The card is compatible with the standard connectors of the TRACE detector prototype PCBs. In figure 4.9 we can see the preamplifier board and a silicon pad detector inside a vacuum chamber with an alpha source. The detector front channels are biased by integrated punch-through resistors and AC coupled to the CSPs thanks to built-in decoupling capacitors realized on the detector surface. The back channel has no punch-through resistance or decoupling capacitor: these components must be added separately. We chose a high-voltage 2.2 nF decoupling capacitor and a 20 MΩ load resistance. The CSP output signals are routed to three

MDR-26 connectors while the digital slow-controls are routed to a HDMI connector. The board is made of a main card and a small additional routing card. This one extends the main card connectivity and is plugged on it by means of miniaturized low-profile connectors. The design of the PCB is mainly focused on the minimization of noise and undesired cross-talks between different channels. For this reason the power supply lines of each ASIC are individually filtered. Proper shields were placed between the output signals and the input nodes of the preamplifiers. Each output signal is shielded from the others by means of ground planes. During the design stage the solder mask was removed from the areas around the input node of the preamplifiers in order to avoid the noise induced by parasitic resistive paths. Particular care was taken designing the connections between the detector and the ASICs because the parasitic capacitance of the input node influences greately the noise performance of the preamplifier. On the board each ASIC has a different I^2C address so that they are independently programmable.

A 1 mm thick silicon pad detector was connected to the preamplifier card and put in a vacuum chamber with a non-encapsulated triple ^{241}Am ^{244}Cm ^{239}Pu alpha source. The output cone of the source was oriented towards the center of the detector in order to illuminate the pads that are processed by the 32 channels of the prototypical electronics. Due to the low sample activity the measurement took one whole night from 8PM to 9AM. The CSP output signals were terminated in a semi-differential configuration. The two wires of the differential line were connected through 50Ω resistances respectively to the CSP output and ground and acquired as a standard differential signal. Sixteen output signals were digitized with four N1728A CAEN modules. These are FPGA-powered 100 MHz 14-bit resolution digitizer cards with four differential inputs each. These modules record simultaneously the waveforms and the energies of the events calculated on-line with adjustable digital trapezoidal filters [20]. The 40 V detector bias was provided by a CAEN N1471 NIM power supply module. The trigger of the system was derived from the back signal of the detector by means of an ORTEC 855 shaping amplifier and an ORTEC 416A gate and delay generator. The spectra of the front and back channels were calibrated with the reference energies of the alpha source reported in table 4.3.

As we can see in figure 4.11 the spectrum acquired from the front pad chosen as reference has a resolution of ≈20 keV. In table 4.5 we can find the absolute and relative Full Width at Half Maximum (FWHM) of each peak. The wide broadening of the less-populated peaks (5143 keV and 5388 keV) should not be taken into account due to low

Table 4.3: Peak energies and relative amplitudes of the ^{241}Am ^{244}Cm ^{239}Pu alpha source used for the acquisition in the vacuum chamber. The energy correlation matrix obtained is visible in figure 4.14

Isotope	Peak Energy [MeV]	Relative peak intensity [%]
Pu-239	5.105	11.5
	5.143	15.1
	5.155	73.4
Am-241	5.388	1.4
	5.443	12.8
	5.486	85.2
Cm-244	5.763	23.3
	5.805	76.7

statistics. These results, reported in table 4.5, are not in agreement with the measurement of the resolution of the CSP we made on the test bench with the pulser. For this reason in table 4.6 we analysed all the possible causes of the spectral broadening: the noise coming from CSP, the thermal noise of load resistor R_{LOAD} of the pads and the back, the shot noise associated to the current that flows through the whole detector I_{DET} (10nA) or through each pad I_{PAD} and also the natural energy dispersion induced by the energy loss of the alpha particles during their travel across the 0.4 μm-thick aluminium metallization of the pads (alpha straggling). The last contribution is by far the most relevant one. This phenomenon has been already reported in literature [21].

The spectrum acquired from the back channel (figure 4.10) is characterised by lower resolution. It is difficult to evaluate the FWHM since the satellite peaks are completely indistinguishable from the main ones (5805 keV, 5486 keV, 5155 keV). The FWHM of the main peaks estimated with a multi-peak fit is ≈70 keV. The alpha straggling, as can be seen in tables 4.6 and 4.4 can justify the resolution of the front channel but not the peak broadening of the back channel. In this case the main cause of spectral broadening is the non-optimal experimental setup. The baseline of the back channel suffered from low-frequency voltage fluctuations in the order of 1V peak-to-peak caused by imperfect grounding and filtering of the detector power supply module. The back channel output signal was not directly connected to the digitizer cards but was split and connected to the trigger system. The splitting was operated by non-optimal conversion boxes which introduced additional noise. In future experiments an improvement in the back-end architecture is mandatory. The events were also plotted on a correlation matrix

(figure 4.14) with on the x-axis the energy of the back channel and on the y-axis the one of the front channel. In figure 4.12 and 4.13 we can see the output waveforms of both the back and a front channel. The results are encouraging and we foresee to use the TRACE32ch v1.1 board in an experimental context involving nuclear reactions with stable or radioactive beams.

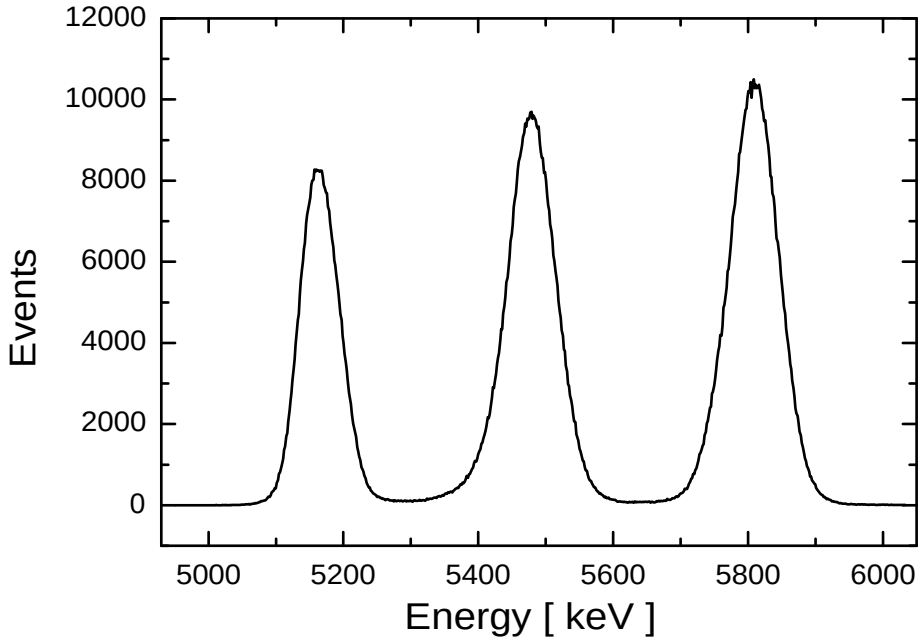

Figure 4.10: Spectrum of the ^{241}Am ^{244}Cm ^{239}Pu triple alpha source acquired on the back channel. The resolution is estimated to be ≈70 keV.

Table 4.4: Analysis of different contributions to the spectral broadening of the back channel.

Source	White component [A^2/Hz]	Corner frequency [Hz]	Corner time [s]	ENC^2 [C^2]	electrons rms [e^-]	sigma [keV]	FWHM [keV]
CSP noise (From simulation)	1.66E-29	5874	2.71E-05	1.22E-32	690.19	2.91	6.85
R_{LOAD}	5.52E-28	-	-	1.29E-33	224.02	0.94	2.22
I_{BACK}	2.24E-26	-	-	5.23E-32	1427.98	6.02	14.18
Alpha straggling (0.4 µm Al)	-	-	-	-	1427.97	6.02	14.18
Total					2145.87	9.05	**21.30**

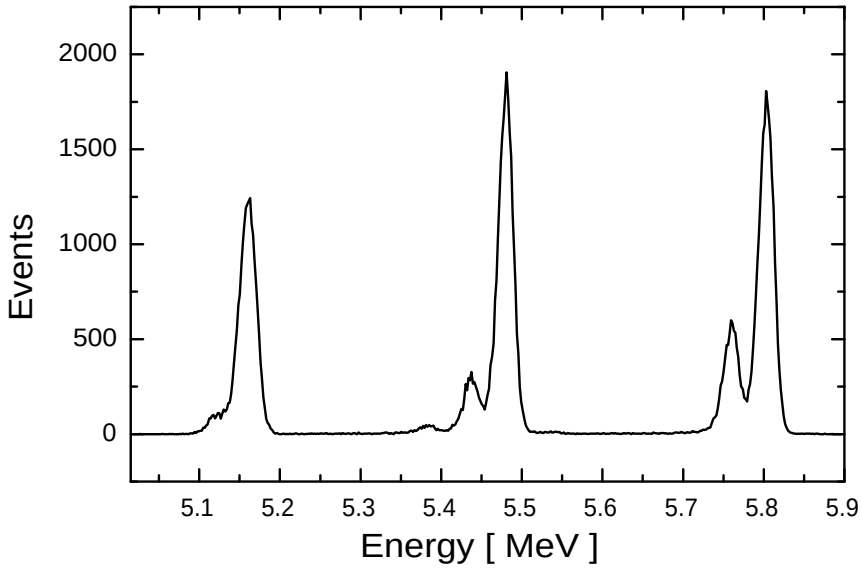

Figure 4.11: Spectrum of the ^{241}Am ^{244}Cm ^{239}Pu triple alpha source acquired on the front channel.

Table 4.5: Absolute and relative FWHM values for the seven peaks in the spectrum of figure 4.11

E [keV]	FWHM	FWHM %
5143	39.45	0.77
5155	23.81	0.46
5388	135.36	2.51
5443	26.28	0.48
5486	21.56	0.39
5763	24.80	0.43
5805	22.02	0.38

Table 4.6: Analysis of different contributions to the spectral broadening of the front channel.

Source	White component [A^2/Hz]	Corner frequency [Hz]	Corner time [s]	ENC^2 [C^2]	electrons rms [e^-]	sigma [keV]	FWHM [keV]
CSP noise (From simulation)	1.66E-29	39419	4.04E-06	3.09E-34	109.79	0.46	1.09
R_{LOAD}	5.52E-27	-	-	1.29E-32	708.43	2.99	7.03
I_{PAD}	3.74E-28	-	-	8.72E-34	184.35	0.78	1.83
Alpha straggling (0.4 μm Al)	-	-	-	-	1427.97	6.02	14.18
Total					1608.41	6.78	**15.97**

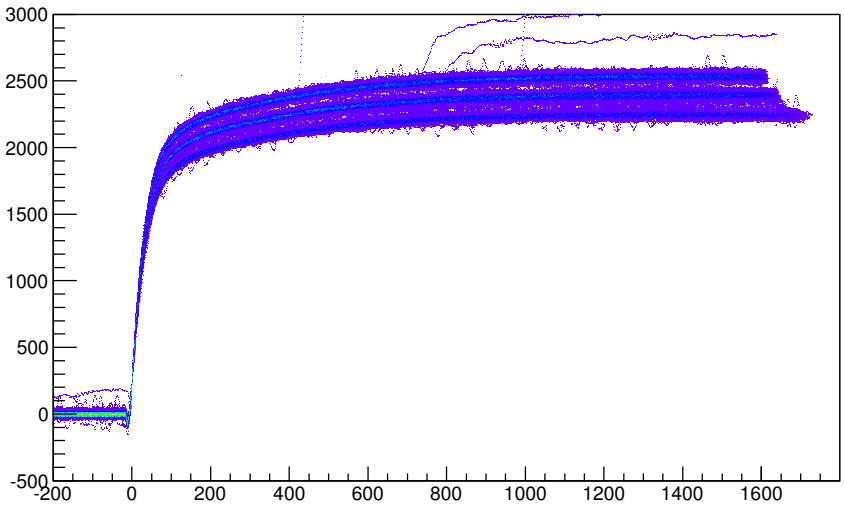

Figure 4.12: Signals acquired from the back channel. A ^{241}Am ^{244}Cm ^{239}Pu sample was used as alpha source. The lenght of the time window is 20 µs.

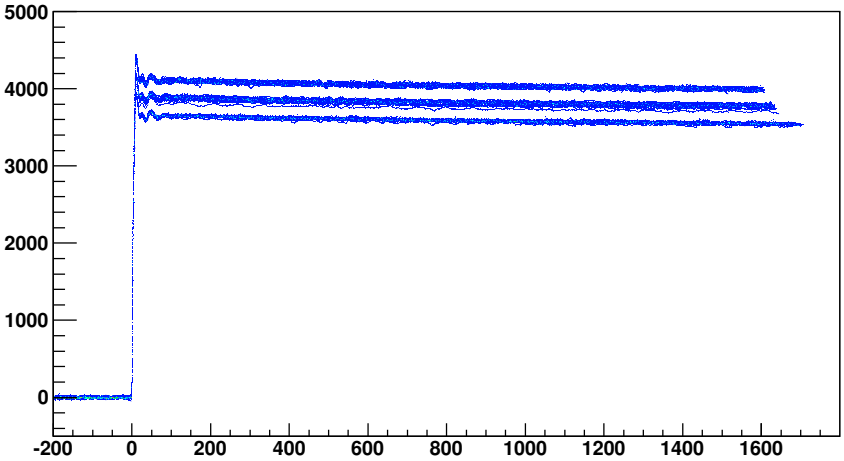

Figure 4.13: Signals acquired from a front channel. A ^{241}Am ^{244}Cm ^{239}Pu sample was used as alpha source. The three lines of the source are well separated and clearly distinguishable. The lenght of the time window is 20 µs.

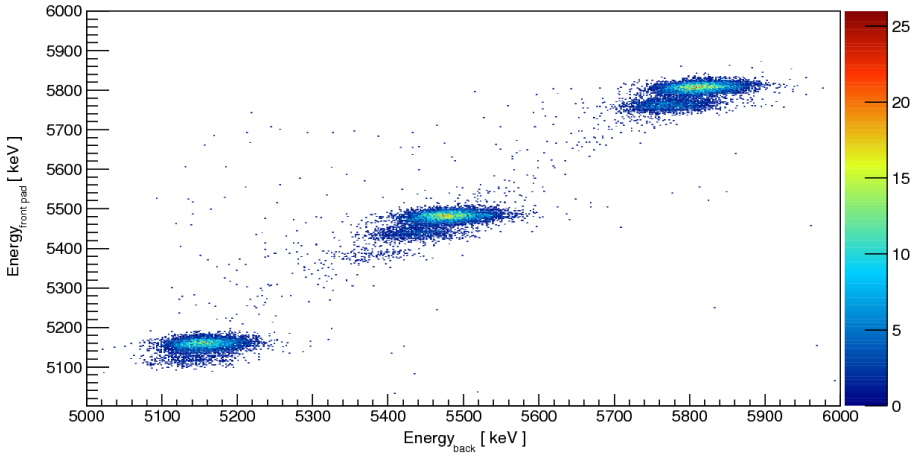

Figure 4.14: Correlation matrix of the energies on a front pad of the detector vs the energy measured on the back. For the measure a ^{241}Am ^{244}Cm ^{239}Pu alpha source was used. The energy FWHM of the front pad is equal to ≈3.5‰.

Conclusions

We designed, realized and tested a 5-channel integrated low-noise low-power charge-sensitive preamplifier specifically designed for the requirements of the TRACE detector array. The device was submitted to the foundry in the middle of 2014 and received at the end of the same year. The chip comprises four channels specifically designed for hole signals and one channel for electron signals. The power consumption is around 10 mW per channel as required by the specifications of TRACE. Experimental tests with the pulser demonstrated that the circuit resolution with a 4 pF detector capacitance is approximately 0.75 keV for the front channels and 1.22 keV for the back channel. The rise time of the signals is fast enough to perform pulse-shape analysis on the waveforms. With 4 pF detector capacitance, 1 pF feedback capacitance and proper bandwidth configuration the leading-edge risetime is in the order of 10 ns. This is an important aspect since one of the main goals of the TRACE detector array is the particle discrimination with PSA techniques. The slow-control engine is fully compliant with the I^2C standards and works as expected. The possibility to adjust a host of key parameters with a simple digital stream gives great flexibility to this ASIC. It can in fact be tuned to work properly with different kinds of solid-state detectors in a wide range of experimental situations. The bandwidth and sensitivity of the preamplifier can be optimized according to experimental needs on a case-by-case basis. The fast-reset technique boosts the dynamic range of the preamplifier by more than one order of magnitude. The spectra acquired with the time-over-threshold method are linear in an outstanding 800 MeV range. Even for the smallest signals that trigger the fast-reset technique the error associated to the TOT energy measurement is less than 1‰. We designed and realized a prototype preamplifier board with a total of

32 channels. We connected it to a 1 mm thick TRACE silicon pad detector and acquired the spectrum of a ^{241}Am ^{244}Cm ^{239}Pu triple alpha source. The resolution of the front channels is in the order of 3.5‰ of the total energy. Future perspectives include the realization of a new ASIC preamplifier with eight or ten channels and a new preamplifier board. This would be much more compact since, in search of the maximum integration possible, the new ASICs will be directly wire-bonded to the PCB.

Appendices

Appendix A

Integrated circuits suffer from the limited supply voltage they can tolerate without permanent damage. A reduced supply voltage yields a reduced output voltage swing. So, the overall dynamic range of integrated Charge Sensitive Preamplifiers (CSP) is typically remarkably smaller than that obtained with discrete component solutions. Losing the ability to measure the event energy is not the only problem associated with CSP saturation. Saturation translates into dead time, i.e. a certain window of time over which the preamplifier is not able to amplify/analyze the signals coming from the detector. We propose here an original circuit solution conceived to address these issues. Not only is the shown device able to reduce substantially the dead time. It even allows high resolution spectroscopy when the preamplifier is in deep saturation condition. For energies under the threshold of saturation the preamplifier works in a standard way, while for over threshold events an auxiliary signal is generated the amplitude of which is proportional to the energy released into the detector. It is based on the fast-reset device shown in this thesis work but includes also a time-to-amplitude converter able to correct the Time-Over-Threshold energy measurement from its baseline dependency.

A.1 Concept and functionality

The energy measurement of over-threshold signals is based on a "fast reset" circuitry. A comparator recognizes when the output voltage of the CSP reaches the saturation point. It triggers a switched current sink which starts draining the excess charge away from the input node of the preamplifier, i.e. the output node of the detector, until the preamplifier output voltage is brought back to the 0 V baseline level. In this way a substantial reduction of the dead time is obtained from some milliseconds to some microseconds typically, with

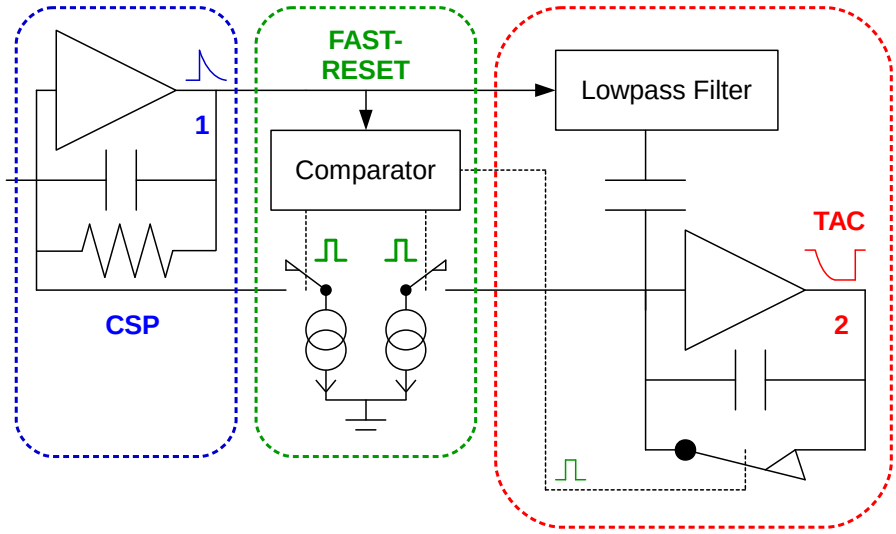

Figure A.1: Schematic diagram of the innovative TAC circuit with baseline rejection system. The signal marked with the number 1 is the standard output of the CSP. When the signals are under the threshold of saturation their amplitude is proportional to energy. The signal marked with number 2 is the auxiliary output from the TAC. When the CSP signals are saturated, TAC output signal are generated and their amplitude is proportional to energy.

a dramatic benefit for the experiments. When a large event saturates the CSP, the charge generated by the detector is not lost. It is conserved on the capacitance of the input node. We discharge the input node with a constant and controlled current sink. In this way we can deduce the amount of charge looking at the time taken for removing, at constant rate, the charge itself. A time over threshold analysis is then performed on the comparator signal, whose duration is proportional to the removed charge. The effectiveness of this method has been demonstrated in the previous chapters. However the method has a weak point. When performing a fast-reset cycle the residual charge of the tail of previous events is undistinguishable from the charge released by the detector in correspondence to the event we are measuring. The error due the presence of this stochastic charge could spoil the spectroscopic performances of the device, especially at high event rates. We hence designed a particular Time to Amplitude Converter (TAC) which not only converts the duration of the reset cycle into amplitude, but also corrects this one from the error induced by the tail observed at the beginning of the reset cycle. In this way the amplitude of the signals coming from the TAC is proportional to the energy of the last event only.

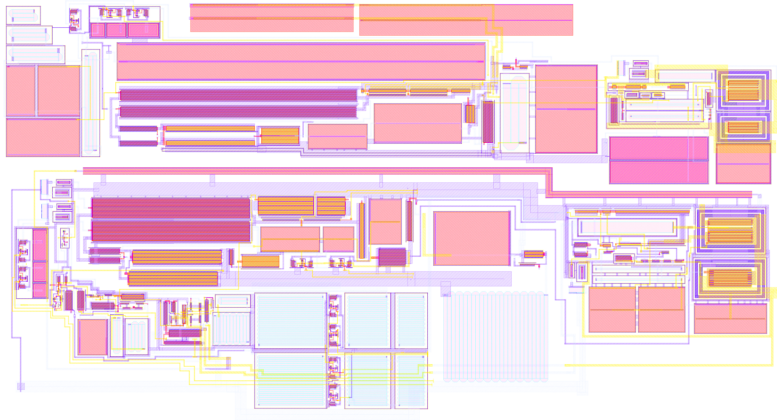

Figure A.2: Layout of the CSP with the TAC structure. The device is 570 μm x 1060 μm bonding pads excluded. It does not require any external component and both the CSP and the TAC are able to drive a 50 Ω coaxial cable.

The TAC signals can then be simply processed by a pulse-height analyzer. The TAC signals end with a nice flat-top which makes the sampling procedure easy. The height of these signals is proportional to the event energy up to 800 MeV. The original dynamic range of the preamplifier is thus extended by more than one order of magnitude.

A.2 Circuit structure

The circuit structure of the TAC, visible in figure A.1, is similar to that of a CAMEX filter. A multi stage low-pass filter is used in combination with controlled switches to perform an average of the baseline of the CSP before and after the reset cycle. These two values are subtracted one from the other and then used to correct the amplitude of the integrator voltage inside the TAC. For energies under the threshold of saturation the CSP works in a conventional way. When a high-energy event saturates the CSP the comparator triggers the fast-reset process. The TAC converts the duration of the comparator output signal into an analog voltage, rejecting the baseline thanks to the low-pass filter which acts as a delay line. In figure A.2 we can see the layout of the CSP with auxiliary TAC structure. Both the CSP and the TAC can drive a terminated 50 Ω coaxial cable.

A.3 Post-layout simulations

The graphs in figure A.3 and A.4 demonstrate the effectiveness of this approach. Figure A.5 shows that the residual fluctuation due to the tail is one order of magnitude smaller

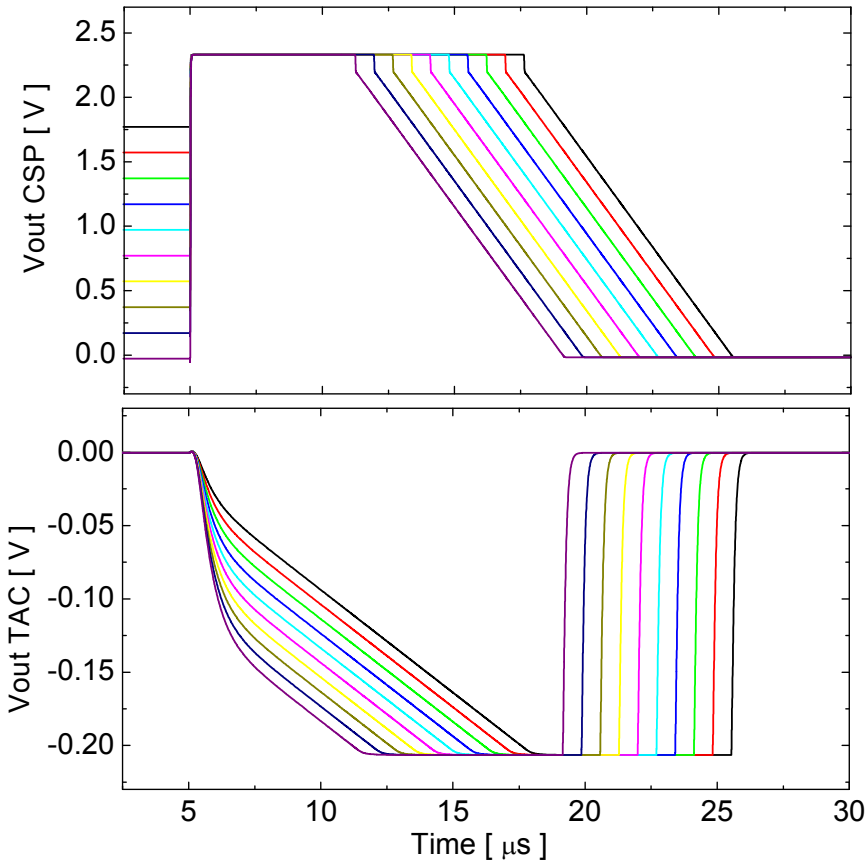

Figure A.3: Top: CSP output signals in correspondence to events of 74 MeV. The starting baseline is comprised between 0 V and 1.8 V. The saturation is recovered in some microseconds by the fast-reset device. The duration of the reset process is directly proportional to the energy of the event but is affected by the value of the baseline at the beginning of the reset process.
Bottom: TAC output signals. The TAC device receives as inputs both the comparator signal and the output of the preamplifier. The first one is used to determine the length of the reset process while the second one is used to correct the first one from the dependence on the baseline fluctuations. In this way the TAC produces analog signals with amplitudes directly proportional to the energy of the event that caused saturation and are unaffected by the baseline fluctuations. (Post-Layout Computer simulations)

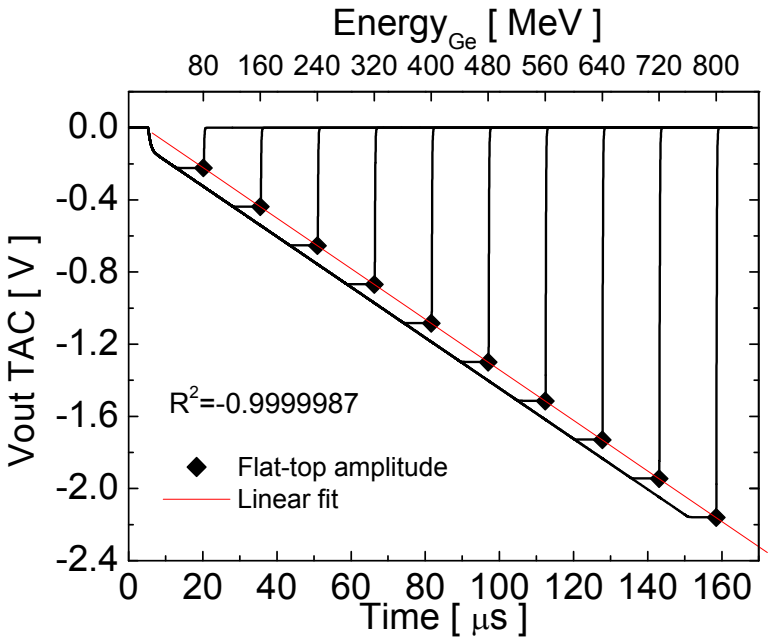

Figure A.4: TAC output signals during fast-reset events of different amplitudes. Even if the preamplifier signals are deeply saturated the voltage levels of the flat-tops are proportional to the energy of the event. Linearity is ensured up to 800 MeV in Ge. The TAC signals can thus be used to perform high-resolution spectroscopy at high energies. They do not need any kind of shaping and can be sent directly to a digitizer. (Post-Layout Computer simulations)

than the intrinsic noise of the circuit. Since these pulses do not require any kind of shaping, the r.m.s. fluctuation of the TAC output voltage is proportional to its equivalent input noise. As shown in figure A.5 this value is around 0.117 mV. Considering a CSP feedback capacitance of 1 pF and a TAC capacitance of 20 pF, this value corresponds to 102 keV FWHM. This procedure is triggered only for events with energy higher than 37 MeV. This means that the spectroscopic broadening introduced by noise is roughly 0.27% of the total energy. This is good enough not only for particle but also for gamma spectroscopy.

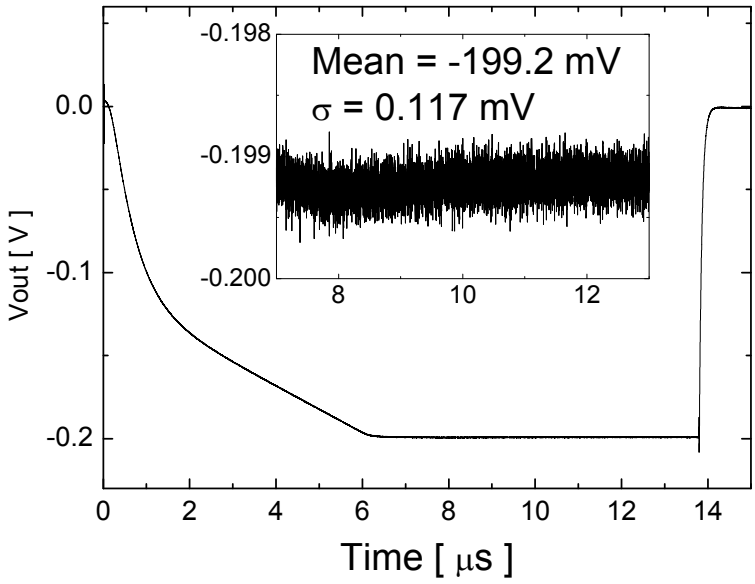

Figure A.5: Noisy waveform coming from the TAC circuit. The energy of the event is approximately 74 MeV. The detail shows the noise fluctuation of the flat-top. The standard deviation of the flat-top voltage level is in the order of 0.1% of its amplitude. This means that the combination of a fast-reset preamplifier and this particular kind of TAC device is able to produce energy spectra with resolution compatible with the requirements of gamma spectroscopy. (Post-Layout Computer simulation

Bibliography

[1] http://www.nndc.bnl.gov .

[2] http://pro.ganil spiral2.eu .

[3] http://www.orau.org/ria/pdf/ria-whitepaper 2000.pdf .

[4] Simpson, J. The euroball spectrometer. *Zeitschrift für Physik A Hadrons and Nuclei* **358**, 139–143 (2014).

[5] https://www.phy.anl.gov/gammasphere/ .

[6] Simpson, J. Gamma-ray spectroscopy of superdeformed states in the nucleus 152 dy. *Journal of Physics G: Nuclear and Particle Physics* **17**, 481 (1991).

[7] Kondev, F. G. e. a. *Phys. Lett B* (1998).

[8] Twin, P. J. *et al.* Observation of a discrete-line superdeformed band up to 60$\hbar$ in ^{152}Dy. *Phys. Rev. Lett.* **57**, 811–814 (1986).

[9] Byrski, T. *et al.* Observation of identical superdeformed bands in N =86 nuclei. *Phys. Rev. Lett.* **64**, 1650–1653 (1990).

[10] Akkoyun, S. *et al.* Agata—advanced gamma tracking array. *Nuclear Instruments and Methods in Physics Research Section A: Accelerators, Spectrometers, Detectors and Associated Equipment* **668**, 26 – 58 (2012).

[11] Uroić, M. *et al.* Improvements in data analysis obtained by large-area silicon ΔE - E detector telescopes. *Eur. Phys. J. A* **51**, 93 (2015).

[12] Mengoni, D. *et al.* Digital pulse-shape analysis with a trace early silicon prototype. *Nuclear Instruments and Methods in Physics Research Section A: Accelerators, Spectrometers, Detectors and Associated Equipment* **764**, 241 – 246 (2014).

[13] Pollacco, E. *et al.* Must2: A new generation array for direct reaction studies 287–288 (2005).

[14] Knoll, G. *Radiation Detection and Measurement, 3rd edition* (1999/2000).

[15] Balkanski, M. & Wallis, R. *Semiconductor Physics and Applications* (Oxford University Press, 2000).

[16] Watanabe, S. Multi-lorentzian model and 1/f noise spectra. *Journal of the Korean Physical Society* **46**, 646–650 (2005).

[17] Pascovici, G., Pullia, A., Zocca, F., Bruyneel, B. & Bazzacco, D. Low noise, dual gain preamplifier with built in spectroscopic pulser for highly segmented high-purity germanium detectors. *WSEAS Trans. Cir. and Sys.* **7**, 470–481 (2008).

[18] Pullia, A., Zocca, F., Pascovici, G. & Bazzacco, D. Extending the dynamic range of nuclear pulse spectrometers. *Review of Scientific Instruments* **79** (2008).

[19] Zocca, F., Pullia, A., Bazzacco, D. & Pascovici, G. A time-over-threshold technique for wide dynamic range gamma-ray spectroscopy with the agata detector. *Nuclear Science, IEEE Transactions on* **56**, 2384–2391 (2009).

[20] Radeka, V. Trapezoidal filtering of signals from large germanium detectors at high rates. *IEEE Transactions on Nuclear Science* **19**, 412–428 (1972).

[21] Pullia, A., Bertuccio, G., Maiocchi, D., Caccia, S. & Zocca, F. An SiC/GaN detector/front-end detection system for high-resolution alpha-particle spectroscopy. *IEEE Transactions on Nuclear Science* **55**, 3736–3740 (2008).